NTNU

Norwegian University of
Science and Technology

Qualitative and Quantitative Evaluation of Reservoir Quality Through Integrated Interpretation of CSEM, Seismic and Well Data

Pingvin Case Example

Victoria Flatås

Petroleum Geoscience and Engineering
Submission date: June 2017
Supervisor: Ståle Emil Johansen, IGP
Co-supervisor: Pål Gabrielsen, EMGS

Norwegian University of Science and Technology
Department of Geoscience and Petroleum

Abstract

In the last decades, the marine controlled source electromagnetic (CSEM) method has proven to be a useful tool for de-risking hydrocarbon prospects. Promising statistics and good data coverage in the Barents Sea have sparked the interest in using CSEM data for exploration purposes. The CSEM method has the advantage over conventional exploration techniques of being sensitive to hydrocarbon saturation *and* volume. The significance of integrating CSEM data with other geophysical data has been demonstrated in this thesis. Whether information in terms of reservoir quality can be obtained from CSEM data when incorporating seismic and petrophysical data, has been emphasized. Three-dimensional (3D) CSEM data together with two-dimensional (2D) seismic data and petrophysical data from exploration well 7319/12-1 have been used for qualitative and quantitative interpretation of the Pingvin gas discovery in the Bjørnøya Basin, Barents Sea. Quantitative interpretation entailed establishing relationships through petrophysical analysis between anomalous transverse resistance (ATR) and gross pay using models representing different reservoir qualities. These relationships have been combined with the ATR map created from constrained CSEM inversion results, to create gross pay maps from which reservoir quality has been interpreted.

The high-resistive CSEM anomaly obtained from constrained inversion corresponded with the seismic anomaly associated with the Pingvin discovery, both laterally and vertically. The resulting gross pay maps and the reservoir thickness interpreted from the seismic data have indicated improved reservoir quality towards the updip part of the seismic anomaly, relative to the part of the reservoir encountered by the well. Results have also shown that the gas saturation is likely to be higher in this same area compared to the saturation estimated from the well data. The results from this thesis highlight the importance of CSEM data for differentiating between brine and hydrocarbons as well as for qualitative and quantitative interpretation of reservoir quality.

Sammendrag

I løpet av de siste tiår har CSEM-metoden (aktiv kilde) vist seg å være et viktig verktøy for å redusere leterisikoen knyttet til offshore hydrokarbonprospekter. Lovende statistikker og god datadekning i Barentshavet har medført økt interesse for bruk av CSEM-data for leting etter olje og gass. Fordelen med denne metoden, sammenlignet med konvensjonelle letemetoder, er at den er sensitiv til både hydrokarbonmetning *og* -volum. Viktigheten av å integrere CSEM-data med andre geofysiske data er beskrevet i denne avhandlingen. Det er blitt vurdert i hvilken grad CSEM-data kan benyttes sammen med seismisk og petrofysisk data til å vurdere reservoarkvalitet. Tredimensjonal (3D) CSEM-data sammen med todimensjonal (2D) seismisk data og petrofysiske data fra letebrønn 7319/12-1 har blitt benyttet for kvalitativ og kvantitativ tolkning av Pingvin, et gassfunn i Bjørnøyabassenget i Barentshavet. Den kvantitative tolkningen innebar petrofysisk analyse for etablering av sammenhenger mellom *anomalous transverse resistance* (ATR) og *gross pay* fra modeller som representerte ulike reservoarkvaliteter. Disse sammenhengene ble kombinert med ATR-kart generert fra resultater fra tvungen CSEM-inversjon for å generere *gross pay*-kart som videre ble brukt til å tolke kvaliteten av det aktuelle reservoaret.

Den høyresistive CSEM-anomalien fremskaffet fra tvungen inversjon stemte godt overens med den seismiske anomalien forbundet med Pingvinfunnet, både lateralt og vertikalt. De resulterende *gross pay*-kartene og reservoartykkelsen fremskaffet fra seismikk indikerte en forbedring av reservoarkvalitet i retning av oppdippdelen av den seismiske anomalien, i forhold til reservoarkvaliteten i brønnområdet. Resultatene viste også at gassmetningen sannsynligvis er høyere i dette området sammenlignet med metningen estimert fra brønndata. Resultatene fra denne avhandlingen viser viktigheten av CSEM-data for å differensiere mellom vann- og hydrokarbonfylte reservoarer, samt for kvalitativ og kvantitativ tolkning av reservoarkvalitet.

Preface

This master's thesis is written at the Department of Geoscience and Petroleum at the Norwegian University of Science and Technology (NTNU) during the spring of 2017.

This thesis is the final result of a close cooperation with Electromagnetic Geoservices (EMGS). The work is performed by the author, with help from EMGS regarding the CSEM data. The method used for qualitative and quantitative interpretation of reservoir quality presented in this thesis is based on the work performed by Morten et al. (2017) and Granli et al. (2017).

The project involves interpretation of three different geophysical data sets; CSEM, seismic and petrophysical data. The reader is required to have basic knowledge on geology, petrophysical analysis and seismic interpretation.

This semester has been a great learning experience, from which I will benefit in my future career.

Victoria Flatås
Trondheim, Norway
June 2017

Acknowledgments

I would like to thank Electromagnetic Geoservices (EMGS) for giving me the opportunity to work with such an interesting and complex case and for allowing me access to software and office supplies. I am especially grateful to Pål T. Gabrielsen and Jan Petter Morten in EMGS for giving me strong academic support.

I would like to express my gratitude to my supervisor at the Norwegian University of Science and Technology (NTNU), Professor Ståle Emil Johansen, for providing valuable guidance and insightful comments. His reassuring words have been invaluable.

Erik Skogen and Sondre Fagerås deserve a thank you for assisting me with the petrophysical work. Dicky Harishidayat and Kamaldeen Olakunle Omosanya also deserve to be acknowledged for assisting me with the software Petrel and for helping me with the seismic depth conversion.

The NTNU-NPD-SCHLUMBERGER PETREL READY database and the NTNU-Multi Client Geophysical (MCG) are acknowledged for allowing me access to 2D seismic data from parts of the Southwestern Barents Sea. I would also like to acknowledge the NTNU-NPD DISKOS database for access to petrophysical data from exploration well 7319/12-1.

A special thank you to my mother and father for all the support throughout my years in Trondheim and for proofreading my thesis.

Last, but not least, I would like to thank my classmates for five memorable years at NTNU in Trondheim. I will miss the time we have spent together.

Contents

List of Figures

List of Tables

Chapter 1

Introduction

Electromagnetic sounding has proven to be useful in hydrocarbon exploration for identification of pore fluid composition (Johnstad et al., 2005; Johansen et al., 2008; Danielsen and Bekker, 2011; Gabrielsen et al., 2013; Vieugue, 2014). The controlled source electromagnetic (CSEM) method is ideal for detection of subsurface oil and gas accumulations because of the possibly large resistivity contrast between hydrocarbon-filled reservoir rocks (typically 20 - 1000 Ωm) and reservoirs filled with saline formation water (typically 0.5 - 2 Ωm) (Eidesmo et al., 2002a,b; Johansen et al., 2005). One great advantage with the method is that the electromagnetic energy is sensitive to net reservoir volume *and* hydrocarbon saturation, making it a suitable geophysical tool capable of reducing volumetric uncertainties (Baltar and Roth, 2013). This technique continues to gain acceptance in the oil industry because of the major potential for de-risking exploration. Promising statistics and good data coverage have increased the interest in utilizing CSEM data for exploration purposes, especially in the Barents Sea (Fanavoll et al., 2012).

The Barents Sea is experiencing increased interest in hydrocarbon exploration due to several recent discoveries like Skrugard, Wisting and Filicudi (Fanavoll et al., 2014a; Norwegian Petroleum Directorate, 2017). The importance of incorporating CSEM data when exploring for oil and gas in the Barents Sea is among others described by Fanavoll et al. (2014b). High-resistive anomalies at the Skrugard, Havis and Wisting discoveries indicate that the CSEM method can provide valuable geophysical information in these areas. Exploration in the Barents Sea is complicated by the complex geology, addressing the need for new methods useful for hydrocarbon volume estimation and reservoir characterization.

Studies addressing quantitative reservoir characterization from integrated interpretation with CSEM data have been published the last years (e.g. Harris et al. 2009; Morten et al. 2011, 2012; Alvarez et al. 2017). These studies demonstrate that 3D CSEM data can be useful not only to differentiate qualitatively between brine and hydrocarbons, but also, in combination with seismic and petrophysical data, to quantitatively estimate fluid distribution. Significant ambiguities are associated with quantitative interpretation of reservoir properties from seismic data only (Eidesmo et al., 2002a; Morten et al., 2012). CSEM data, petrophysical data and seismic data are obvious complementary geophysical methods as they provide different sensitivity characteristics. Structural information is provided by the seismic data, reservoir rock properties like porosity and water saturation at the well position are provided by the petrophysical data and information on formation pore fluid is provided by the CSEM data. There is no method for quantitatively characterize hydrocarbon reservoirs from CSEM, seismic and petrophysical data that is extensively used by oil companies today.

For this master's thesis, the Pingvin gas discovery in the Bjørnøya Basin in the Barents Sea is studied for evaluation of reservoir quality. This is done through a qualitative and quantitative, joint interpretation of three-dimensional (3D) CSEM data, two-dimensional (2D) seismic data and petrophysical data from exploration well 7319/12-1. The location of the Pingvin discovery is illustrated in Figure 1.1. The Bjørnøya Basin is relatively unexplored and this thesis provides additional knowledge for future hydrocarbon exploration in the area. The 3D CSEM data was acquired prior to the drilling of the well, from which a high-resistive anomaly was obtained at the location of the seismic anomaly associated with the Pingvin discovery (Fanavoll et al., 2014a). The primary objective for writing this thesis is to investigate whether additional information in terms of reservoir quality can be obtained from the CSEM data when incorporating seismic and petrophysical data. Interpretation of gas saturation within the reservoir is also in focus. The importance of incorporating all available information when working with hydrocarbon exploration is emphasized.

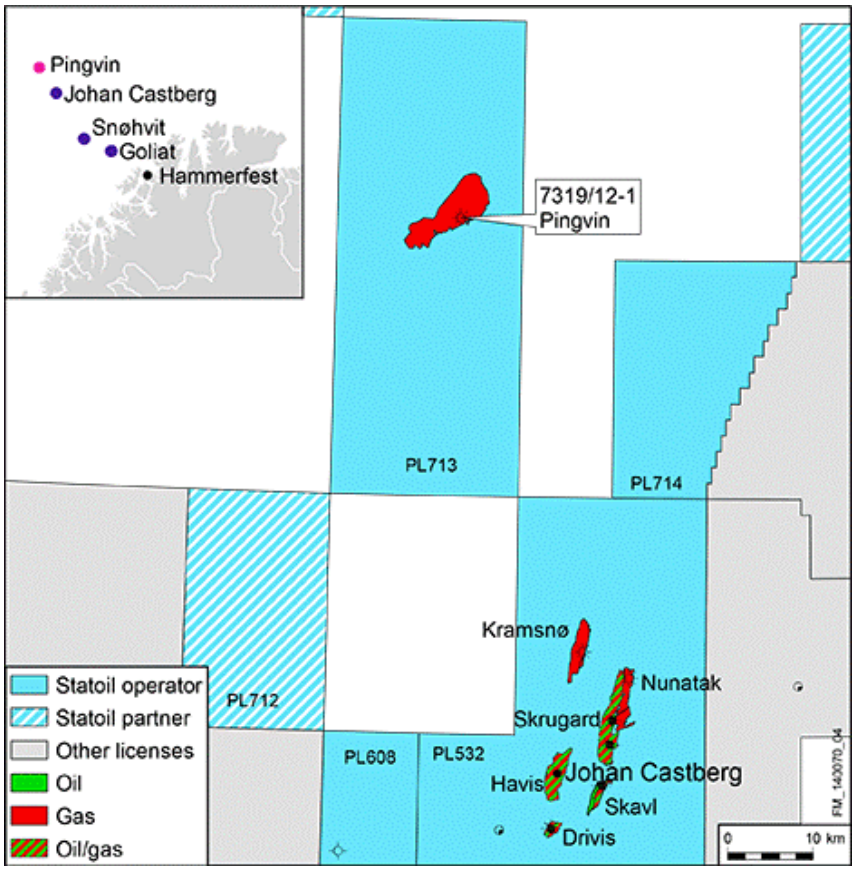

Figure 1.1: *Location of the Pingvin gas discovery within the Statoil-operated licence PL713 in the Bjørnøya Basin in the Barents Sea. The oil and gas field Johan Castberg is located about 60 kilometers Southeast of Pingvin. Figure from (Statoil, 2014).*

Chapter 2

Geological Setting

2.1 Tectonic Evolution of the Southwestern Barents Sea

As summarized in Johansen et al. (1993), Doré (1993) and Gudlaugsson et al. (1998), the Southwestern Barents Sea is recognized by its many platforms, rift basins and NE-SW to N-S trending fault complexes. Since the culmination of the Caledonian orogeny about 400 million years ago, several phases of tectonism have affected the geology in the area. In contrast to the Southwestern Barents Sea, the Eastern and Northeastern parts have since Late Carboniferous been dominated by less tectonic activity and are recognized by relatively stable platforms (Gabrielsen et al., 1990; Breivik et al., 2005). Episodes of extensional tectonic movements have been recorded in the late Paleozoic and Mesozoic in the Southwestern Barents Sea, marking the end of the Pangaea supercontinent. The rifting was mainly caused by the collapse of the Caledonian and Ural mountains and later periods of break-up of Pangaea. The result was sea floor spreading, with the resulting intervening series of platforms, structural highs and rift basins. Marine sediments are the dominant filling of these rift structures. In late Paleozoic and early Mesozoic, the marine depositional environment was not only influenced by tectonics, but also by climate changes. The Barents Sea experienced lower temperatures as the area drifted from a paleolatitude of 20°N in the Carboniferous to 55°N in the Triassic and ending at its present position of about 75°N. Clastic sedimentation has dominated the deposition from

the Triassic era, whereas carbonates and occasional evaporite intervals were preserved over large areas in the Paleozoic (Worsley, 1986).

The Northeast-oriented North Atlantic rift system caused by the break-up of Pangaea was in late Cretaceous and Paleocene accompanied by a North-South oriented zone with faults on both sides of the margins. This zone has been given different names by different authors, but the name De Geer Zone is recognized by many earth scientists (Doré, 1991; Breivik et al., 1998; Faleide et al., 2008, 1993). The De Geer Zone in the Barents Sea links the Atlantic and Arctic regions. The Cretaceous sediments have been subject to several periods of erosion, limiting our knowledge about the depositional environment. It has however been proven that shale and claystone interbedded with thin beds of silt, limestone and dolomite were deposited during the early Cretaceous. These sediments are the main filling of the deep basins in the Barents Sea. (Johansen et al., 1993; Faleide et al., 2015; Ramberg et al., 2007)

As with the Cretaceous, the Cenozoic era is characterized by marine deposition and episodes of erosion (Doré, 1993). Baig et al. (2016) has by studying shale compaction and maturity techniques, estimated the average Cenozoic exhumation for specific areas in the Barents Sea. The estimated exhumation ranges from 800 to 1400 meters in the Hammerfest Basin and from 1150 to 1950 meters on the Loppa High. Johansen (2016) has estimated the average net erosion from shale velocity and sandstone diagenesis to range from 800 to 1500 meters in the Bjørnøya Basin.

Neogene and Quaternary ice age periods have greatly influenced the petroleum systems in the Barents Sea. The glaciers have eroded the Norwegian mainland as well as the continental shelf and Svalbard. Rivers and glacial streams have in earlier times been the dominating erosional mechanisms. The consequences of melting glaciers have been the rise of the Norwegian mainland and the inner continental shelf and simultaneous subsidence of the outer continental shelf. Previously deeply buried sediments have experienced (and still experiences) pressure release as a result of uplift, causing re-migration of oil and gas. Multiple wildcat wells in the Barents Sea have detected oil shows, but only a few of which have encountered large volumes of oil or gas. It is likely that gas has gone out of solution due to decreased formation pressure, displacing the original oil in place. From seismic data, gas leakage has been detected in many areas in the Southwestern Barents Sea. The leakage is closely linked to the erosion and uplift in the Cenozoic. (Ramberg et al., 2007)

Figure 2.1 illustrates the different geological provinces in the Southwestern part of the Barents Sea. The lithostratigraphy and chronostratigraphy of the Southwestern Barents Sea are presented in Figure 2.2. The transect crosses the Sørvestsnaget and Tromsø Basins, Ringvassøy-Loppa Fault Complex, the Hammerfest Basin and the Bjarmeland Platform.

2.2 The Bjørnøya Basin

The Bjørnøya Basin is surrounded by Stappen High in the North, Veslemøy High in the South and Loppa High in the Southeast (see Figure 2.1). The basin is bounded by the Bjørnøya Fault Complex to the Southeast and the Northwestern boundary is also influence by faulting. The Bjørnøya Basin has experienced faulting and has thus some characteristics of a large-scale half-graben (Gabrielsen et al., 1984). The basin developed as a result of the opening of the North Atlantic Ocean and the De Geer Zone in the Cretaceous and early Cenozoic. Because of Cretaceous subsidence, the basin is mainly filled by Cretaceous sediments (Breivik et al., 1998; Ryseth et al., 2003). Despite Cenozoic erosion and limited sediment supply in the Paleogene and Neogene, Cenozoic deposits are present in the Bjørnøya Basin (Ramberg et al., 2007). Due to heavy uplift and erosion in the area, the upper part of the basin-fill sequence does not exist today. (Gabrielsen et al., 1990)

Figure 2.3 shows regional profiles crossing the Bjørnøya Basin in W-E and SW-NE directions. Thick Cretaceous sediments have been deposited and preserved. The Knurr Formation was deposited as calcareous marine mud. The younger Kolje Formation and Kolmule Formation are muddy deposits characterized by less interbedded calcareous beds.

2.3 The Pingvin Gas Discovery

The Pingvin gas discovery is located in the Bjørnøya Basin, about 60 kilometers Northwest of the oil and gas field Johan Castberg (see Figure 1.1). 3D seismic data has proven the presence of a flat-spot and acquired CSEM data has indicated a strong CSEM anomaly only in the upper part of the seismic anomaly. Wildcat well 7319/12-1, drilled by Statoil in 2014, encountered a 15-meters gas column in the Torsk Formation at 953 meters MD.

The late Paleocene to Oligocene Torsk Formation has in the Barents Sea been deposited as shallow marine mud with interbedded sand bodies and limestone/siltstone stringers (Ramberg et al., 2007; Norwegian Petroleum Directorate, ndf). The reservoir has been identified as a Paleocene sandstone reservoir with good porosity, but with poor permeability (Løseth et al., 2015).

Preliminary resource assessments have estimated an accumulation of recoverable gas ranging from 30 to 120 million barrels of recoverable oil equivalents. Due to the limited gas volumes and lack of infrastructure in the Bjørnøya Basin, the discovery is considered of having no commercial value. It is however promising that a reservoir and a functioning hydrocarbon system has been discovered in this relatively unexplored area. (Løseth et al., 2015)

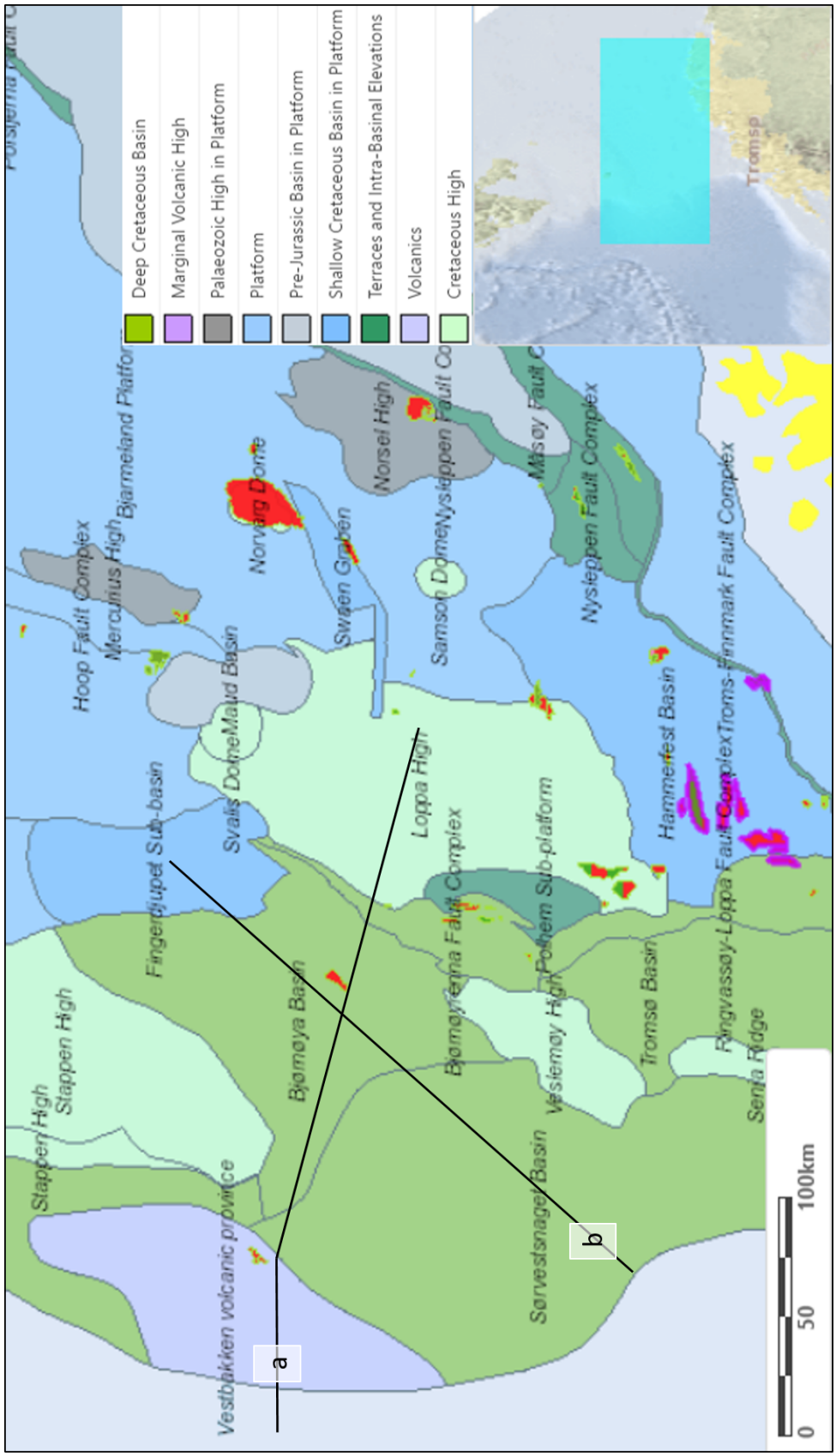

Figure 2.1: *Regional structural map from the Southwestern Barents Sea. The red areas represent detected gas-filled reservoirs, green is detected volumes of oil and pink represents condensate. Lines a and b represent locations of regional geological profiles. Figure modified from (Norwegian Petroleum Directorate, nda).*

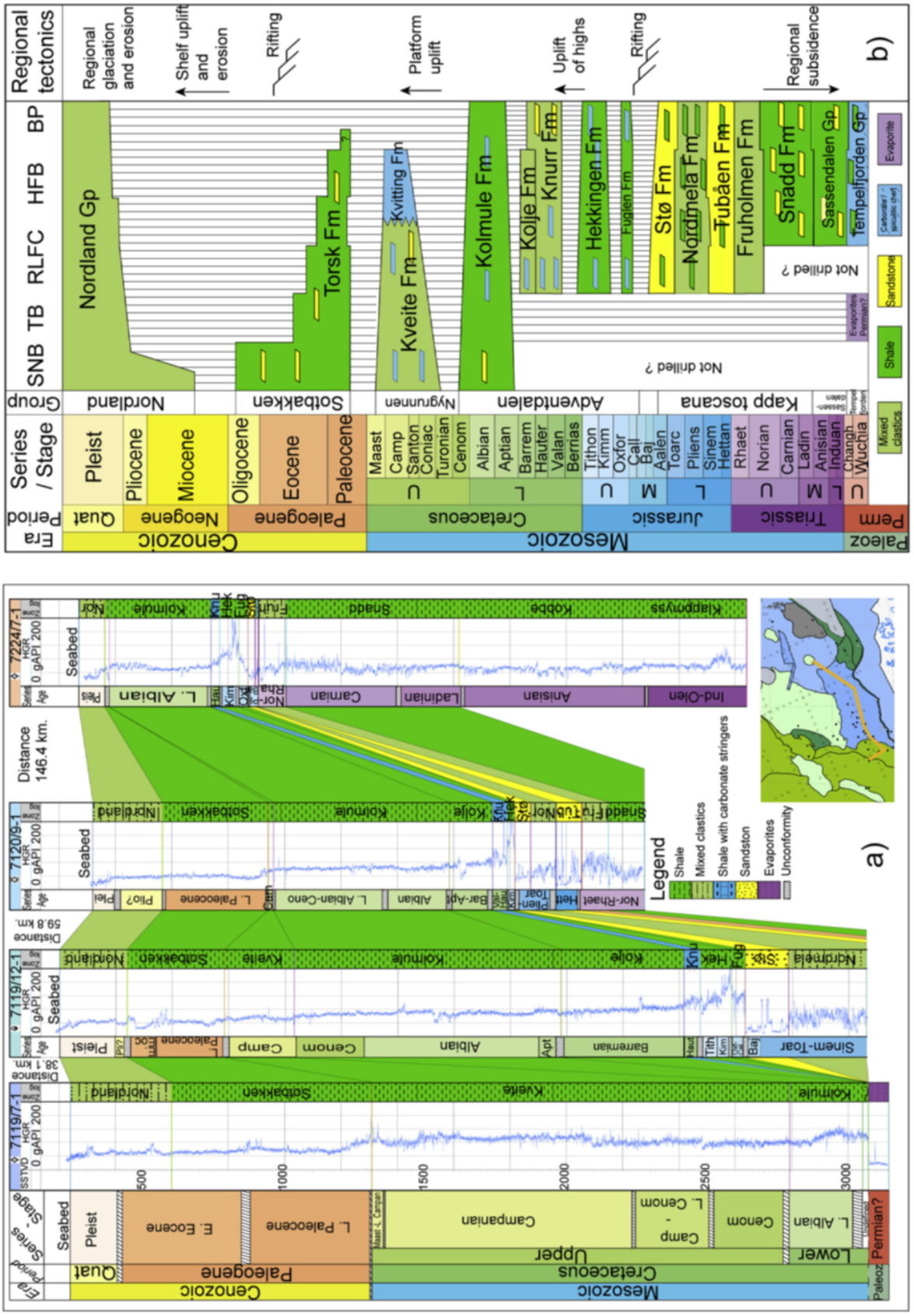

Figure 2.2: *Stratigraphical nomenclature of the Southwestern Barents Sea: (a) Lithostratigraphic correlation from well logs and (b) chronostratigraphic correlation. The sections cross the Sørvestsnaget Basin (SNB), Tromsø Basin (TB), Ringvassøy-Loppa Fault Complex (RLFC), Hammerfest Basin (HFB) and Bjarmeland Platform (BP). Figure from (Baig et al., 2016) which has been modified from (Dalland et al., 1988; Ryseth et al., 2003; Worsley, 2008).*

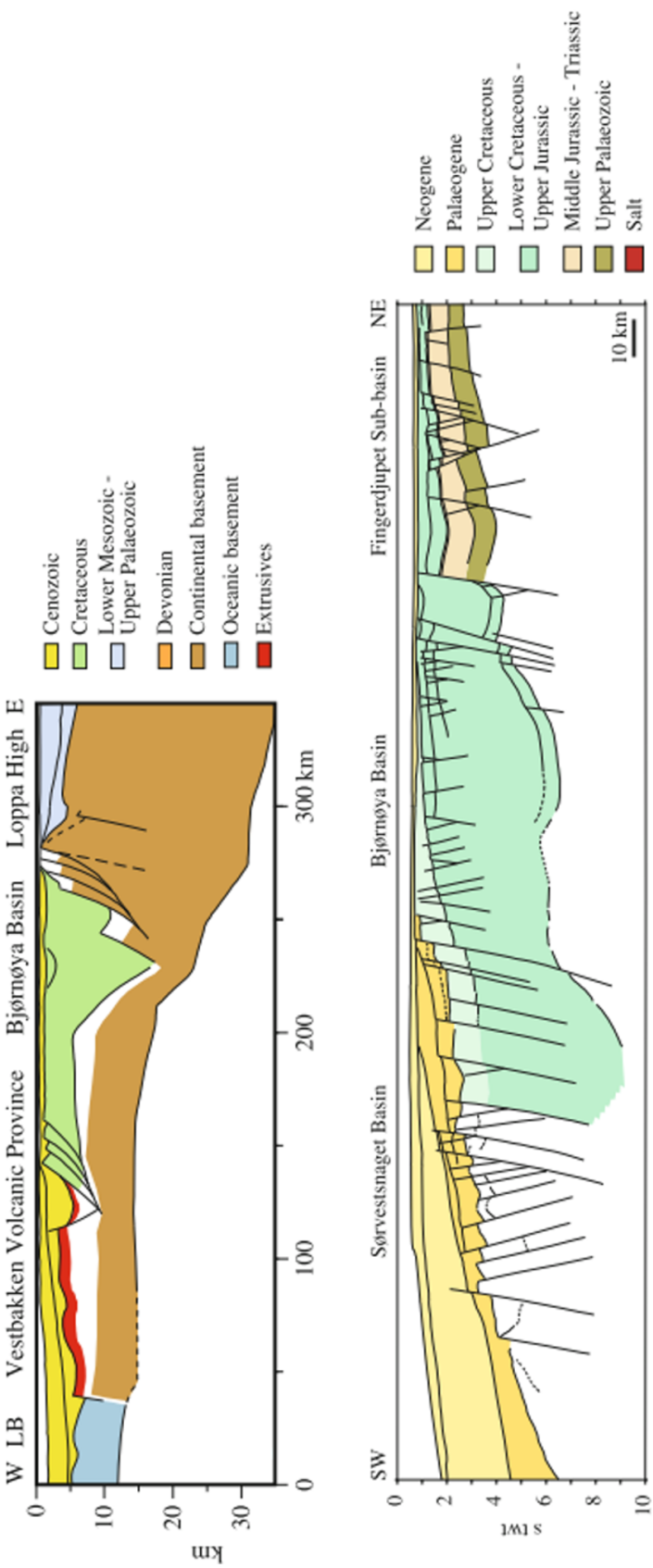

Figure 2.3: *Regional profiles crossing the Bjørnøya Basin (a) in the W-E and (b) in the SW-NE directions. The Bjørnøya Basin is mainly filled by Cretaceous and Cenozoic sediments. See Figure 2.1 for location of the profiles. Figure (a) modified from Faleide et al. (2008) and figure (b) modified from Faleide et al. (1993); Breivik et al. (1995).*

Chapter 3

Relevant Background Theory

3.1 Marine 3D CSEM for Hydrocarbon Prospecting

An introduction to the controlled source electromagnetic (CSEM) method; background theory, workflow and application, is given in this section. The method presented was developed by Statoil (Eidesmo et al. (2002a)), from which Electromagnetic Geoservices (EMGS) was established in 2002.

3.1.1 Basic CSEM Concepts

Controlled source electromagnetic (CSEM) data has the advantage of being sensitive to resistivity contrasts in the subsurface. The CSEM technology utilizes that the resistivity readings when running electric currents through a hydrocarbon-saturated sedimentary rock are significantly different from the resistivity readings from the same rock saturated with saline water. Typical values are 20 - 1000 Ωm for sedimentary rocks with high saturations of hydrocarbons and 0.5 - 2 Ωm for sedimentary rocks filled with saline water (Johansen et al., 2005; Johansen and Gabrielsen, 2015). The bulk resistivity is largely determined by the pore fluid resistivity. Hence, resistivity is an important rock property for discovering and localizing hydrocarbon accumulations. (Eidesmo et al., 2002b,c)

Figure 3.1 illustrates resistivity ranges for different earth materials. Interpretation of resistivity models obtained from CSEM data is complicated by the fact that there are

several geological features that exhibit high resistivities. Examples are carbonates, salt, igneous rocks, low-porosity rocks, organic-rich rocks and some minerals (Hesthammer and Boulaenko, 2005; MacGregor and Tomlinson, 2014).

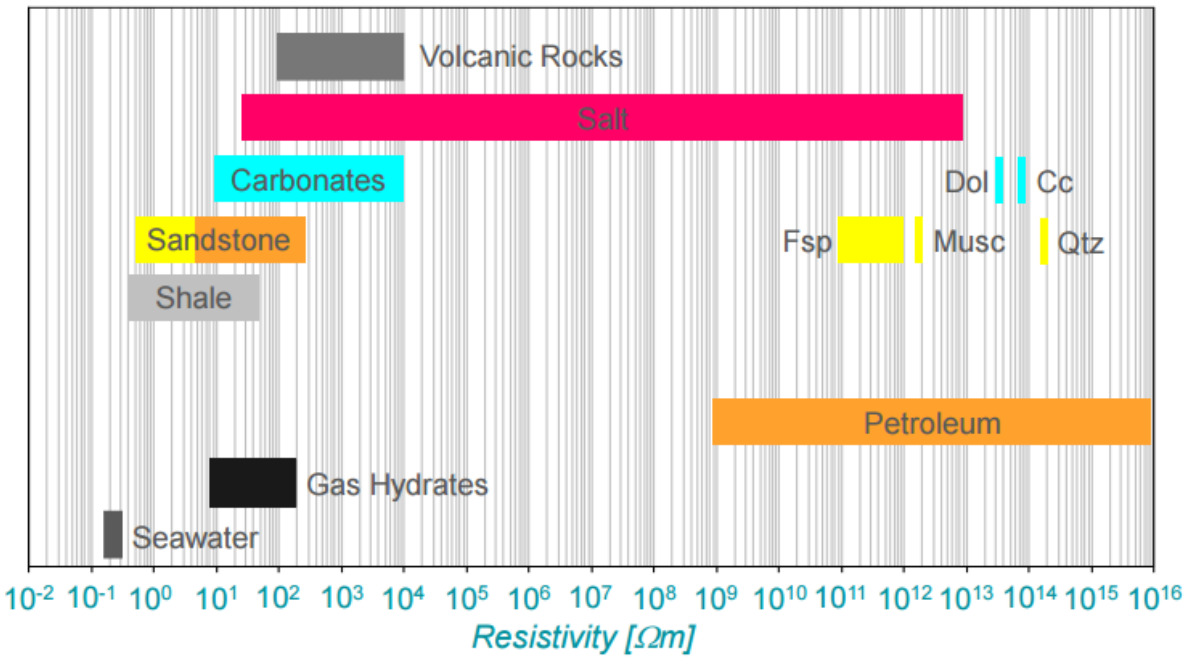

Figure 3.1: *Resistivity ranges for different earth materials. Oil and gas exhibit much higher resistivities compared with seawater, but there are also other geological features exhibiting high resistivities. Notice that the resistivities are for pure substances. The resistivity is in logarithmic scale. Figure modified from (Palacky, 1987; Eidesmo et al., 2002a)*

The formation resistivity is largely dictated by the interplay between the porosity, water saturation, salinity of the formation water and the temperature (Schlumberger, 1987; Rider, 1996). For a clean reservoir sandstone, the formation resistivity can be determined by the use of the Archie equation

$$R_t = \frac{a * R_w}{\phi_t^m * S_{w,t}^n} \tag{3.1}$$

where a, m and n are rock property coefficients, R_w is the water resistivity, ϕ_t is the total porosity and $S_{w,t}$ represents the water saturation in the total pore space (Archie, 1942). More complicated models are required in order to account for the volume and the distribution of clay.

Knowledge on how resistivity is dependent on rock properties is essential for interpretation of CSEM data. Figure 3.2 illustrates how resistivity changes with porosity, hydrocarbon saturation, water salinity and temperature. Keep in mind that the creation of the curves is based on the Archie equation, i.e. assuming a clean sandstone formation.

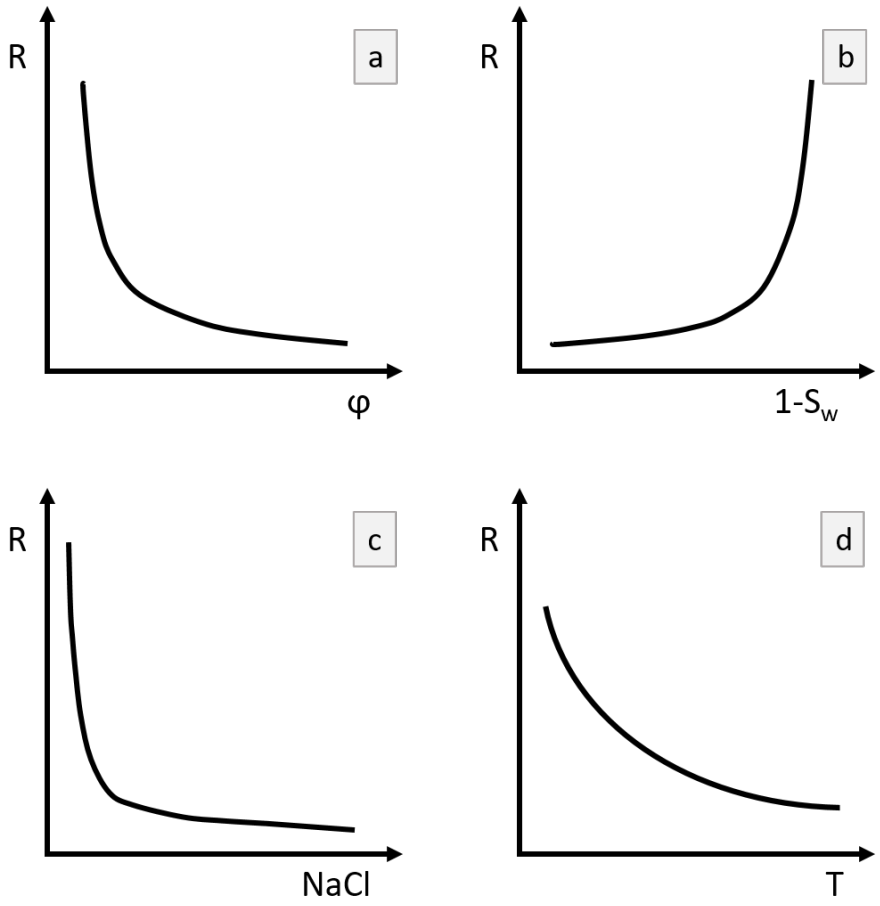

Figure 3.2: *Resistivity as a function of (a) porosity ϕ, (b) hydrocarbon saturation 1-S_w, (c) water salinity NaCl and (d) temperature T. The resistivity trends are estimated from the Archie equation (Equation 3.1), assuming a clean sandstone formation. One variable is changed while keeping the others constant. The relationship between temperature, salinity and water resistivity is found from the Schlumberger chart GEN-6 (see Figure A.4) (Schlumberger, 2009).*

Figure 3.2b shows that the resistivity changes drastically for high hydrocarbon saturations. This relation is utilized in the CSEM method for detection of commercial-scale hydrocarbon-filled reservoirs (see Figure 3.9).

3.1.2 CSEM Data Acquisition

CSEM data is acquired by emitting a carefully designed, continuous electromagnetic signal through the seawater and the bedrock. These signals are recorded by stationary receivers placed at the seabed. The active source, a powerful horizontal electric dipole source, is towed behind a data acquisition vessel in a predetermined pattern (see Figure 3.3). The signal is low-frequent (0.1 - 30 Hz), with the main energy output at the lower part of the frequency spectrum. The receivers are recording while the source is towed above the receiver grid along so-called towlines. For 2D data acquisition, receivers are placed along one receiver line with the vessel towing the source along the same line. The resolution of the data decreases with increasing receiver spacing (Bhuiyan et al., 2010). The receivers sink freely down to the seabed and are detached from their anchor when the survey is finished. (Eidesmo et al., 2002b,c; Ellingsrud et al., 2002)

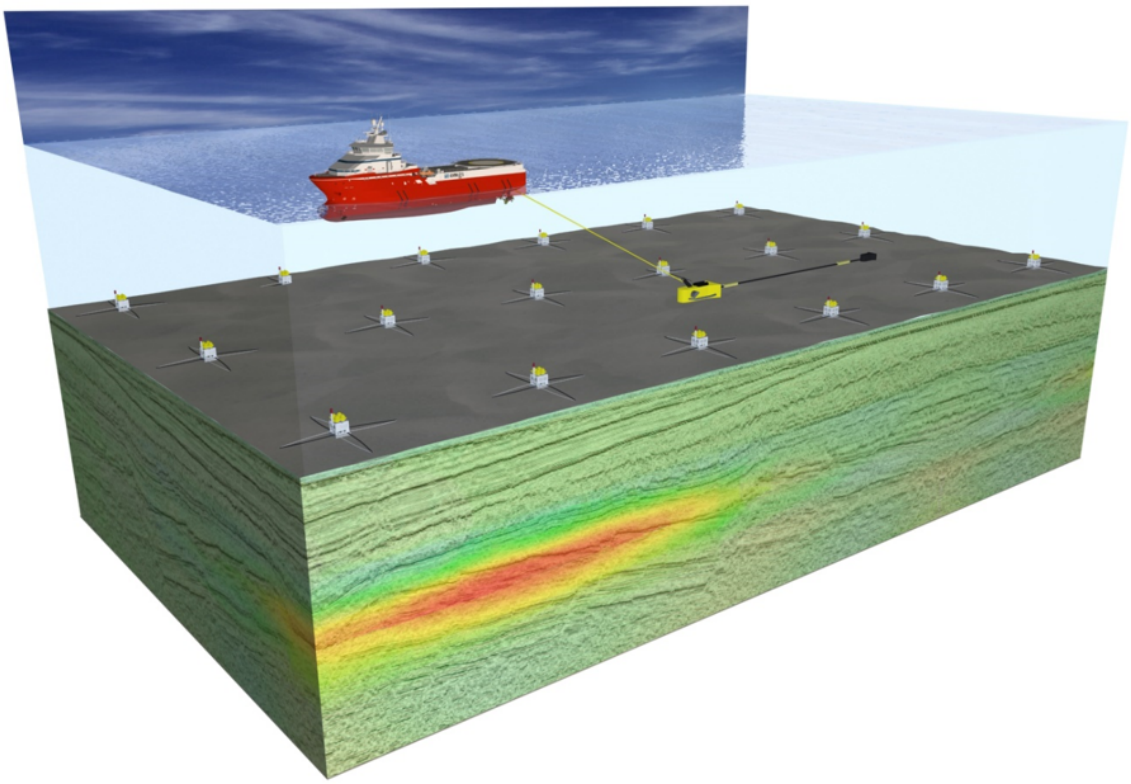

Figure 3.3: *Acquisition of marine 3D controlled source electromagnetic (CSEM) data with resulting resistivity model compared with seismic data. The receivers are placed at the seabed in a grid recording the electromagnetic signals emitted from the dipole source which is towed by the data acquisition vessel. In this illustration, red coloring represents high resistivities and blue coloring represents low resistivities. Figure modified from (Lindom et al., 2007).*

Figure 3.4 illustrates different energy pathways, from the active source to the receivers. Generally, the direct wave traveling directly from the source to the receivers dominate the electromagnetic signals at short source-receiver offsets. Energy from the subsurface starts to dominate the recordings with increasing offsets (Wicklund and Fanavoll, 2004). In shallow waters, the airwave, i.e. the energy traveling along the interface between the air and the seawater, tends to dominate the received signal at long source-receiver offsets (Eidesmo et al., 2002c). It is only the energy having penetrated the subsurface that is of interest, as this energy carries information about the geology.

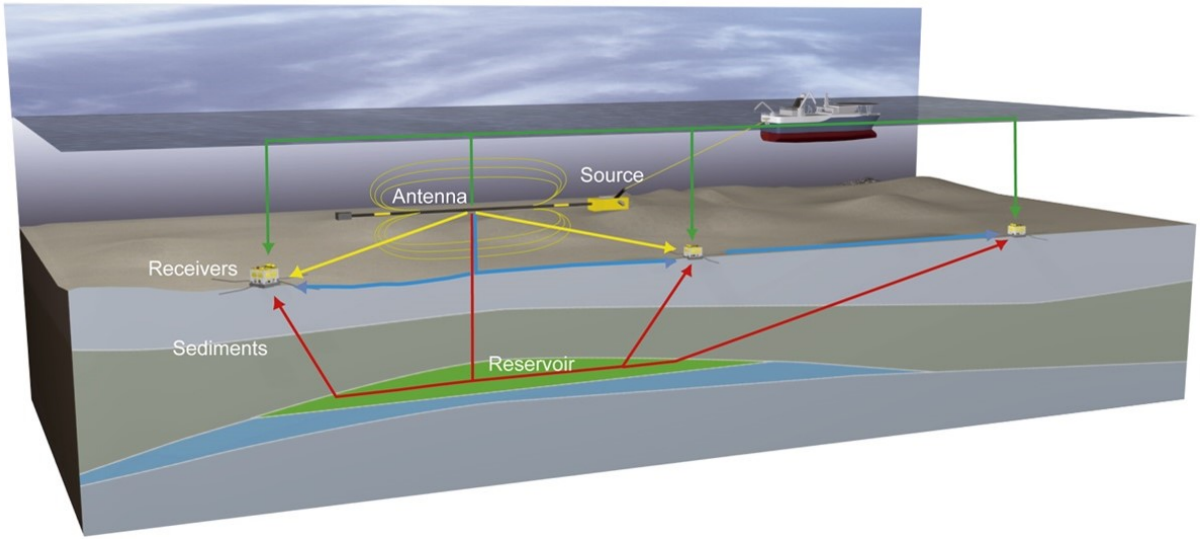

Figure 3.4: *CSEM energy pathways. The red arrows indicate the energy having penetrated the subsurface, the yellow indicate the direct energy and the green arrows represent the airwave. The direct wave dominates the electromagnetic signals at short offsets, whereas the airwave dominates at large offsets in shallow waters. Figure from (Vold et al., 2012) which has been modified from (Eidesmo et al., 2002a; Kong et al., 2002).*

As the source is constantly moving, the source and receiver antennas will form varying arrangements. Inline data is collected when the source and receiver antennas are in line with each other and broadside data is collected when the source and receiver antennas are parallel and perpendicular to each other. Azimuth receivers measure both inline and broadside data. Only inline data is recorded for 2D CSEM surveys. Broadside data, and consequently also azimuthal data is acquired for 3D surveys. (Eidesmo et al., 2002c; Ellingsrud et al., 2002; Johansen and Gabrielsen, 2015)

Resistivity is directional dependent. Due to anisotropy, the resistivity in the vertical direction is usually higher than the resistivity in the horizontal direction (Constable,

2010). This property can be utilized when interpreting the data. Inline data is mainly sensitive to the vertical resistivity component ρ_v. Thin, high resistive horizontal layers can be detected by inline data, whereas the broadside data measures the horizontal resistivity component ρ_h, i.e. the background trends. Thin, high resistive vertical layers, on the other hand, can be detected by the broadside data. 3D data acquisition is superior to 2D acquisition among others because both the resistivity components are taken into consideration. (MacGregor and Tomlinson, 2014; Johansen and Gabrielsen, 2015) Figure 3.5 illustrates the difference between inline, broadside and azimuth receiver configuration.

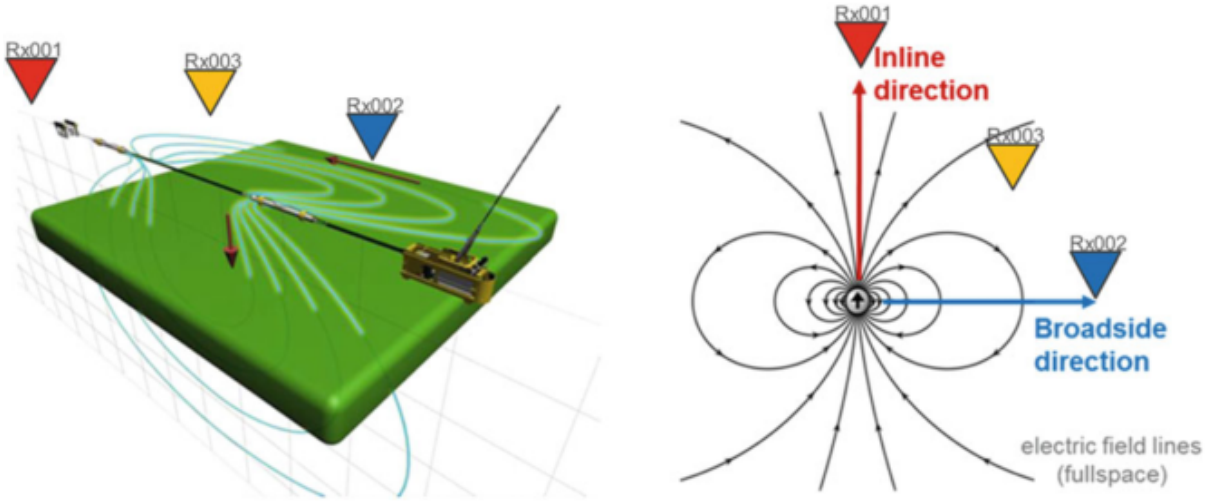

Figure 3.5: *Inline, broadside and azimuth receiver configuration. Inline data is acquired by receiver Rx001, broadside data is acquired by Rx002 and azimuthal data by Rx003. Inline data is sensitive to the vertical resistivity component and broadside data is sensitive to the horizontal resistivity component. The azimuth receiver records a combination of inline and broadside data. 2D surveys will only record inline data. Figure copied from (Johansen and Gabrielsen, 2015).*

3.1.3 Energy Attenuation

The transmitted CSEM energy is rapidly attenuated in conductive sediments. The energy propagates faster and is less attenuated in more resistive layers. Detection of guided waves through hydrocarbon reservoirs (see Figure 3.4), is the basis of using electromagnetic energy for hydrocarbon exploration (Eidesmo et al., 2002b). Low frequencies are utilized because these are attenuated less than high frequencies. Hence, CSEM is a low-resolution tool. The rate at which the energy is attenuated is determined by the skin depth given by

$$\delta = \sqrt{\frac{R}{\pi \mu f}} \approx 503 \times \sqrt{\frac{R}{f}} \tag{3.2}$$

where R represents the resistivity of the material, μ is the magnetic permittivity and f is the frequency. The skin depth is defined as the penetration depth required to attenuate the electromagnetic signal by a factor e^{-1} (about 37%) (Spies, 1989). The higher subsurface background resistivities, the higher frequencies are required to resolve high resistive features. With highly sensitive equipment, a resistive body buried several skin depths can be detected.

3.1.4 CSEM Workflow

Figure 3.6 shows the CSEM workflow. Prior to acquiring CSEM data, one or more sensitivity studies are performed with the aim to evaluate whether the defined target can be detected by the method. Through forward modeling, the expected CSEM response is calculated (Johansen et al., 2005; MacGregor and Tomlinson, 2014). The CSEM survey is designed based on the results of the sensitivity analysis. The data is acquired as described in Section 3.1.2. The acquired data is downloaded from the receivers and processed, both on board the acquisition vessel and on land. The raw data recorded in time series is for example calibrated and transformed into frequency domain through Fourier transformation and the receivers are mathematically rotated to become either inline or broadside oriented. Calculation of inline and broadside data is necessary for all receivers because the receivers sink freely down to the seabed causing randomly oriented antennas. Processed inline and broadside data are input to the inversion algorithm.

Attribute analysis is performed to directly analyze the data. Magnitude and phase plots are assessed to detect bad quality data and to evaluate the CSEM response from the subsurface prior to running inversions (Ellingsrud et al., 2002; Røsten et al., 2003). Inversion is performed in order to reproduce the earth's resistivity distribution. A more thorough explanation of inversion is given in the section below, Section 3.1.5. Interpretation of the resulting resistivity distribution involves explaining the observed resistivity changes and relating these to lithology and fluid effects. Integration of seismic, petrophysical data and established geological knowledge is essential as CSEM data provide low-resolution subsurface information, mainly on fluid type. As an example, seismic data can provide

additional information on strata and geological structures. (Johansen et al., 2008)

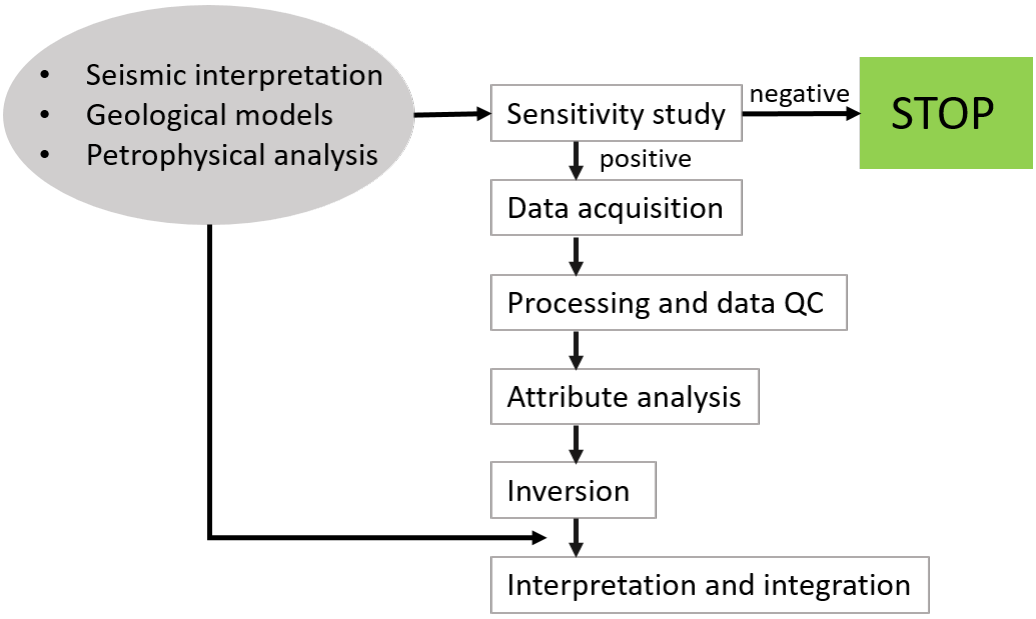

Figure 3.6: *CSEM data workflow – from sensitivity analysis through data acquisition, processing and attribute analysis to inversion and interpretation. In the inversion step, the earth's resistivity distribution is reproduced. In order to fully utilize the inverted CSEM data, integration of seismic data, petrophysical data and existing geological knowledge is necessary. See text for more explanation. Figure modified from (Johansen and Gabrielsen, 2015).*

3.1.5 Inversion of CSEM Data

The concept of inversion is summarized by Johansen and Gabrielsen (2015). Inversion is the process where the subsurface resistivity distribution is estimated from the acquired electromagnetic data. The problem is inverse; we want to obtain a parameter, the resistivity distribution, that is impossible to measure directly. A relationship between the electromagnetic data and the resistivity is necessary. Because of difficulties in obtaining this relationship, the problem is solved by iteratively finding the resistivity model that best explains the measured data (see Figure 3.7). Synthetic electromagnetic data is created from a resistivity model through forward modeling by using the same source- and receiver geometry identical to the actual data acquisition configuration. For the first iteration, a qualified guess of the resistivity distribution in the earth is used as the resistivity start model. Maxwell's equations are utilized in the forward modeling step. The synthetic data is compared with the acquired CSEM data for each iteration. The difference between

these data sets is termed data misfit, which explains how well the resistivity start model explains the measured data (Støren et al., 2008). If the misfit is unacceptable, the input resistivity model is updated and the synthetic data is again compared with the observed data. The final inverted resistivity model is obtained when the misfit is minimized, i.e. below a certain value of when it is done converging. The area is discretized on a regular grid, and through the inversion, the cells are updated and assigned resistivity values. For 3D CSEM data, the cells are assigned both vertical and horizontal resistivity values, but only vertical resistivities are obtained from 2D data. The results are among others dependent on the resistivity model used for the first iteration, possible constraints and different input parameters.

There is no unique solution to the inverse problem, i.e there are several resistivity models that can explain the measured electric and magnetic data. To limit the number of possible resistivity models and to stabilize the solution, regularization is introduced. Additional information is included in the inversion in order to obtain a geologically meaningful model (EMGS, ndb). The regularization is dependent on the strength of predetermined regularization parameters. As an example, the regularization can be designed to smooth the resistivity model more in the horizontal than in the vertical direction. Sediments are usually deposited approximately horizontally and it therefore makes sense to seek a horizontally layered model (Johansen and Gabrielsen, 2015). Both the data misfit and the regularization misfit, the total misfit, is minimized in the inversion. Regularization misfit describes the misfit between the resistivity within a cell and a reference value. A low total misfit means that the inverted resistivity model is close to what is measured by the receivers and that the resistivity distribution can be explained by geological models. (summarized by Spichak (2015))

An inversion workflow that uses the electromagnetic data itself is termed unconstrained inversion. The inversion is not influenced by any geological constraints; the resistivity results are functions of the measured data and the inversion input parameters. Constrained inversion, on the other hand, limits the inversion space by applying restrictions (Zach and Frenkel, 2009). Constraints can be applied by for example only allowing the inversion to update the resistivity model within a certain layer, defined through seismic interpretation. Figure 3.8 shows unconstrained and constrained inversion results. A major advantage of running constrained inversion is the improved spatial resolution compared to the unconstrained results. However, by including incorrect constraints, incorrect inversion results

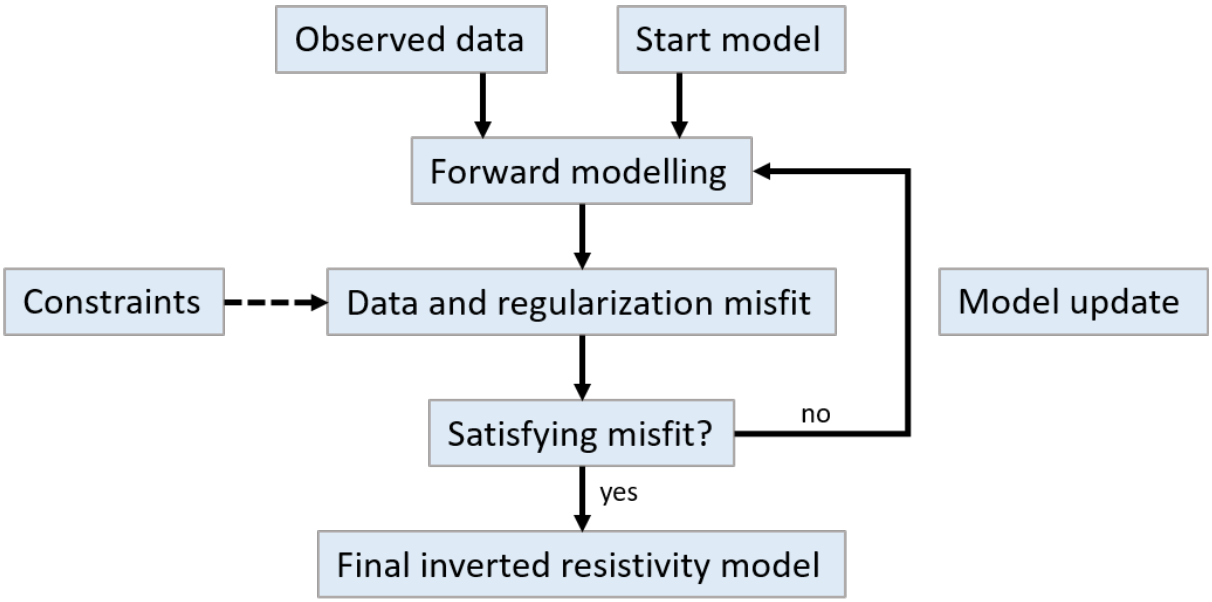

Figure 3.7: *Flow chart explaining the CSEM inversion workflow. For each iteration, synthetic electromagnetic data is created based on the input resistivity model and compared with the acquired CSEM data. The resistivity model is updated until the difference between the synthetic and the measured data, the data misfit, and the regularization misfit is minimized. An initial resistivity model, a start model, must be created for the first iteration. The inversion results can be directed by constraining the process. Figure modified from (Zach and Frenkel, 2009).*

will be created. A good geological understanding of the area in focus is for that reason essential. It is recommended to always perform an unconstrained inversion for comparison. (Harris and MacGregor, 2007; Johansen and Gabrielsen, 2015)

Inversions can be performed in 2.5D with the main objective of assessing the resistivity trends in the subsurface and to evaluate the resolution and data information for different frequencies, before running 3D inversion. The inversion is termed 2.5D because the 3D field is modeled in a 2D window. The advantage of using 2.5D approximation is that the number of unknown parameters in the inversion is reduced compared with 3D inversion. This allows for much faster forward modeling and implementation of more powerful algorithms applied to minimize the total misfit. The Gauss-Newton method is utilized in the forward modeling in 2.5D inversion. This algorithm is gradient-based and the second derivative of the misfit function is also calculated. Gradient-based means that the gradient of the misfit function with respect to changes in resistivity is calculated for each iteration. The Gauss-Newton algorithm is relatively robust and not much dependent on the input resistivity start model. (EMGS, nda)

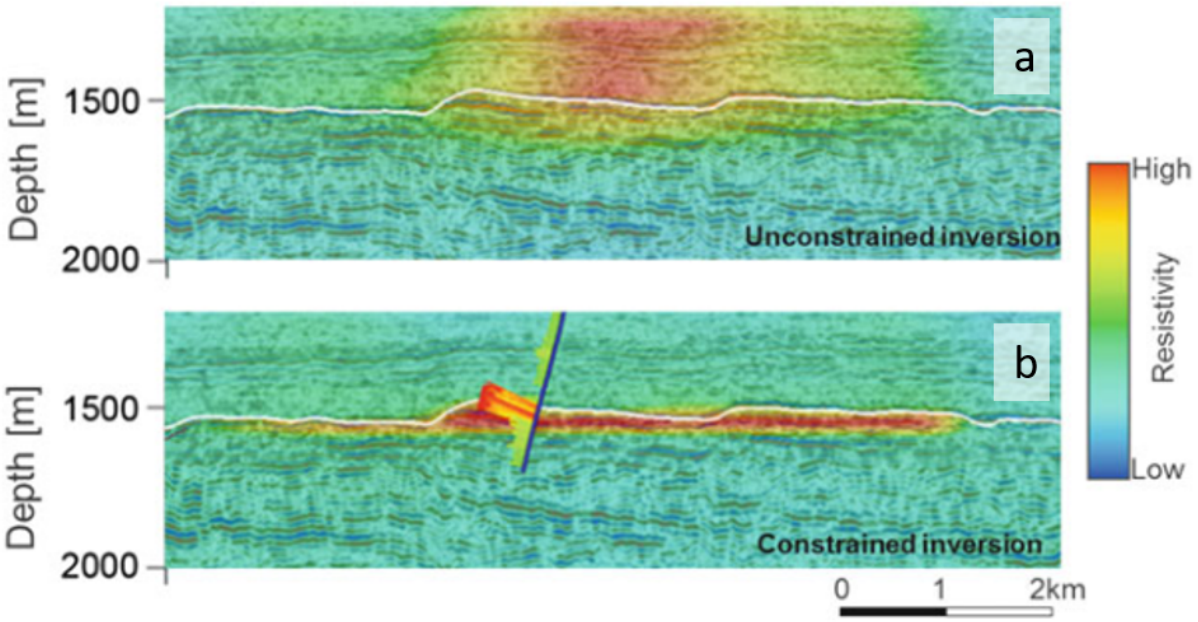

Figure 3.8: *CSEM inversion results from the Troll oil province in the North Sea. (a) Unconstrained and (b) constrained inversion results are overlain depth migrated seismic data. The blue line in (b) shows the location of the well. The constrained inversion has been run by allowing the inversion to mainly update the resistivity model within the reservoir defined by interpreted seismic horizons. Figure modified from (Morten et al., 2012).*

3D inversions are more time-consuming, computationally expensive and more sensitive to the start model compared with 2.5D inversion. A less powerful optimization method is therefore required for 3D. The Broyden-Fletcher-Goldfarb-Shanno (BFGS) method is implemented in the 3D inversion algorithm. The benefit of using the BFGS algorithm is that the computationally time is reduced because only the gradient of the misfit function is calculated. The algorithm requires however many iterations before the misfit converges. The consequence of utilizing a less powerful algorithm than for example the Gauss-Newton algorithm is more smeared resistivity anomalies and possibly more inaccurate depth estimations than in 2.5D. (Nguyen et al., 2016; EMGS, ndb)

3D inversion is superior to 2D inversion because more precise imaging of the earth's resistivity distribution is obtained. Both inline and broadside data is recorded in 3D, allowing detection of high resistive and high conductive bodies of any geometry. The benefits of 3D acquisition include increased vertical and horizontal resolution and hence improved hydrocarbon volume estimates compared with data in 2D (Danielsen and Bekker, 2011). Gauss-Newton and BFGS are numerical algorithms where the misfit function can end up

in a local minimum, i.e the misfit function has not been fully minimized (Nguyen et al., 2016). For that reason, it is very important to keep in mind that inversion results should not be considered as providing the true image of the earth's resistivity distribution, but rather an approximation to the measured CSEM data.

Parameter Testing

Parameter testing is an essential part of running inversions. The parameters are adjusted in order to give the most optimal image of the subsurface resistivity distribution. The model must among others be geological meaningful with a high signal-to-noise ratio. Some important parameters are frequency content, cell size, receiver grid spacing and regularization strength (Commer and Newman, 2008). To evaluate the influence the different parameters have on the imaging of the subsurface resistivities, established knowledge about the geology and on the CSEM method must be combined with the inversion results.

3.1.6 Data Sensitivity

The reservoir property to which the CSEM method is primarily sensitive is the anomalous transverse resistance (ATR). The method is also among others sensitive to prospect area, prospect burial depth, hydrocarbon saturation and the complexity of the background geology, as these properties affect the ATR values. Anomalous transverse resistance is defined as

$$\text{ATR} = \Delta z \times \Delta\rho = (z_{top} - z_{base}) \times (\rho_{target} - \rho_{background}) \tag{3.3}$$

where Δz is the thickness of the prospect and $\Delta\rho$ is the difference in resistivity between the target and the background geology (Baltar and Roth, 2013). It is the vertical resistivity that is useful for calculating ATR as the electromagnetic energy guided through hydrocarbon reservoirs is detected by the vertical resistivity component. The CSEM response from a 20-meter thick reservoir with a resistivity contrast of 60 Ωm is equal to the response from a 30-meter thick reservoir with a resistivity contrast of 40 Ωm. This in only valid for thin resistors with reservoir thickness below the CSEM resolution (Constable and

Weiss, 2006; Mittet and Morten, 2013). The sensitivity increases with larger ATR. For a given ATR, the sensitivity increases with decreasing target burial depth and/or increasing target area (Johansen et al., 2007; Mittet et al., 2008).

Depending on the geological setting, CSEM measurements can be sensitive to resistivity properties down to depth of several kilometers. The study performed by Mittet and Morten (2012) has proven that for a reservoir with a thickness of 50 meters and an average hydrocarbon saturation of 80%, the maximum burial depth with successful imaging is 2500 meters. The maximum depth of imaging is the maximum depth at which the main features of a resistive object is recovered by the inversion. The maximum depth of detection can be much larger than the maximum depth of imaging and is defined as the depth where the response from the resistive object equals the noise level. The CSEM equipment, software, processing algorithms and inversion schemes have been improved the last years, giving reason to believe that the maximum depth of imaging has increased.

3.2 Joint Interpretation of CSEM, Seismic and Petrophysical Data

The CSEM technique is not a stand-alone method. CSEM data is often acquired to add information which is not fully provided by other sources; seismic data, petrophysical data, information from cores and regional geological knowledge.

Petrophysics provide the necessary link between in situ reservoir measurements and measured data from remote sensing techniques. Well logs provide high-resolution measurements from the subsurface sediments and fluids, but are limited in areal extent. Remote geophysical methods are required in order to obtain the additional information from the areas between the wells. For hydrocarbon fields, this additional information is essential for reservoir management and production optimization. (MacGregor et al., 2010) Seismic sounding is the most commonly used geophysical method within hydrocarbon exploration. The relatively high-resolution seismic images are used to create geological models. Seismic data can detect strata and geological structures in the subsurface, but have problems identifying the fluid content (Eidesmo et al., 2002a). CSEM data has the advantage of being sensitive to high hydrocarbon saturations. Figure 3.9 shows that small fractions of

gas in the pore fluid can change the seismic velocity by a factor of two, whereas high saturations of gas is required before significant changes in resistivity are achieved (Constable, 2010). The P-wave velocity also decreases when oil substitutes water in a reservoir, but the velocity effect is less pronounced compared with gas. CSEM data can not be used to distinguish gas from oil (MacGregor et al., 2008). Seismic and CSEM are considered as complementary remote sensing methods as seismic data can not differentiate between high and low saturations of hydrocarbons, whereas CSEM data can.

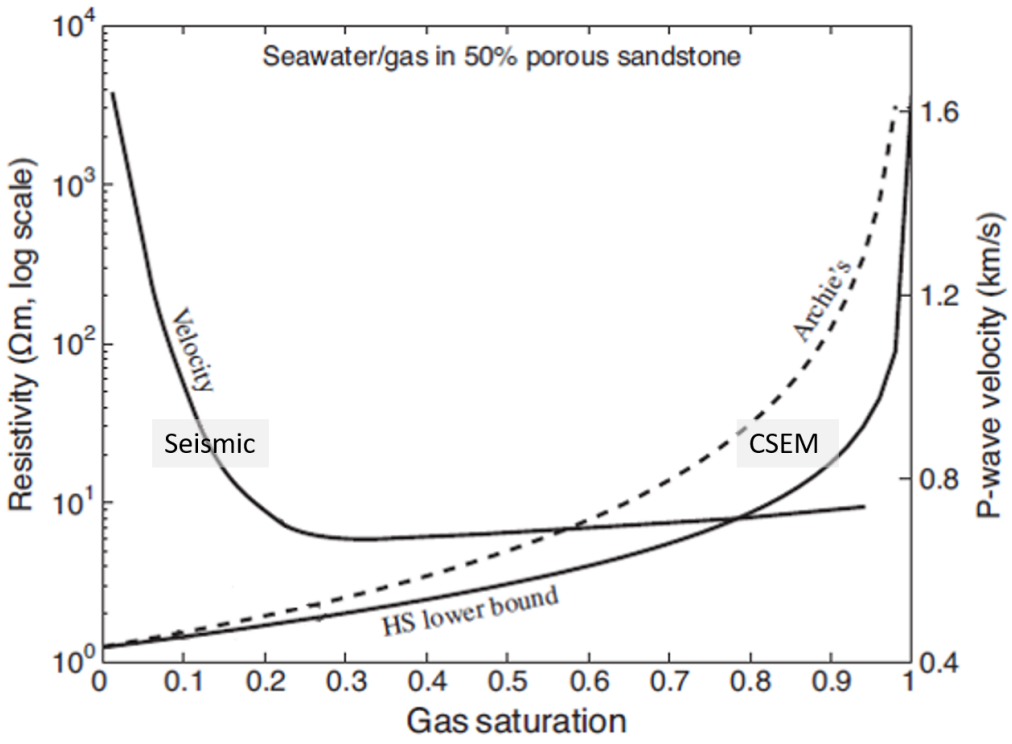

Figure 3.9: *Resistivity and P-wave velocity as functions of gas saturation for a 50% porous sandstone. The seismic velocity decreases when small amounts of gas are introduced into the pore space. The bulk resistivity increases drastically for high gas saturations, which also is the case for oil. The Hashin-Shtrikman (HS) effective medium model for resistivity is widely used, but Archie's law is provided as a reference. Figure modified from (Constable, 2010).*

By exploiting the strengths of each of the methods; CSEM, seismic and petrophysical data, estimates of rock and fluid properties can be obtained with greater confidence than from any one source of information alone. If only one type of data is considered, ambiguities can remain in the interpreted results. (Harris et al., 2009) High resistive anomalies in the CSEM data can be explained by several geological features (see Section 3.1.1), i.e. these anomalies do not necessarily coincide with accumulations of hydrocarbons. By combining

different data types with different resolutions and strengths, the number of possible explanations to observed resistive anomalies can be reduced. The more information provided, the lower the risk of drilling a dry well.

Chapter 4

Data

4.1 2D Seismic Data

The interpreted two-dimensional (2D) seismic data was comprised of three data sets; one from Multiclient Geophysical (MCG), one from the Norwegian Petroleum Directorate (NPD) and one survey acquired on behalf of Norsk Hydro (NH). The interpreted parts of the seismic data sets cover an area of about 640 km^2. The seismic data from MCG, MCG0901, has been in focus for the seismic interpretation as the data is relatively newly processed. The survey was acquired in 2009 in the eastern part of the Bjørnøya Basin, but covers also parts of Bjørnøya Fault Complex, Veslemøy High, Tromsø Basin and Ringvassøy-Loppa Fault Complex. These interpreted lines are oriented in the NE-SW direction, parallel to the fault strike associated with the Bjørnøyarenna Fault Complex. The seismic line spacing is 4 kilometers. The data set was reprocessed by PSS-Geo in 2012. The sampling interval and bin spacing are 4 ms and 12.5 m respectively. Radon transform has been used for multiple attenuation before application of pre-stack time migration using the Kirchhoff algorithm. The vertical resolution has been calculated from

$$\text{Vertical resolution} = \frac{\lambda}{4} = \frac{v}{4f} \tag{4.1}$$

where λ is the wavelength of the sound wave, f is the dominant frequency and v represents the velocity. The vertical resolution at the reservoir level ranges from 15 m to 35 m. The

values are based on measured velocities from well 7319/12-1 of 2345 - 2771 m/s and by using 20 - 40 Hz as a dominant frequency range. The range for vertical velocity is quite wide because the velocity and dominant frequency vary a lot at this level. Geological layers with a thickness below $^1/_4$ of the wavelength, here with an average value of 25 m, can not be resolved. The seismic resolution is poorer at depths below the reservoir while increasing towards the seabed. This makes sense because the seismic waves are attenuated as they penetrate the subsurface, mainly due to geometrical spreading, absorption and transmission loss. The frequency content is dominated by low frequencies at large depths because high frequencies are attenuated more than low frequencies.

Five 2D seismic lines from Norsk Hydro acquired in 1985 cross the Pingvin discovery. The data is sampled every 4 ms. Despite the age of the data set, the vertical seismic resolution at the reservoir level is close to that of the reprocessed MCG data from 2012. The data quality at larger depths is however much better for the MCG data. The Norsk Hydro seismic lines have been shifted up by 14 ms prior to performing seismic interpretation to match the two-way traveltime for the top reservoir reflector in the MCG data.

In order to tie the MCG and NH seismic lines together, two 2D seismic lines from NPD's survey NPD-BJRE-BJSY-84 acquired in 1984 have been utilized. The data was processed in 1985 with a sampling rate of 4 ms. In large because of the age and the processing algorithm used, the data quality and vertical resolution of this data are significantly worse compared with the MCG seismic. The two NPD lines have been shifted up by 13 ms by using the MCG data as a reference.

Figure 4.1 shows the Bjørnøya Basin and the surrounding basins, highs and fault complexes, in addition to the available MCG, NH and NPD 2D seismic lines. The parts of the seismic lines used for seismic interpretation for this project are shown.

4.2 Petrophysical Data

Petrophysical data from exploration well 7319/12-1 has been available throughout the project. Gas was encountered at 953 meters measured depth (MD) and the final vertical drilled depth was 1540 meters. The kelly bushing elevation is 40 meters. The Cretaceous Kolmule Formation is the oldest penetrated formation. The water depth at the well location is 422 meters. The well was drilled with KCl/polymer/GEM water-based mud,

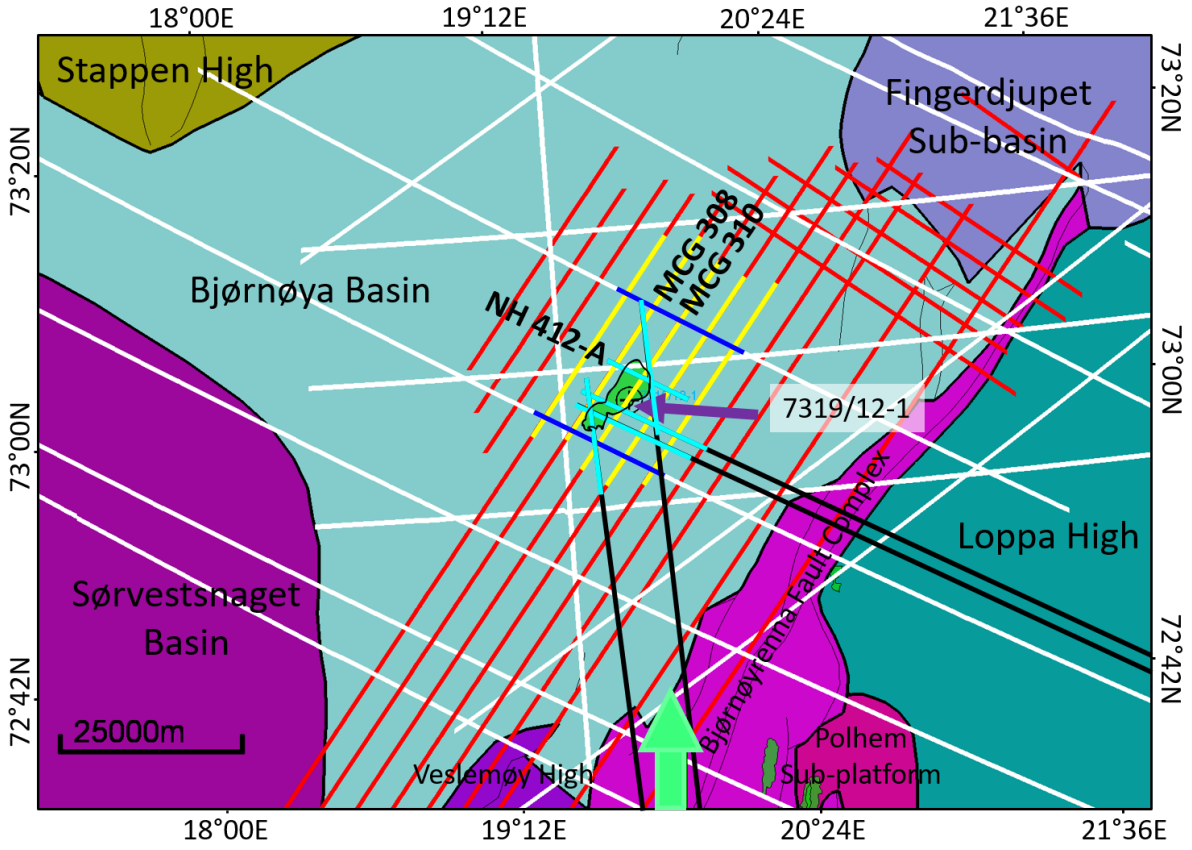

Figure 4.1: *Structural elements in the Southwestern Barents Sea and seismic data coverage. The yellow, the turquoise and the blue seismic sections show the parts of the red Multiclient Geophysical (MCG) lines, the black Norsk Hydro (NH) lines and the white Norwegian Petroleum Directorate (NPD) lines respectively used for seismic interpretation. The shape of the discoveries have been downloaded from Norwegian Petroleum Directorate (nde) and are shown in bright green. The purple arrow indicates the position of well 7319/12-1, penetrating the Pingvin discovery.*

among others to prevent swelling of clay and to protect the borehole and the cuttings. In this study, the well is regarded as vertical as the maximum wellbore inclination is only 2°. Three cores with a total length of 17.61 meters were cut in the interval between 965.5 to 988.1 meters MD. Core photos have not been available. Fluid samples were acquired at 961.9 m, 973.2 m and 976.3 m MD, saturated with gas, water and water respectively. (Norwegian Petroleum Directorate, ndg) Multiple well logs have been accessible, with the most important being gamma ray, spectral gamma ray, density, neutron porosity, resistivity with micro, medium and deep measurements and measurements from nuclear magnetic resonance (NMR) logging. In addition, elemental capture spectroscopy (ECS) logs have

been important. The NMR measurements have been acquired from another wireline run than the other listed measurements. There is, however, no significant difference in depth between the runs. Figure 4.2 shows that responses from the NMR porosity curve coincide with the response from the density, neutron porosity and resistivity curves at the same depths.

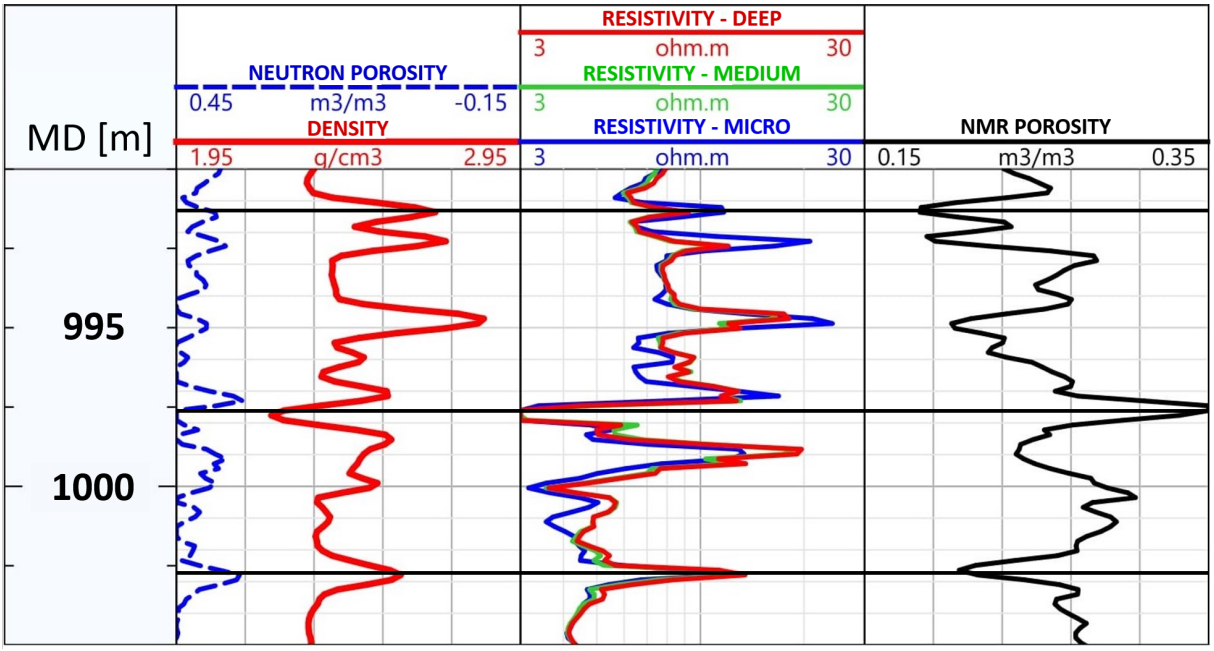

Figure 4.2: *Quality control of nuclear magnetic resonance (NMR) log. The well section shows that no depth shift of the NMR porosity curve is required. The depths of the NMR porosity spikes coincide with the density, neutron porosity and resistivity spikes. The black horizontal lines are added in order to better see the match between the curves. This well section shows measurements from the underburden, at a measured depth of 990 to 1005 meters measured depth.*

Logger's depth describes the well depth values used as a reference for all wireline operations. The depths of the cores are however measured in drillers depth. Driller's depth is the depth measured while drilling. The total depth to the point of interest is provided by adding the measured length of each joint of pipeline or tubing. The difference in depth between logger's depth and driller's depth is a result of stretch in the wireline and the drill string. Core plugs have only been acquired from an interval of 17.61 meters, limiting the basis of evaluating whether the depths of the core measurements coincide with the depth of the well logs. Density measurements from core analysis and from NMR measurements indicate however that the density in the reservoir sand is lower than the density of the underburden shale. Based on the provided information, there is no reason to depth shift the core measurements.

Fluid saturation analyses were performed on the core plugs by the Dean-Stark method. The results were corrected for mud invasion with the presumption that the total calculated volume of invaded mud filtrate has replaced hydrocarbons only. This presumption is incorrect, as there was mobile water in several of the core plugs. The mud would have replaced this mobile water, and not only gas as presumed. The corrected water saturation values are consequently much lower than the true water saturation values. Because of this, the water saturation measurements from the core plugs have been regarded as unreliable.

The bit size and caliper log measurements have given little indication of mudcake buildup or borehole washout, except for an interval from 1001 to 1007 meters MD with relatively poor borehole conditions. There are uncertainties regarding the quality of the well logs within this interval, but the reservoir, which has been in focus for this project, does not appear to be affected by any borehole instabilities.

4.3 3D CSEM Data

The CSEM data used is comprised of two three-dimensional (3D) CSEM data sets, in parts survey BSTEN04 and in parts survey BSTEN05. The surveys are multi-client data sets, acquired by EMGS in 2010 and reprocessed in 2013, also by EMGS. Figures 4.3 and 4.4 show the merged CSEM data set used for unconstrained and constrained inversion respectively, the position of well 7319/12-1 and the bathymetry map. Inline, broadside and azimuth measurements from fewer receivers have been included for constrained inversion than for unconstrained inversion. The receivers have been deployed at water depths ranging from 402 to 462 meters, and with a planned receiver spacing of three kilometers. According to the data acquisition reports, the median receiver deviation for BSTEN04 were 20 meters and 40 meters for BSTEN05. It is not the planned receiver positions that are input to inversion, but the actual receiver positions. The data sets were acquired with a dipole length of 264.7 and 271.8 meters and an average source strength of 1172 and 1167 ampere, respectively for survey BSTEN04 and BSTEN05.

The quality of the data for each receiver has been evaluated through running inversions and is presented in Section 6.5.1. The overall quality of the available 3D CSEM data has been regarded as good.

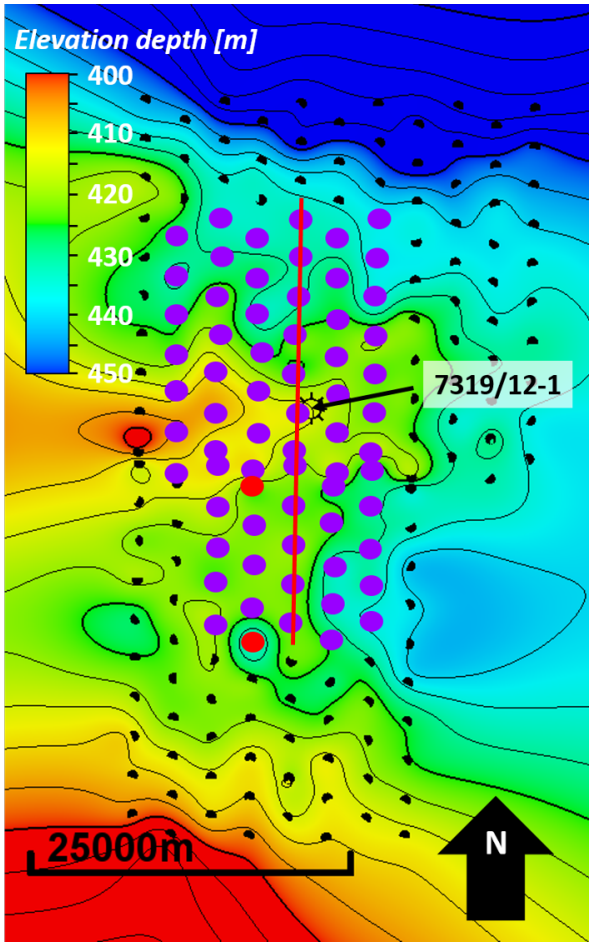

Figure 4.3: *Merged CSEM data set with receivers from surveys BSTEN04 and BSTEN05 (black circles) and bathymetry map. The purple dots indicate the receivers used for unconstrained inversion. The red circles indicate receivers removed from the data set. Data from the black receivers has not been used. The red line represents a section crossing the Pingvin discovery.*

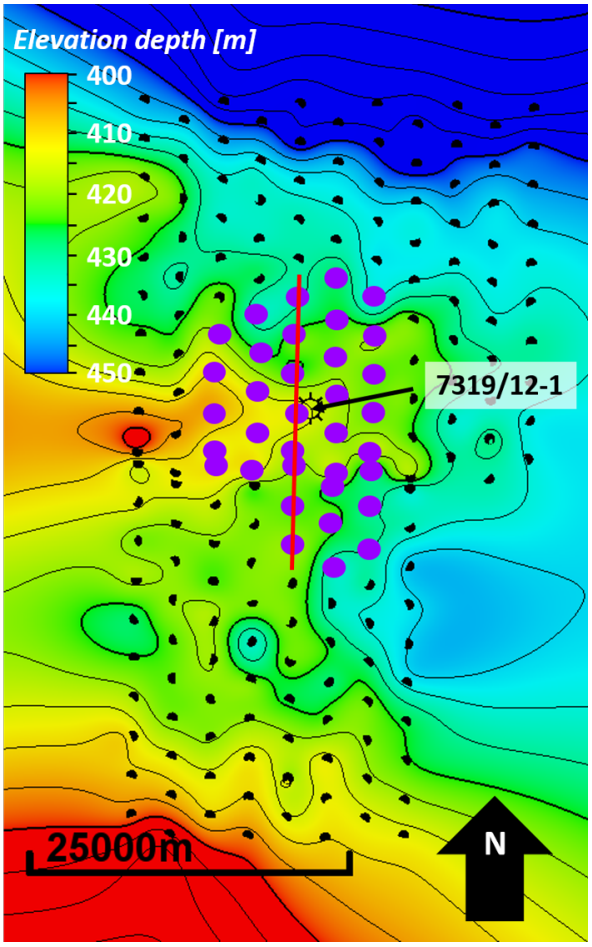

Figure 4.4: *Merged CSEM data set with receivers from surveys BSTEN04 and BSTEN05 (black circles) and bathymetry map. The purple dots indicate the receivers used for constrained inversion. Data from the black receivers has not been used. The red line represents a section crossing the Pingvin discovery.*

Chapter 5

Method

The method used for this project was divided into four distinct sections and is summarized in Figure 5.1. Results from seismic interpretation and petrophysical analysis were used in combination with results from unconstrained and constrained 3D CSEM inversions to say something about the reservoir quality. The seismic interpretation has involved investigation of the evolution of the basin, characterization of the seismic anomaly associated with the reservoir, interpretation of the top reservoir surface and seismic depth conversion. Results from petrophysical analysis have been important for the seismic depth conversion. Lithology and fluid identification and porosity and water saturation estimation have been regarded for the petrophysical analysis. Information on resistivity from well logs has been used in the CSEM inversion. The seismically derived top reservoir surface has been used as input to the constrained CSEM inversion. An anomalous transverse resistance (ATR) map has been created based on these inversion results. Rock physics models have been established by upscaling well logs to CSEM resolution and creating relationships between ATR and gross pay. Gross pay maps have been created by combining these relationships with the ATR map. Reservoir quality has been interpreted based on the resulting gross pay maps and the reservoir thickness interpreted from the seismic data. This chapter provides a more detailed description of this method. Continuous interpretation of the results have been important. The method used for qualitative and quantitative interpretation of reservoir quality presented in this thesis is based on the work performed by Morten et al. (2017) and Granli et al. (2017).

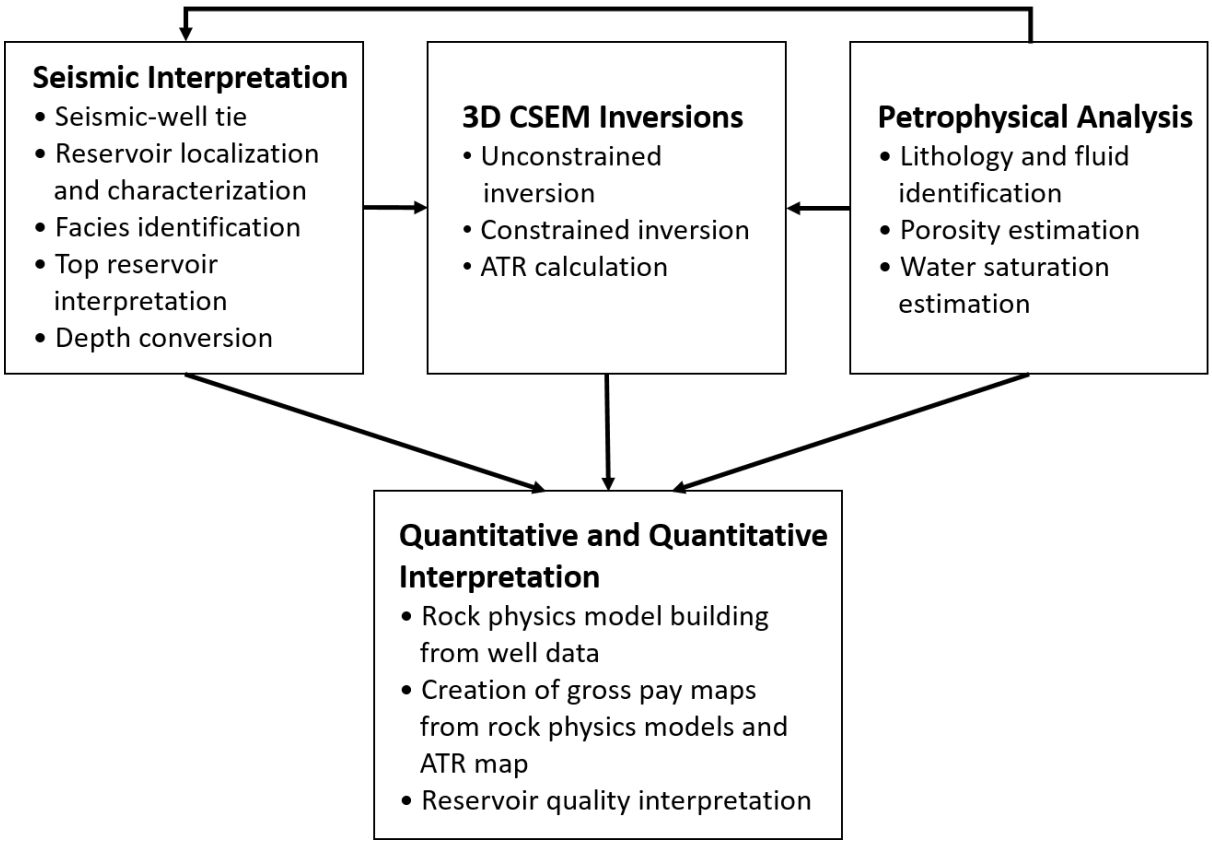

Figure 5.1: *Project workflow. Seismic and petrophysical interpretation have been combined with 3D CSEM inversion results for qualitative and quantitative interpretation of the reservoir. Through seismic interpretation, the depositional setting in the basin has been investigated, the fluid anomaly has been interpreted, the top reservoir surface has been extracted and seismic depth conversion has been performed. Information from well logs has been important for the seismic depth conversion. The resistivity distribution in the subsurface has been estimated from CSEM inversions. The seismically derived top reservoir surface has been used as input to the constrained inversion. An anomalous transverse resistance (ATR) map has been created based on these inversion results. Lithology and fluid have been identified and porosity and water saturation have been estimated in the petrophysical analysis. Measurements from the well data have been used as input to the CSEM inversion. Rock physics models have been established from the well data by creating relationships between ATR and gross pay. These relationships have been combined with the ATR map to create gross pay maps. Reservoir quality has been interpreted based on the gross pay maps and the reservoir thickness interpreted from the seismic data.*

5.1 Seismic-Well Tie

Seismic-well tie has been performed to relate formation tops identified in the well with seismic reflectors from one seismic line. Well data is measured in units of depth and seismic data is measured in time and it was therefore necessary to establish a time-depth relationship. Check-shot data, which is borehole seismic data, together with sonic and density logs have been correlated to surface seismic data by generating a synthetic seismogram. The synthetic trace has been compared with the seismic data at the well location.

The time-depth relationship has been established by calibrating the sonic log with check-shot data. A calibrated curve, a drift curve, has been fitted to the difference between the sonic log times and the check-shot times. The drift curve has been applied to the sonic log to fit the check-shot data (Stewart et al., 1984). The vertical resolution of the sonic log data is much higher than that of the seismic data. Despiking of the sonic log has for that reason been performed prior to the establishment of the time-depth relationship to avoid erroneous calculations. Ideally, the density log should also be edited, but this has not been done for this project. (White and Simm, 2003)

Convolution is a key concept in creating the synthetic seismogram. The synthetic seismic trace has been created by convolving the reflection coefficient with the wavelet, which is the Earth's impulse response. The convolutional model is presented by

$$\text{Seismic trace(t)} \;=\; \text{Reflection coefficient(t)} \;*\; \text{Wavelet(t)} \;+\; \text{Noise(t)} \qquad (5.1)$$

The corrected sonic log and the density log have been combined in an acoustic impedance log. Reflection coefficients have been calculated for changes in acoustic impedance, which have been combined with the earth's impulse response to generate the synthetic seismogram (White and Simm, 2003). This approach is illustrated in Figure 5.2.

Figure 5.2 assumes that the polarity of the seismic data is SEG normal (American convention), i.e. an increase in acoustic impedance gives positive seismic amplitude. European convention assumes the opposite. The figure also illustrates zero phase where the majority of the energy is concentrated in the center of where there are changes in acoustic impedance. A major advantage with zero phase data is that it tends to provide sharper

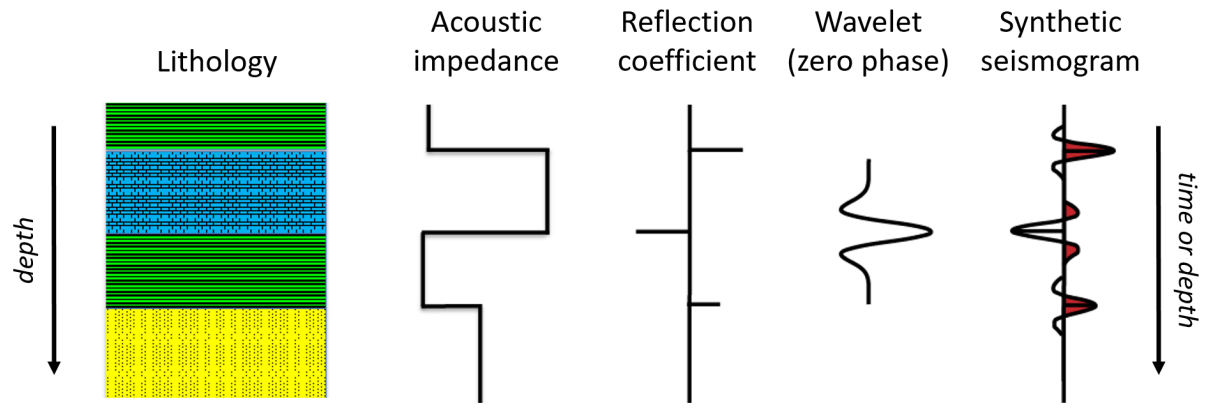

Figure 5.2: *General generation of synthetic seismogram. The acoustic impedance log has been created at facies contrasts from edited sonic and density well logs. Reflection coefficients have been calculated and convolved with the wavelet to create the synthetic seismogram (see Equation 5.1). Notice that the seismogram in this figure is in zero phase and has SEG normal polarity convention. Figure modified from (White and Simm, 2003).*

definitions and less noise between stratigraphic features than minimum phase data (Simm and White, 2002).

The resulting synthetic seismogram has been compared with the seismic data. The 2D seismic section closest to the well has been used as a reference to fit the synthetic seismogram to the nearest seismic trace (see Figure 5.3). The tie that gave the best character tie with the least shift in time at the depth of interest has been accepted.

5.2 Seismic Interpretation

2D seismic data has been interpreted in order to understand the evolution of the Bjørnøya Basin and for interpretation and extraction of the top reservoir surface. The interpretation has involved identification of seismic facies and identification of the high amplitude anomaly associated with the Pingvin discovery. The characteristics of the interpreted seismic units and created facies thickness maps have been used for establishing a geological history. Late Cretaceous and Tertiary sediments have been in focus for this project.

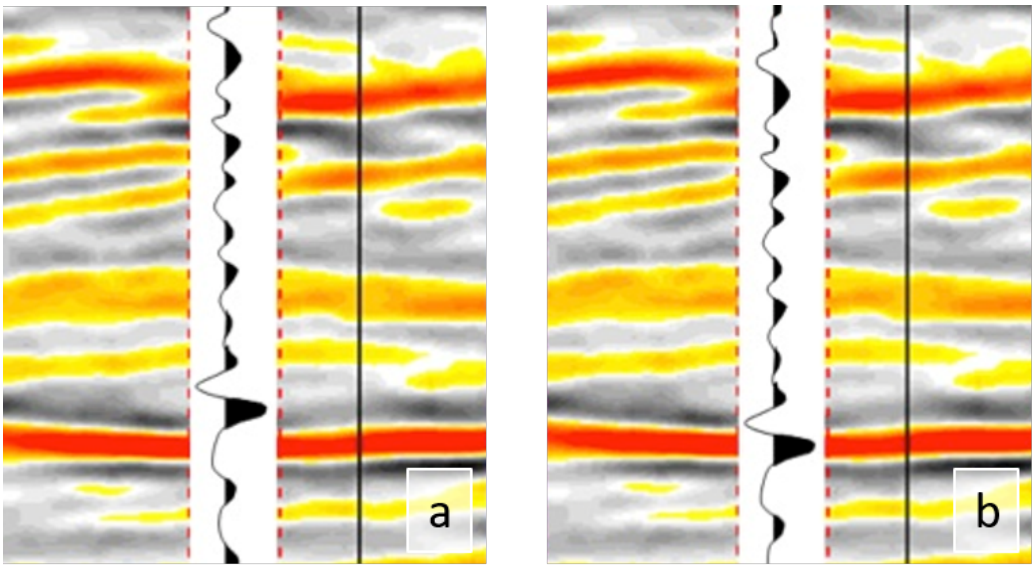

Figure 5.3: *Synthetic seismogram shift. The original synthetic seismogram in (a) has been shifted in time to get the best character tie, which is shown in (b). The peaks in the synthetic seismogram match with the peaks (red and yellow color) in the seismic data. The same applies for the troughs. Figure modified from (Schroeder, nd).*

5.2.1 Seismic Facies Analysis

The area of interest has been interpreted by identifying units with distinct seismic characteristics, different from the neighboring units. Seismic facies have been described and interpreted based on the seismic parameters; amplitude, continuity, configuration and frequency. The facies have been interpreted in terms of depositional environment. Internal reflection organization and lateral extent of the facies have been considered.

Frequency describes the vertical change in seismic reflector spacing and bed thickness. The frequency usually decreases with depth, mainly because of decreasing seismic resolution. Amplitude can give information on sediment type. The higher the amplitude, the larger the acoustic impedance contrast. Continuity of reflectors is usually associated with the lateral extension of the deposits. The presence of discontinuous reflectors often indicates rapid change in energy level, e.g. braided or meandering river deposits. The internal reflection pattern, or configuration, can provide information on depositional processes and stratification. Parallel to wavy reflections implies uniform sedimentation conditions. Chaotic areas are composed of discontinuous reflectors with varying amplitude and frequency. Disorganized reflectors and consequently sediments, may occur in multiple

depositional settings, examples are channel fill in a proximal fan or slumped deposits on a slope. Seismic facies analysis has been summarized by Veeken (2007). See Figure 5.4 for seismic facies characterized in terms of continuity, amplitude and frequency and Figure 5.5 for different reflection configurations.

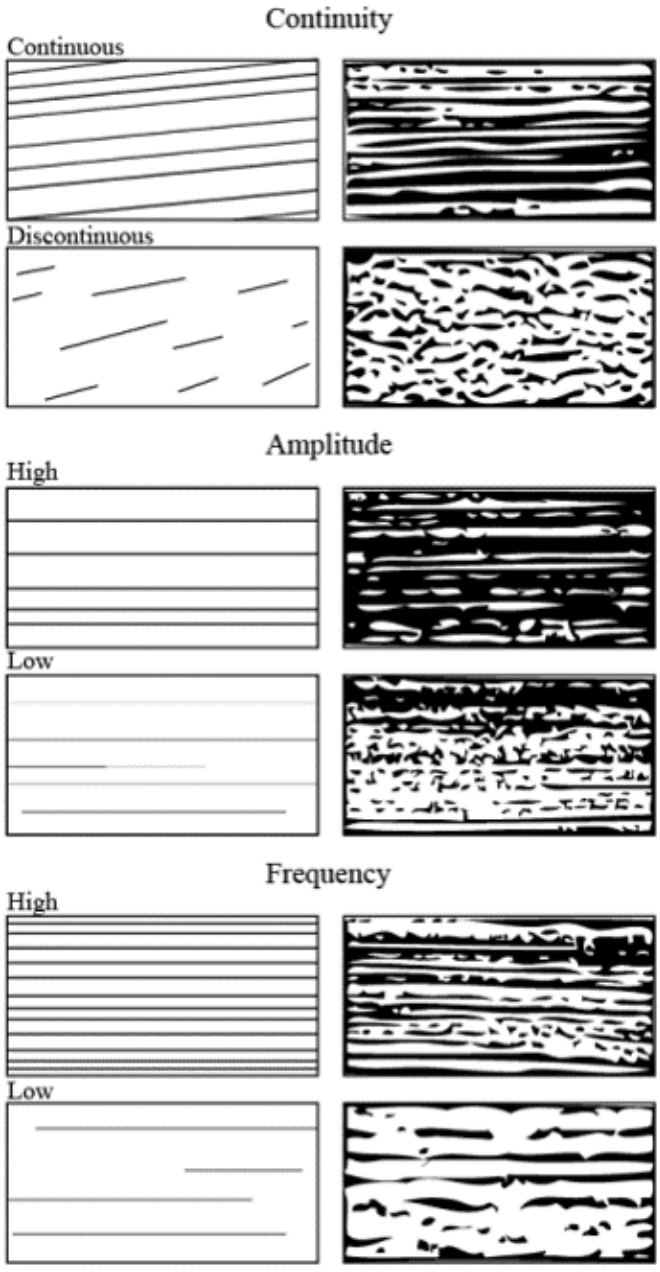

Figure 5.4: *Seismic reflection attributes. The seismic data has been interpreted and facies units have been identified based on continuity, amplitude and frequency. See text for more explanation. Figure modified from (Veeken, 2007).*

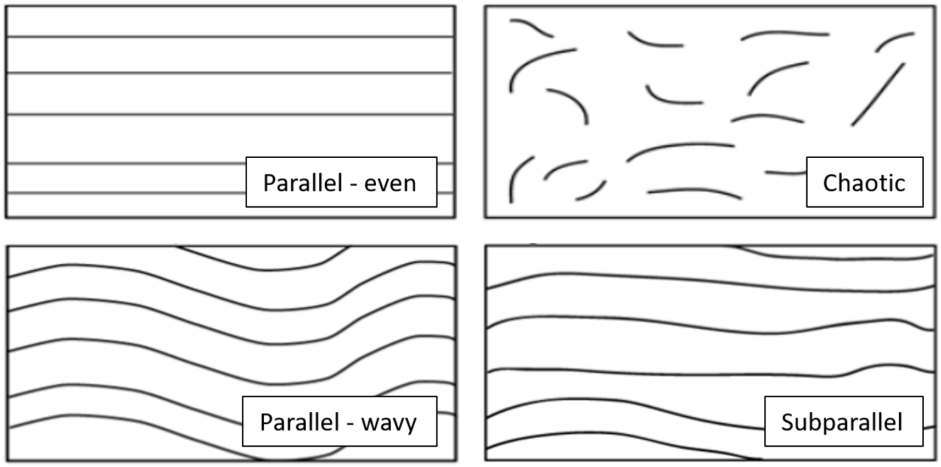

Figure 5.5: *Seismic reflection configurations. The figure illustrates parallel (even and wavy), chaotic and subparallel configurations. Divergent, hummocky and clinoforms are example of other geometries. Figure modified from (Veeken, 2007).*

5.2.2 Horizon Interpretation

In stratigraphic interpretation, the idea is that the different seismic facies units are bounded by surfaces representing time lines. These bounding surfaces have mainly been chosen based on their continuity, amplitude, internal facies characteristics and reflection termination pattern. Typical reflection termination patterns are onlap, toplap, downlap and erosional truncation (Mitchum et al., 1977). The most prominent reflectors were chosen instead of interpreting the formation tops encountered by the well as the main objective with the seismic interpretation was to understand the depositional history in the area. The horizon corresponding to the top reservoir has been thoroughly interpreted for several seismic sections.

5.2.3 Identification of Direct Hydrocarbon Indicators

Direct hydrocarbon indicators (DHIs) are within seismic described as anomalous seismic responses caused by the presence of hydrocarbons. Such seismic anomalies are created as a result of changing elastic rock properties caused by pore fluid changes that are seismically detectable. DHIs have been identified based on the presence of flat spots, bright spots, chimney effects and seismic polarity reversal (Veeken, 2007).

High-amplitude anomalies can be related to lithology or to fluid effects. The nature of the

seabed reflector has been used as a reference for differentiation. The acoustic impedance is larger at the seabed than that in the water layer. Seabed reflectors are caused by lithology effects and fluid effects are therefore expected to exhibit opposite amplitude characteristics. For SEG normal polarity, high-amplitude anomalies represented by a trough, so-called "soft" events, can result from hydrocarbon leakage or accumulations (Avseth et al., 2005).

5.3 Seismic Depth Conversion

The seismic data has been interpreted in two-way traveltime. The associated surface of the interpreted top reservoir horizon has been used as input to the constrained CSEM inversion. The electromagnetic energy from the CSEM data is a function of depth and depth conversion of the seismically derived top reservoir has therefore been necessary. In order to compare the CSEM inversion results with the seismic data, seismic 2D sections crossing the reservoir have also been depth converted. The depth conversion results, especially the depth conversion of the seismic sections, are dependent on the velocity at all depths. Input seismic surfaces to the velocity model have therefore been interpreted for several seismic 2D lines and to the depth corresponding to about 8000 ms.

Tertiary sediments show a broad range of velocities (Richardsen et al., 1993). Interval velocities from the time-depth relationship created from seismic-well tie have therefore been used for the layers penetrated by the well. These velocities have been extracted from the data itself. For the older and deeper deposits, the interval velocities have been estimated from sonic measurements from composite logs from surrounding wells (Norwegian Petroleum Directorate, ndb). Different interval velocities were tested with the aim to match the seismically derived top reservoir surface with the top reservoir position identified from the well data. It has been assumed that the velocities and the associated uncertainties increase with depth. Table 5.1 shows the set-up of the velocity model. The quality of the depth conversion has been evaluated based on the match between the depth converted top reservoir surface and the top reservoir position in the well.

Table 5.1: *Set-up of velocity model for seismic depth conversion. The seismic packages penetrated by the well have been assigned velocities obtained from the time-depth relationship created through seismic-well tie. Constant interval velocities have been assigned to the deepest surfaces. No well corrections have been applied for the seismic surfaces not penetrated by the well.*

Seismic surface	Correction – Well tops	Velocity model	
Seabed	Associated Gr. or Fm.	V = V0 = Vint	V0: Well TDR – Constant
Seismic surface 1	Associated Gr. or Fm.	V = V0 = Vint	V0: Well TDR – Constant
Seismic surface 2	Associated Gr. or Fm.	V = V0 = Vint	V0: Well TDR – Constant
Seismic surface 3		V = V0 = Vint	V0 = Constant = ... m/s

5.4 Petrophysical Evaluation Workflow

Petrophysical analysis has been performed with the aim to extract reservoir properties at the well location for establishing rock physics models. Well log interpretation has included getting an overview of the data availability and quality, identification of permeable zones, lithologies and fluid types and estimation of porosity and water saturation. Porosity and water saturation are among the rock properties which are not possible to measure directly, and the relations used to calculate these properties from measurable parameters are empirically developed (Worthington, 2011). Keep in mind that the geology is infinitely more complex than what can be measured in the wellbore. See Ellis and Singer (2007) for information on different well logging tools, techniques and measurements. Notice that if the thicknesses of the beds are less than the log resolution, log measurements represent an average of several beds. The vertical resolution for the different well logs ranges from a few centimeters to several meters (Nelson and Mitchell, 1990).

5.4.1 Identification of Permeable/Impermeable Zones

The T2 distribution based on the nuclear magnetic resonance (NMR) tool and separation between the micro, medium and the deep resistivity measurements have been used as permeability indicators. The T2 distribution gives responses in terms of the size of the

pores and in terms of permeability. The larger the pores, the more free fluid and higher permeability (Allen et al., 1997). Separated resistivity curves means that the different measurements have measured different substances, indicating permeability and invasion of mud filtrate to the formation. Perfectly overlapping resistivity curves indicates no invasion of mud filtrate and no permeability. Overlapping resistivity curves can only be linked with impermeability when the salinity of the formation water is different from the salinity of the drilling mud. (Ellis and Singer, 2007)

5.4.2 Lithology Identification

Physical rock samples are preferred for unambiguously determine formation lithology. Rock sampling is however not a continuous measurement. Well logs have been analyzed in combination with results from rock samples to identify the rock types and the variations in mineralogy with depth. Lithological description from core samples and information on mineralogy from the gamma ray (GR) tool, the elemental capture spectroscopy (ECS) tool, in addition to information from different cross-plots and neutron-density separation, have principally been used for determining formation lithology. Investigation of the type of minerals contained within the reservoir has been important in order to understand the well log responses. The gamma ray log has provided knowledge on the presence of clay and minerals like micas and feldspar. The cross-plots used have been found from Schlumberger (2009): LITH-1B presented in Figure A.1 and LITH-2 in Figure A.2. Determining the mineralogy within the reservoir has been necessary for estimation of the bulk volume fraction of clay and shale and for estimation of porosity and water saturation.

5.4.3 Shaly Sand Deposits

Identifying the type of lithology from well logs is relatively straight forward if one has a relatively good understanding of the surrounding geology and if the encountered formations are clean, i.e. with little to no clay content. Most sediments are deposited along with some clay and understanding how clay affects the different well logs is therefore necessary. The presence of shale in hydrocarbon reservoirs can largely impact the reservoir quality and the estimates of reserves. Saturation and porosity estimation is complicated by the clay minerals present within the shale. In addition, the distribution of clay usually varies

and often there are multiple clay mineral types present. (Ellis and Singer, 2007)

A common misconception is that shales are composed of 100% clay, the two terms are often used interchangeably by geoscientists. Shale is a fine-grained rock consisting of different minerals and with a sizable fraction of clay minerals (Ellis and Singer, 2007). Bhuyan and Passey (1994) estimated in 2008 clay volume from gamma ray and neutron-density porosity logs. The study showed that the shales were composed of 50-70% clay, 25-45% silt- and clay-sized quartz and 5% other minerals including feldspar and carbonates. According to La Vigne et al. (1994), formations identified as shales typically contain between 35 and 70% clay. Figure 5.6 illustrates the elements of a shaly sand reservoir.

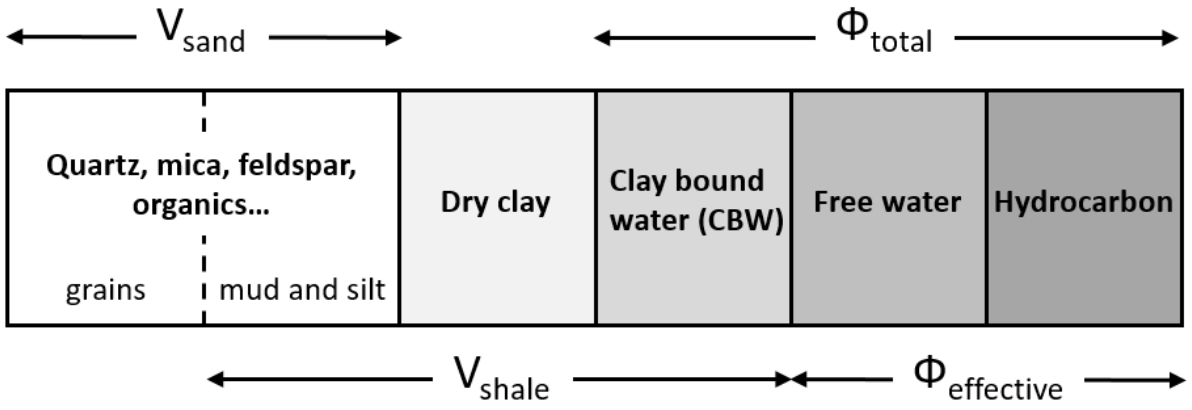

Figure 5.6: *Elements of a shaly sandstone reservoir. The figure shows that shales not only contain clay minerals, but the concept also includes clay bound water and clay-sized particles of quartz, mica, feldspar and others. Clay bound water is the difference between total porosity and effective porosity. It has been assumed that the volume of each element is equal for simplification only. Figure modified from (Al-Ruwaili and Al-Waheed, 2004).*

Clay minerals are characterized by their platy nature and their ability to adsorb cations to their negatively charges exposed surfaces. The clay properties affect all well logs and the presence of clay is therefore discussed throughout Section 5.4. The minerals are for example often radioactive and associated with increased gamma ray counts. Hydrogen is contained within all clay minerals, affecting (increasing) the neutron porosity response. Increased porosity can therefore be mistaken by the presence of clay. The density log is also affected by the presence of clay because different clay minerals exhibit different densities than for example quartz.

Shale Volume Quantification

The most frequently used deterministic method within petrophysics for estimating the bulk volume fraction of shale in a formation is based on the total gamma ray log. The equation for the gamma ray index, I_{GR}, is given by

$$I_{GR} = \frac{GR_{log} - GR_{clean}}{GR_{sh} - GR_{clean}} \tag{5.2}$$

where GR_{log} denotes the gamma ray reading of the given depth position, GR_{clean} is the gamma ray log reading from a sandstone or carbonate formation with no shale content and GR_{sh} is the gamma ray log reading in 100% shale. It has been estimated that the volume of shale, V_{sh} equals the gamma ray index I_{GR}, as this relation can be used for the first order approximation of shale volume. It was assumed that the clay minerals in the reservoir are the same as the clay minerals at the depth of the GR_{sh}-value. (Ellis and Singer, 2007; Szabó, 2011)

If the gamma ray measurements are associated with radioactive minerals other than shale, using the total gamma ray log for shale estimation can therefore overestimate the shale content. The spectral gamma ray logs can be utilized for sand and carbonate deposits influenced by sediments or minerals with high thorium, potassium or uranium content. If the potassium curve gives values not associated with shale, the thorium log can be used in Equation 5.2 instead of the total gamma ray log. Equally, the potassium and uranium logs can be used in combination with the same equation. (Glover, nd)

Clay Volume Quantification

Elemental analysis is necessary for quantifying the volume of clay. The weight percent of clay, W_{cl} has been estimated from the elemental capture spectroscopy measurements by combining weight percentages of the elements silicon, calcium, iron and magnesium. This weight percent of clay is a function of the matrix and has been converted to a fraction of the bulk volume by

$$V_{cl} = W_{cl} \times \frac{\rho_{ma}}{\rho_{cl}} \times (1 - \phi_t) \tag{5.3}$$

where ρ_{ma} is the composite density of all solids, ρ_{cl} is the density of the clay minerals and ϕ_t is the total porosity. Calculation of the total porosity is described in Section 5.4.5. This method is uncomplicated and objective, but it is based on correlations that are not always applicable. Also, the equation does not distinguish between different types of clay. For more information, see Ellis and Singer (2007).

5.4.4 Fluid Identification

Fluid types have been identified from fluid samples acquired at different logging depths. Well logs have also been important as these provide continuous measurements from the wellbore.

Water, oil and gas are fluids expected to be encountered in the subsurface and one challenge is to distinguish the associated well log responses from each other. Crossover between the neutron and the density curves is indicative of light oil or gas (Ellis and Singer, 2007). When gas is introduced into the formation, the bulk density is expected to decrease as the density of gas is lower than the density of water. The neutron porosity log is sensitive to hydrogen concentration and as the hydrogen concentration in gas is lower than that in water, the neutron porosity decreases when gas substitutes water. The neutron-density crossover is usually less pronounced for oil. Resistivity measurements have also been important for fluid identification as the bulk resistivity is largely determined by the pore fluid resistivity. High resistivities can be caused by the presence of oil or gas. Water is a conductive material exhibiting low resistivities compared to hydrocarbons. Figure 5.7 illustrates a classical textbook example presenting a gas-saturated formation where the resistivity measurements start increasing and separating at the same depth as the decrease in gamma ray and the neutron-density crossover. This is interpreted as the depth of the top reservoir. When the volume of clay and consequently the gamma ray log readings increase in the lower part of the gas zone, the neutron-density crossover is less pronounced. Hydrogen is a prominent member of all clay minerals proven by increased neutron responses towards the base of the gas zone. Clay often substitutes the fluid present, giving a higher bulk density compared to a clean formation. This clay effect can be falsely interpreted as increasing gas saturations or presence of oil. Information on clay mineral distribution is necessary for determining whether the clay minerals substitute the fluid or the grains or a combination of these.

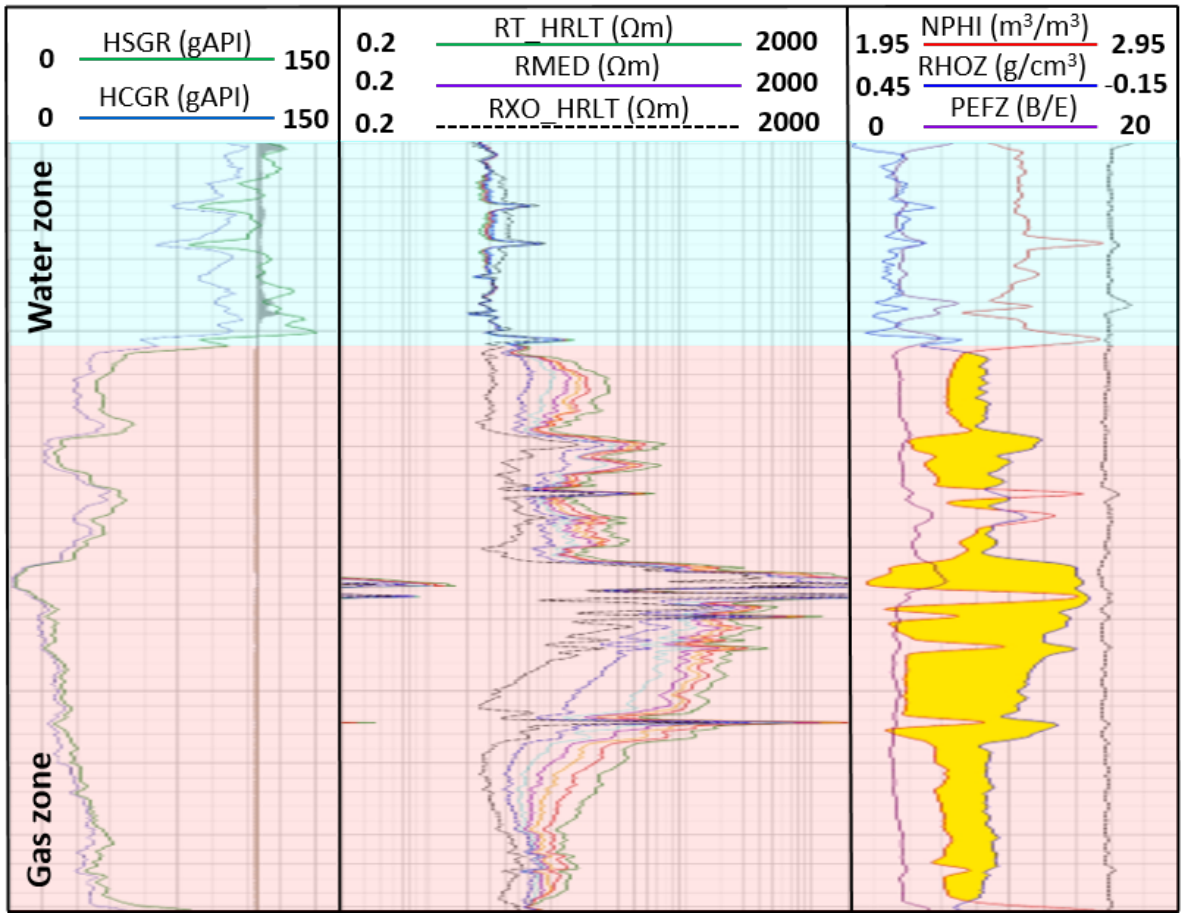

Figure 5.7: *Fluid identification from well 7220/8-1 (Skrugard) in the Barents Sea. The water zone, i.e. the overburden (blue), is characterized by low resistivities and high neutron, density and gamma ray log readings. The gas zone (red) is characterized by high resistivities relative to the water zone, crossover between the neutron and density curves (yellow) and low gamma ray log readings. A likely cause of the increased gamma ray log in the lower part of the gas zone is the introduction of clay minerals to the formation. The neutron-density separation decreases when clay is introduced to the formation. Notice that the neutron and density curves are on sandstone scale. Only the most relevant curves for this project have been labeled. The figure is modified from the composite log available in the DISCOS database.*

5.4.5 Porosity Estimation

Porosity calculation has been important for estimation of hydrocarbon potential. Total porosity ϕ_t and effective porosity ϕ_e logs have been calculated and used as input to different water saturation equations. The difference between the total and effective porosity is the clay bound water (CBW) which is illustrated in Figure 5.6. The total porosity equals the effective porosity for clean formations.

Total Porosity

The total porosity has been estimated from the density measurements because of the well established linear relation between density and porosity and because only a few parameters are required (Ellis, 2003). The formation bulk density ρ_b can be calculated from the fluid density ρ_f, matrix density ρ_{ma} and the total density porosity ϕ_t and the equation is given by

$$\rho_b \;=\; \rho_f \times \phi_t \;+\; \rho_{ma} \times (1 - \phi_t) \tag{5.4}$$

Solving the equation for total porosity gives

$$\phi_t \;=\; \frac{\rho_{ma} \;-\; \rho_b}{\rho_{ma} \;-\; \rho_f} \tag{5.5}$$

where ρ_b is the quantity measured by the density log. The equation has been calculated for each formation/fluid zone as both the matrix and fluid density changes with depth. The rock matrix density measured from core samples have been used. For the zones with no core data, average grain densities of core plugs from zones with similar log responses have been used. Typical matrix density values are 2.64 - 2.65 for sandstone and 2.71 for limestone (Ellis and Singer, 2007). Chart GEN-7 in Figure A.3 has been used to determine the fluid density, i.e. the water density, from known values of temperature, pressure and salinity. These parameters were assumed not to change within the depth range of interest. The temperature and the pressure have been taken from the hydrocarbon zone and found in the fluid sample report. The water salinity has been calculated from chart GEN-6 in Figure A.4. The resistivity of the fluid was then required. The density tool has a high vertical resolution and therefore a shallow depth of investigation. As a consequence, the density tool measures the mud filtrate in the invaded zone, and not the actual formation fluid(s). The salinity has consequently been found for the mud filtrate with resistivity and reservoir temperature given in the fluid sample report. Notice that this approach for calculating the salinity is only valid if the mud is water-based.

The density of the formation water has been assumed to be equal to the mud filtrate density. The density of the mud filtrate is higher than the density of hydrocarbons, especially for gas. Using the mud filtrate density for density porosity calculation in the gas

zone will give too high porosity values. This challenge has been solved by combining the density porosity log with the total porosity from the combinable magnetic resonance tool (TCMR). The TCMR porosity is sensitive to the presence of hydrogen in the formation, giving too low porosity readings in the gas zone. Freedman et al. (1998) has developed the density-magnetic resonance (DMR) method that corrects the total formation porosity in the gas zone. This approach has been used in this project because the density of the gas was unknown. In a gas-bearing zone, the gas-corrected total porosity (DMRP) always lies between the density porosity (DPHI) and the TCMR porosity and can be approximated as

$$\text{DMRP} \cong 0.6 \times \text{DPHI} + 0.4 \times \text{TCMR} \tag{5.6}$$

Porosity can also be evaluated from acoustic logging or from the neutron porosity log. The porosity estimated from the sonic log requires knowledge of the velocity of the matrix and the pore fluid(s). The neutron porosity log measures the true porosity only for water-saturated formations with a hydrogen-free matrix. (Ellis and Singer, 2007)

Effective Porosity

For core analysts, effective porosity is the volume of connected pores. For log analysts, however, the effective porosity describes the pore volume that has the potential to store hydrocarbons. The effective porosity is the total porosity excluding the clay bound water (CBW) which is given by

$$\phi_e = \phi_t - \text{CBW} = \phi_t - V_{sh} \times \phi_{sh,e} \tag{5.7}$$

The effective porosity in clay, $\phi_{sh,e}$, has been estimated from the gas-corrected total porosity log from a 100% shale zone because the effective porosity is assumed to be zero within shale. The volume of shale in the formation has been calculated from the gamma ray log (see Section 5.4.3). (Woodhouse and Warner Jr., 2004; Peeters, 2011)

The total and effective porosity can also be calculated from the neutron-density cross-plot by determining the point corresponding to 100% shale. Using a dry shale point yields the

total porosity and a wet shale point yields the effective porosity. The shale is wet when clay bound water is present. This method is further described in (La Vigne et al., 1994).

5.4.6 Water Saturation Estimation

Water saturation (S_w) estimation requires input of several measured and estimated petrophysical parameters. Multiple equations and approaches have been developed to determine the water saturation of a formation, giving different results (Worthington, 1985; Ellis and Singer, 2007). Uncertainties are minimized by carefully evaluating which method to use.

The interplay between the resistivity of the formation and the water saturation of the uninvaded formation is described by the Archie equation (see Equation 3.1). This equation is based on the total porosity and is applicable only for clean sandstone reservoirs as it is assumed that the formation water is the only conductive medium (Archie, 1942). For calculation of the Archie water saturation, the required true formation resistivity has been assumed equal to the deep resistivity readings and the water resistivity value has been found in the fluid sample report. The lithology coefficient a, cementation exponent m and saturation exponent n are often assigned the values one, two and two respectively for sandstones. The equation assumes that the porosity is mainly intergranular and not caused by fractures. (Doveton, 2001; Ellis and Singer, 2007)

The water saturation estimated from the Archie equation is overestimated when clay minerals are present in the formation as clay adds a conductivity contribution. The consequence is a pessimistic hydrocarbon volume estimation. The water saturation equations accounting for the presence of clay can be divided into two distinct groups, but they all revert to the Archie equation in the limit of no shale content. The first group considers shale as a homogeneous conductive medium and the equations depend on the volumetric fraction of shale in the formation (V_{sh}). These equations are often applied due to their simplicity. The physical basis of these models does not comply with reality, but nevertheless, the equations often provide reasonable results. The second group is linked to the ionic double layer, i.e. linked to the clay bound water observed in shaly sandstones. Special core analysis (SCAL) data is required for such methods. The British mathematician and professor in statistics, George Box, has stated that "All models are wrong, but some are useful", which is descriptive of the water saturation equations for shaly sand-

stone reservoirs. The equations based on the volumetric fraction of shale in the rock are unrealistic and the ionic double layer equations are usually impractical. (Doveton, 2001)

The ionic double layer equations have not been regarded in this project as SCAL data has not been available. The equation based on V_{sh} developed by Leveaux and Poupon (1971), better known as the Indonesia equation, is widely used in the oil industry. The disadvantage of this method is that there are large uncertainties as to whether the porosity input should be effective or total (Woodhouse and Warner Jr., 2004). The modified version of the Simandoux model (Bardon and Pied, 1969) has been used as this model has theoretical basis compared to the Indonesia model (Peeters, 2011). The modified Simandoux model gives better accommodation for the shaliness of the formation than the Simandoux model developed by Simandoux (1963). The equation is given by

$$\frac{\phi_e^m}{a \times R_w \times (1 - V_{sh})} \times S_w^n + \frac{V_{sh}}{R_{sh}} \times S_w - \frac{1}{R_t} = 0 \tag{5.8}$$

where R_{sh} denotes the resistivity log reading in 100% shale and R_w is the water resistivity assumed to be constant in the zones of interest. R_w has been determined from fluid samples from the underburden, i.e. the water-saturated formation(s) below the reservoir. As the effective porosity is required input, it is the effective water saturation that is calculated (Doveton, 2001; Kumar, 2010). From the studies of Peeters (2011), it was however concluded that the model works best for total porosity.

Notice that the water saturation results from the Archie equation and the modified Simandoux equation are not directly comparable as Archie's equation considers the total porosity and the modified Simandoux equation considers the effective porosity.

5.5 3D Unconstrained CSEM Inversion

3D unconstrained inversions have been performed prior to running 3D constrained inversions. The objective with running unconstrained inversions has been to inspect the input data and to test different input parameters to be used for constrained inversion. The CSEM inversion workflow is explained in Section 3.1.5. Two and a half-dimensional (2.5D) unconstrained inversions have been run with the aim to evaluate the data information at different frequencies and to approximately determine the background resistivity

distribution in order to build the start model for 3D unconstrained inversion. Different parameters have been tested and the 3D inversion results have been assessed with the focus of accurately imaging the Pingvin gas discovery. The parameters; cell size, frequency, offset range and regularization strength, have been in focus. Start model and the seabed surface have been required input to the inversion.

5.5.1 Data Quality Control

The quality of the input data has been inspected with the purpose of detecting outliers and unlikely data values in order to prevent inaccurate and noisy inversion results. The processed CSEM data has been controlled by evaluating information from different receivers and at different frequencies, inspecting magnitude and phase curves and by examining 2.5D and early 3D inversion results. Figure 5.8 shows typical responses in terms of electric magnitude and phase for CSEM data with presence of a hydrocarbon reservoir. Increased amplitude and reduced phase gradient is expected for receivers measuring the reservoir response compared to the receiver measuring the background response (Eidesmo et al., 2002c; Røsten et al., 2003).

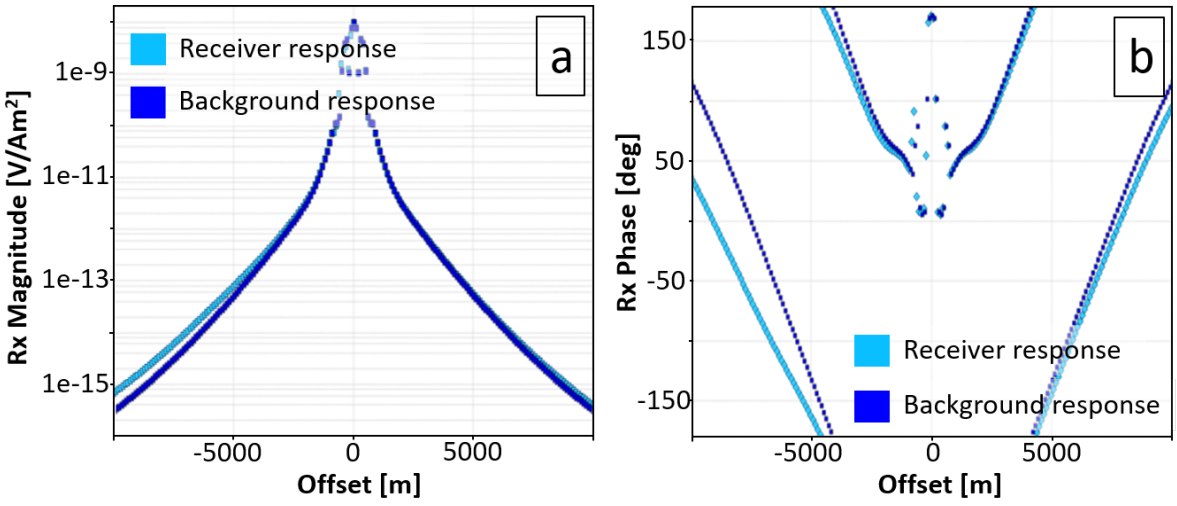

Figure 5.8: *Typical (a) magnitude and (b) phase response for CSEM data with presence of a hydrocarbon reservoir. The light blue curves represent the electric responses from one receiver located at the edge of the reservoir and the darker blue curves represent background values measured by a receiver located far from the reservoir. Increased amplitude and reduced phase gradient is expected for hydrocarbon accumulations. The light blue and the dark blue curves start separating at about 3000 meters source-receiver offset. Figure modified from (Eidesmo et al., 2002c; Johansen et al., 2007).*

5.5.2 Parameter Selection and Testing

Cell Size

Through the 3D inversion, the area of interest has been divided into cells where each cell has been assigned a vertical and a horizontal resistivity value. The cell size has been determined based on a trade-off between spatial resolution and computer computation time (EMGS, ndc). Use of large cells will decrease the spatial resolution and small cells will increase the computational time. In EMGS, the standard horizontal cell size for 3D inversions is 200 meters. The vertical cell size has been determined in the inversion software by minimizing the distance between the receivers and the cells closest to the seabed. This input parameter has not been evaluated through inversion results, but has rather been predetermined.

Frequency

A range of low frequencies is emitted by the electric dipole source. The frequencies with the most pronounced source signals have been selected and different combinations of these have been tested as input for the inversion. Additional information in terms of frequency has been provided from the skin depth curve (see Section 3.1.3) and from 2.5 inversion results. For frequency evaluation in this study, it has been assumed that the depth of investigation is 1.5 times the skin depth. The skin depth and hence the depth of investigation decreases with increasing frequency. It has been important to include high and low frequencies to image the resistivity trends at both shallow and large depths.

Offset Range

Different source-receiver offset ranges have been determined for each frequency selected. The offsets have been cut to remove data with little to no geological information. Data at large offsets with low signal-to-noise ratios has been removed. The electromagnetic field fluctuates close to the dipole source and this near field is dominantly affected by the direct wave (Johansen et al., 2005). Small offsets have consequently been removed because of the difficulty of imaging this near field. As electromagnetic signals are attenuated more for high frequencies, the offset ranges have been selected to be wider for low than for high

frequencies (Mittet and Morten, 2012). Figure 5.9 shows how the offset range has been determined for a specific frequency.

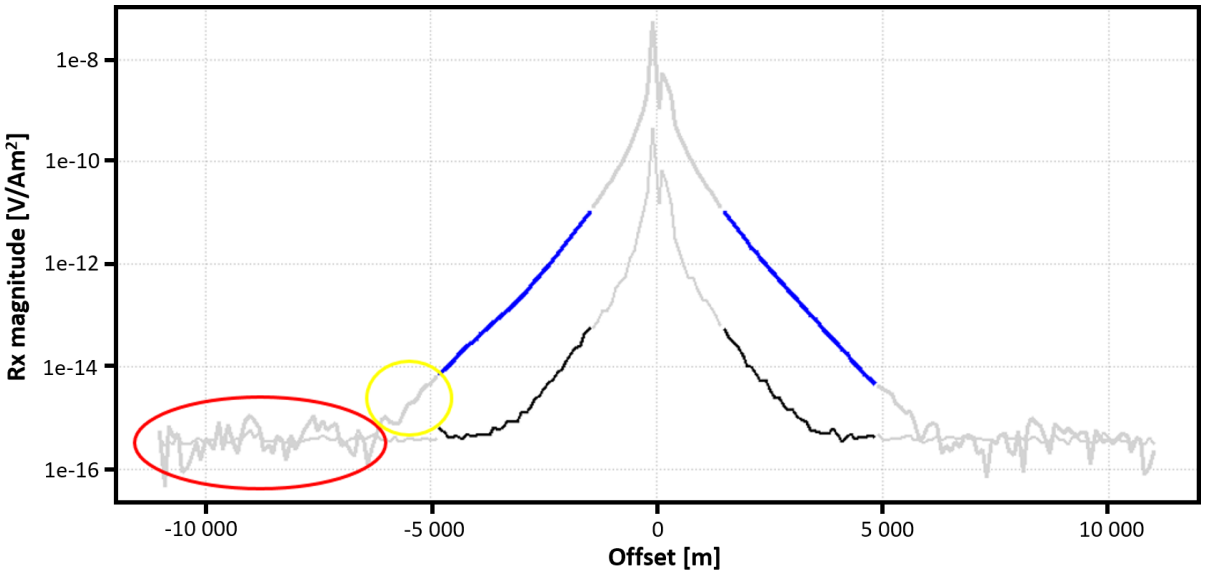

Figure 5.9: *Selected offset range for 10 Hz (blue curve) and associated noise (black curve). The data at large offsets has been masked out in the processing of the data (marked in red) and the offset range selection for the inversion (marked in yellow). The outer offset has in this case been set to 4 900 meters and the minimum offset has been cut at 1 500 meters. The data colored gray has been removed both for negative offsets and positive offsets.*

2.5D Inversion

2.5D inversions have been performed with a simple start model, as the utilized Gauss-Newton method is less sensitive to the input resistivity model than the 3D inversion algorithm (see Section 3.1.5). Resistivity readings from the deep resistivity well measurement have been utilized for building the start model. Masking has been included in the inversion process to combine cells and to decrease the number of unknown parameters in the inversion. The spatial resolution has consequently been reduced as a function of distance from the area of interest. Figure 5.10 illustrates the 2.5D inversion process, from start model trough mask file and to inversion result.

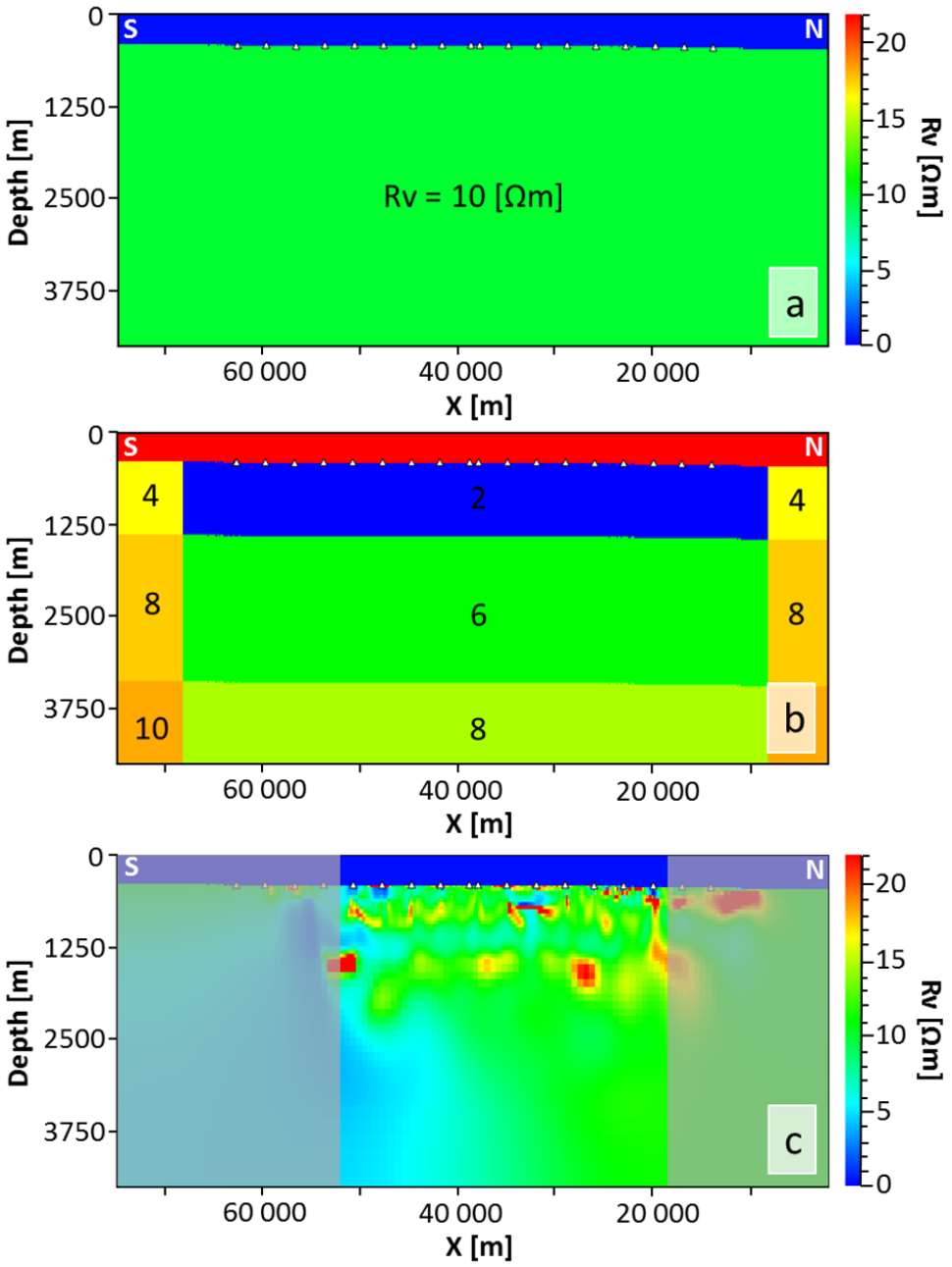

Figure 5.10: *Example of 2.5D (a) start model, (b) mask file and (c) associated inverted resistivity model. This inversion has been run with a halfspace start model with a vertical resistivity of 10 Ωm. A halfspace model denotes a model where constant vertical and horizontal resistivities are allocated to all the cells. The cells have been upscaled through masking by the integers shown in (b). The 2.5D inverted resistivity model is a result of the Gauss-Newton minimization method. The results colored gray should be ignored because of poor data coverage outside the input receivers. Notice that X on the x-axis denotes the source-receiver offset.*

Regularization

Regularization has been applied to limit the number of possible resulting resistivity models and to stabilize the inversion results. The regularization applied has smoothed the model in the vertical and in the horizontal directions, with the smoothing strength dependent on the regularization strength parameters. The model has been smoothed by comparing the resistivity in one cell with the resistivity in the surrounding cells. Application of too low regularization can cause noisy inversion results and too high regularization can cause removal of real geological resistive anomalies from the inversion result. There are different regularization parameters that can be adjusted and different combinations have been tested to obtain the optimal spatial resolution. In this study, the regularization has been set to smooth the resistivity model more in the horizontal directions than in the vertical direction, thus favoring a vertically layered resistivity model. Regularization cooling in the vertical and the horizontal directions has been applied, where the regularization strength has been reduced with increasing iterations (Tveit, 2014). Because of the many regularization parameters possible to adjust, only the regularization cooling has been emphasized when presenting the results.

5.5.3 Start Model Building and Testing

Several 3D vertical and horizontal start models have been built, based on resistivity well logging measurements and 2.5D inversion results. In order to obtain an inversion result that reflects the true subsurface resistivities, the resistivities included in the start model should be close to the actual background resistivities in the subsurface. For all the start models created and tested, a horizontal surface has been inserted right below the seabed to account for different seabed depths in different positions. This volume between the seabed and the horizontal surface has been assigned constant vertical and horizontal resistivity values to ensure equal resistivity values right below the seabed for the entire model. The start models have not been built with any lateral changes in resistivity. The seawater conductivity has been used as input to the start model, which has been generated using source measurements. Inversions concentrate on updating areas with large resistivity contrasts. The upper part of the vertical and horizontal start models, influenced by sea water, has therefore been smoothed to reduce the resistivity contrast between the seawater

and the formation. Figure 5.11 shows an example of a halfspace and a gradient-based vertical start model.

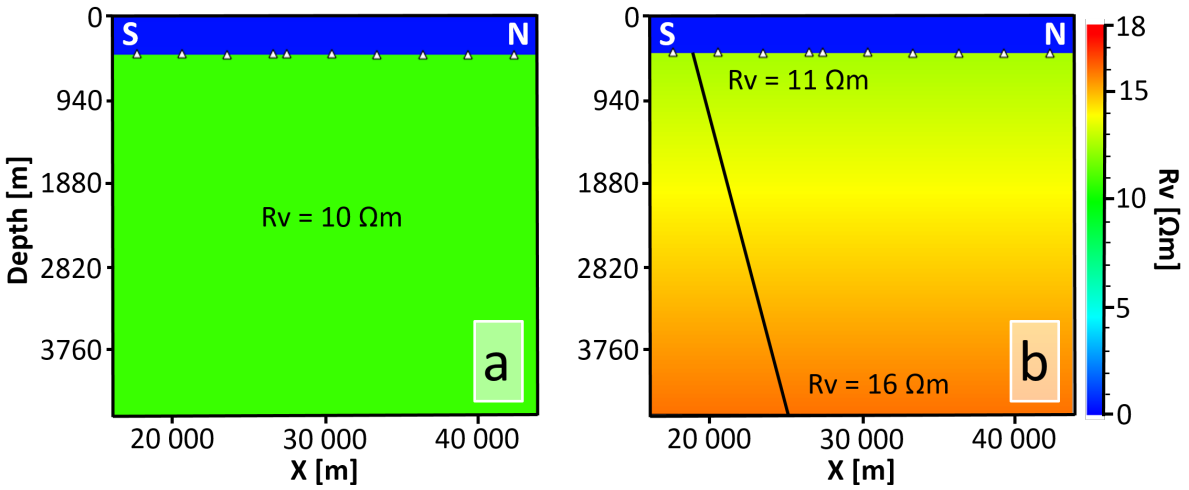

Figure 5.11: *3D vertical (a) halfspace and (b) gradient-based resistivity start model along one receiver line. The halfspace model has been built with a constant resistivity value of 10 Ωm and the gradient-based model has been built with resistivities increasing from 11 Ωm at the seabed to 16 Ωm at 4500 meters depth.*

5.5.4 Unconstrained Inversion Results

The first few inversions have been run with different start models, i.e. with different halfspace and gradient models. Some inversion jobs have been dedicated to frequency testing, but regularization strength was mainly in focus for the unconstrained inversions. The bathymetry file has been input to the inversion which is usually created from source depth measurements. It is, however, the receiver depth measurements that have been used to create the seabed surface because of problems with the source depth measurements for survey BSTEN05.

Figure 5.12 shows an example of the vertical and horizontal models obtained from 3D unconstrained inversion, illustrating how a thin horizontal hydrocarbon-filled layer can be imaged. The high resistive anomaly associated with the hydrocarbon reservoir is present in the vertical, but not in the horizontal resistivity model, as electromagnetic energy is guided through thin horizontal hydrocarbon-filled reservoirs. As described in Section 3.1.2, inline data and hence the vertical resistivity component can detect thin high

resistive layers, whereas the broadside data and hence the horizontal component measures the background trends.

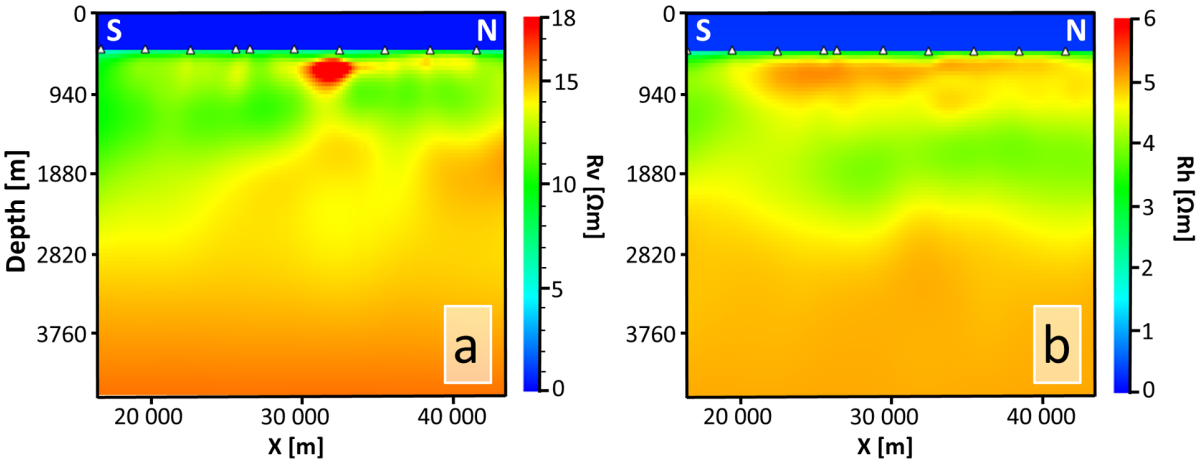

Figure 5.12: *3D unconstrained inversion example. The shallow thin horizontal hydrocarbon-filled reservoir has been detected by (a) the vertical, but not (b) the horizontal resistivity model. See text for more information.*

5.6 3D Constrained CSEM Inversion

3D constrained CSEM inversions have been performed to limit the solution space and focus the electromagnetic energy at the reservoir level. Notice that constraints only can be applied when accurate knowledge on the geology is available. In this study, the top reservoir has been interpreted from the 2D seismic data, depth converted by using the top reservoir in the well as a reference and used as constraint for the inversion. Information from seismic and petrophysical data has thus been incorporated in the CSEM inversion. The high resistive anomaly associated with the hydrocarbon-filled reservoir has been forced below the top reservoir surface. As the Pingvin reservoir has been in focus, data from fewer receivers have been used for running constrained inversion than for unconstrained inversion (see Figures 4.3 and 4.4). By using data from fewer receivers, it was believed that the constrained inversion would focus more on updating the Pingvin anomaly than focusing on the distal background values. It was also believed that the total data misfit would be lowered compared with the unconstrained inversion results. Recalling the concept of anomalous transverse resistance (see Section 3.1.6), it is expected that the resistivity of high resistive anomalies associated with hydrocarbon reservoirs will increase

when the thickness is decreased, e.g. when the electromagnetic energy is concentrated within a specific area. More correct positioning, thickness, lateral extent and resistivity strength were believed to be obtained for the target when constraining the inversion. The paper written by Bhuiyan et al. (2015) shows that the performed seismically guided inversion significantly improved the lateral and the vertical resolution of the high resistive anomalies from the unconstrained inversion at the Albatross and Snøhvit areas in the Barents Sea.

Constraining the inversion can be performed in different ways. For this project, the 3D start model has in combination with an a priori resistivity model, weight grid model, the depth converted top reservoir surface and the measured CSEM data been used to produce the constrained inversion results. The objective of running inversions is to update the resistivity model by minimizing the total cost function. Tikhonov regularization has been implemented for the minimization of the weighted sum of regularization misfit. The regularization misfit can be expressed as

$$\varepsilon_{reg} = \sum_{ix,iy,iz} W(ix,iy,iz) \times \Big[m(ix,iy,iz) - m^{apriori}(ix,iy,iz) \Big]^{L} \tag{5.9}$$

where W is the weight grid model, m is the inverted resistivity model, $m^{apriori}$ is the a priori model and L is the regularization norm (EMGS, ndb; Zhdanov et al., 2007; Constable et al., 2015). The models m and $m^{apriori}$ have been chosen to be the inverse of the conductivity model, which is the same as the resistivity model. For each iteration, the resistivity of every cell in the inverted resistivity model has been compared with the resistivity from the same cell in the a priori model and multiplied with the value of the cell in the weight grid model. The sum of the contributions from all the cells is termed the regularization misfit. A penalty was introduced when the parameter m deviated from the created a priori model $m^{apriori}$. Most deterministic methods require some penalty to be applied to the model in order to deal with instabilities and non-uniqueness. The Tikhonov regularization, in which the model penalty and total cost function are minimized, has therefore been applied to run constrained inversion. This regularization algorithm is frequently used for inversion of different types of geophysical problems. (Constable et al., 2015) The input a priori model has been chosen to be the same as the 3D start model for constrained inversion because no better estimate of the background resistivities has been available.

The regularization norm L has been given the value two, leaving the regularization misfit as a quadratic function. In contrast to L=1, L=2 gives a more smooth resistivity model because small changes in resistivity between the inversion result and the same cell in the a priori model have been favored. The set-up favors creation of conductive anomalies instead of high resistive anomalies because conductive anomalies usually exhibit lower resistivity contrasts with the background values than what high resistive anomalies do. Figure 5.13 shows the regularization misfit function for one iteration and one single cell for L=1 and L=2. For each cell, the penalty of updating large resistivity changes is larger for L=2 than for L=1.

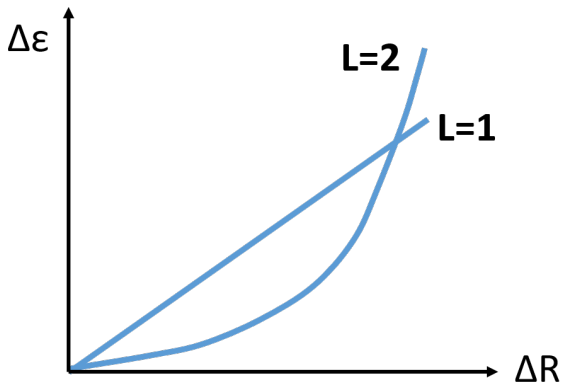

Figure 5.13: *Regularization misfit for one iteration and for one single cell as a function of regularization norm L. ΔR is the difference in resistivity between the inversion result and the a priori model. L=1 gives a linear trend between the regularization misfit and the resistivity change between the inversion result and the a priori model for the same cell. L=2 favors small resistivity updates, while for L=1, the inversion is penalized less for placing high resistive anomalies in the inverted model.*

5.6.1 Start Model Evaluation and Building

It has been very important that the start model represents the true subsurface resistivities; the more accurate the start model, the more precise recovery and positioning of the resistivity anomalies in the subsurface (EMGS, ndc). The accuracy of the start model has been especially important for constrained inversion as the start model also has been used as the a priori model. The start model used for the unconstrained inversion has been evaluated and compared with the background resistivity trends from the final unconstrained inversion result in order to create an improved start model for constrained inversion.

Average resistivity maps have been created every 500 meters, starting from the seabed, both for the unconstrained inversion result and for the associated start model. The resistivity contents from the average resistivity maps from these two models have been compared in histogram windows within the same intervals. A new start model to be used for the constrained inversion has been created, with the same background resistivity trends as those obtained from the unconstrained inversion result. Figure 5.14 illustrates comparison between averaged resistivities from unconstrained inversion result and from the associated start model for a given depth interval.

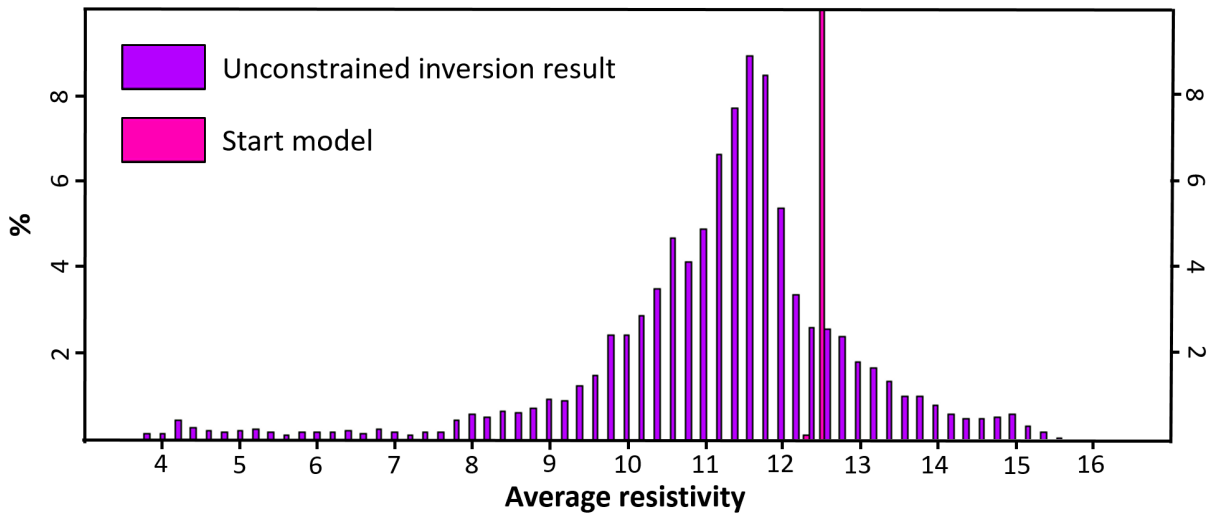

Figure 5.14: *Example of comparison between resistivity content from average resistivity maps created for an interval of 500 meters from unconstrained inversion result and from the associated start model. The histogram shows resistivity values for a given depth interval. The resistivity content from the inversion result shows a large contribution of resistivity around 11.5 Ωm and the start model to be used for constrained inversion should therefore be built with approximately this same value in that depth interval.*

As for the 3D start model used for unconstrained inversions, a horizontal surface has been inserted below the seabed and this volume between the seabed and the surface has been assigned constant vertical and horizontal resistivity values. Horizontal surfaces have also been inserted into the model at depths where the resistivity values or trends change. Seabed smoothing has been applied, however less than that applied to the start model for unconstrained inversion. The water conductivity measured from the acquisition vessel has been input to the start model.

5.6.2 Weight Grid Model Building

The aim has been for the constrained inversion to update the Pingvin anomaly with accurate positioning, thickness, lateral extent and resistivities, with less focus on updating the background resistivities. This requirement has been complied by creating a weight grid model, assigning different regularization weights to different parts of the model. Figure 5.15 illustrates an example of the type of weight grid model created for constrained inversion.

The depth converted top reservoir surface interpreted from the 2D seismic data has been used as input to the weight grid model. The top reservoir has been copied and assigned depth values two cell sizes deeper than the top reservoir surface. This surface has been termed the base reservoir. Two cells have been chosen because this vertical distance corresponds to a reasonable reservoir thickness. One cell was not chosen as the distance between the top and the base reservoir, as this would not allow the electromagnetic waves to be guided through the high resistive layer without being interrupted at cell corners. The surfaces needed to be equally laterally extended as the weight grid model and the surfaces have therefore been gridded. The area between the top reservoir and the base reservoir has been given the value of zero in the weight grid model. In practice, this means that the inversion has been allowed to update freely within this area, with no regularization penalty. The background has been given a slightly higher value, penalizing the total cost function if the inversion would update the resistivity within each cell different from the resistivity in the same cell in the a priori model. Different weight grid models with different regularization weight in the background have been created, tested and evaluated based on the misfit function and based on noise in the inverted resistivity models. The sea water did not need to be accounted for in the weight grid model. The bathymetry has been input to the constrained inversion and, as a default, no changes in resistivity has been allowed within the sea water.

5.6.3 Selection of Input Parameters

Knowledge on suitable input parameters obtained from unconstrained inversion has been useful for running constrained inversion. As testing of the input parameters; frequency, cell size and offset range has been in focus for unconstrained inversion, testing of these

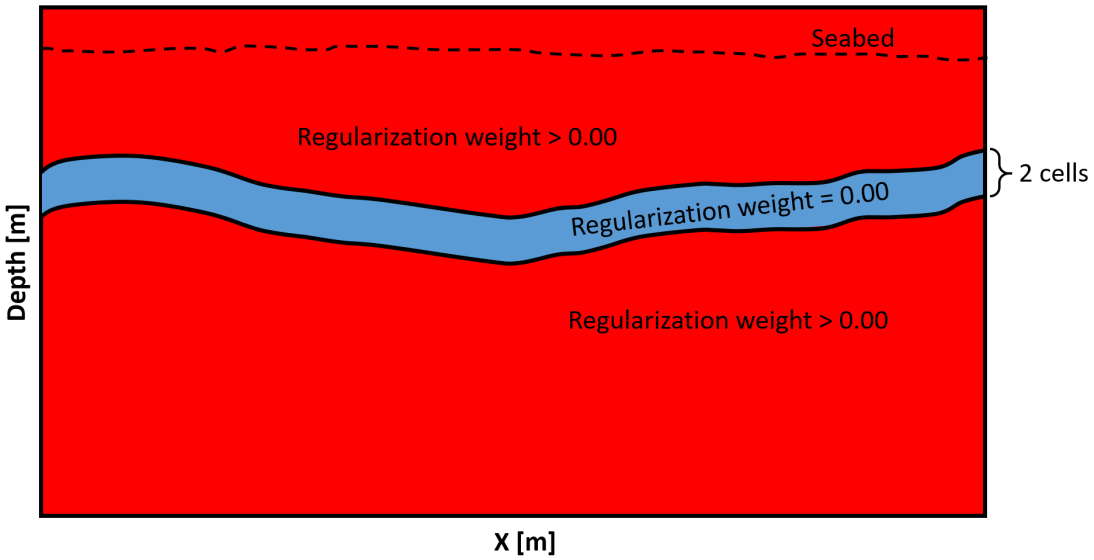

Figure 5.15: *Example of the type of regularization weight grid applied for constrained inversion. No regularization weight has been applied between the top reservoir interpreted from 2D seismic data and the base reservoir (blue). The base reservoir surface has the same shape as the top reservoir, however shifted two cells deeper. The regularization misfit has been penalized if resistivity changes have been made in the background areas (red), as the regularization weight in these areas were given a regularization weight higher than zero.*

parameters has not been emphasized for constrained inversion. The constrained inversion results have been used for quantitative interpretation and obtaining a resistivity model with high vertical resolution has been necessary. The vertical cell size has consequently been decreased compared to the cell size for the unconstrained inversion. The same frequencies have been used. The Pingvin gas discovery has been classified as a shallow target and the offset ranges associated with the lowest frequencies have been decreased compared to unconstrained inversion to decrease the computational time (Bhuiyan et al., 2010).

Constrained inversions have been run with different regularization weight grid models in order to find the regularization weight grid model contributing to accurately imaging the hydrocarbon-filled reservoir. As opposed to unconstrained inversion, smoothing regularization has not been applied.

5.6.4 Constrained Inversion Results

To repeat, the constrained inversion results have mainly been dependent on the measured CSEM data, start model, a priori model and weight grid model, in addition to the input parameters described in the previous section. The results were especially dependent on the a priori model as the inversion aimed to replicate the background resistivities from this model.

Figure 5.16 shows an example of the vertical and horizontal models obtained from 3D constrained inversion and illustrates how a thin horizontal hydrocarbon-filled layer can be imaged. The high resistive anomaly associated with the hydrocarbon reservoir has been detected by the vertical, but not the horizontal resistivity component. Compared with unconstrained inversion, the electromagnetic energy associated with the high resistive anomaly has been focused at the reservoir level.

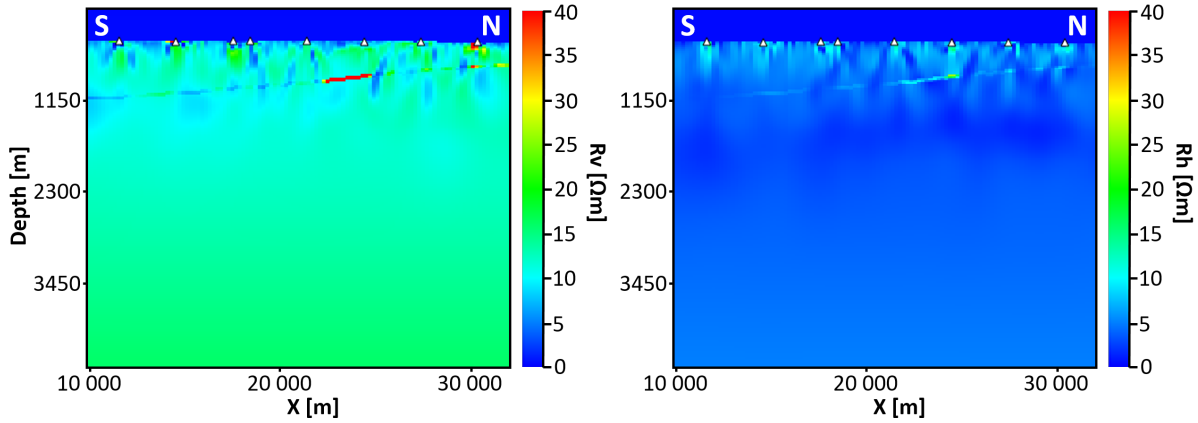

Figure 5.16: *3D constrained inversion example. The shallow and thin horizontal hydrocarbon-filled reservoir has been detected by (a) the vertical, but not (b) the horizontal resistivity model. A slight increase in the horizontal resistivity model is however seen at the location of the reservoir. These inversion results have been obtained by applying constraints through a weight grid model. The anomaly has been forced into the area between the seismically derived top reservoir surface and the base reservoir surface with a constant thickness equal to two times the vertical cell size between them.*

5.7 Color Scale for CSEM Inversion Results

Color scale can have large effects on the inversion results. Proper evaluation of the resistivity content for each resistivity model has therefore been necessary. Color scale has mainly been adjusted based on histograms showing the resistivity content of the model. It has been assumed that the main parts of the total resistivity content from the histograms are associated with the background resistivity values (Barker and Baltar, 2016). For optimal color scale, there should be a clear boundary between the resistivities in the background and the resistivity values associated with the hydrocarbon anomaly. Figure 5.17 illustrates how the inversion results can be affected by the selection of color scale.

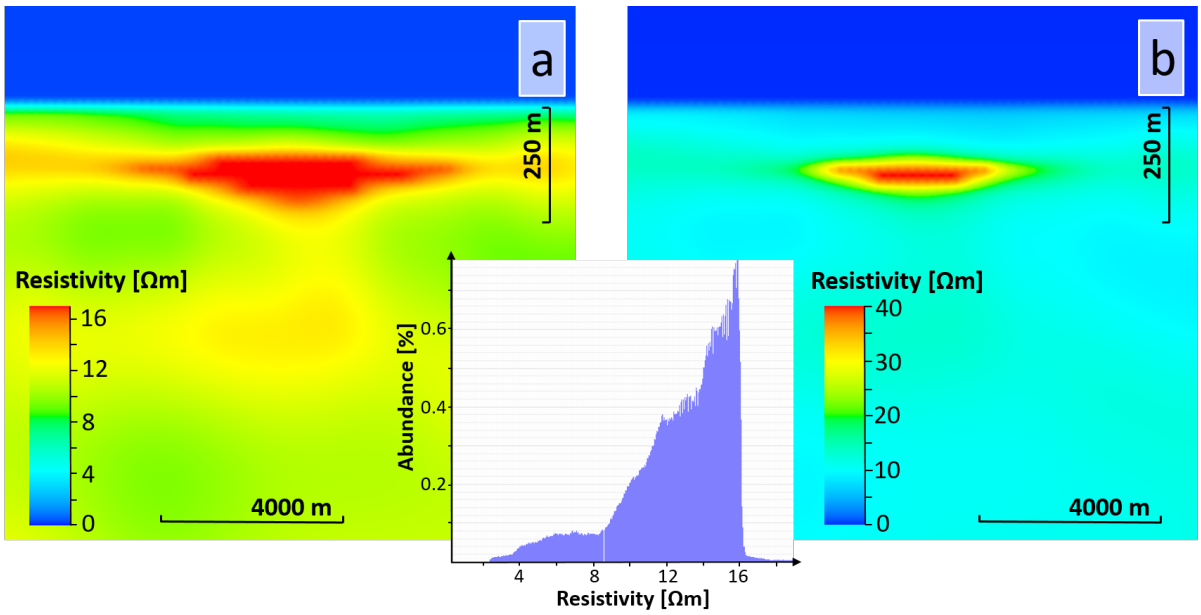

Figure 5.17: *Example of how inversion results can be affected by different color scales. The vertical model presented is a result of unconstrained inversion. The histogram shows vertical background resistivities up to about 16.5 Ωm and one possible color scale for this resistivity model is shown in (a). The color scale has been designed ranging from 0 to 16.5 Ωm, assuming that these resistivities belong to the background response. Resistivities over 16.5 Ωm (bright red) are associated with the high resistive anomaly. A random color scale has been chosen in (b).*

5.8 Uncertainty Evaluation of the CSEM Inversion Results

The performance of the 3D unconstrained and constrained inversions have mainly been evaluated based on the data misfit and through visual inspection of the vertical and horizontal resistivity models. The presence of artifacts in the resulting models and the spatial resolution have been evaluated. Data misfit is defined as the absolute difference between the measured data E_{obs} and the generated synthetic data E_{synth} normalized by the data uncertainty and noise (Constable et al., 1987; Zach and Frenkel, 2009; Maaø and Nguyen, 2010). This relation is expressed as

$$\varepsilon_{data} = \frac{|E_{obs} - E_{synth}|^2}{|\Delta E_{obs}|^2} = \frac{|E_{obs} - E_{synth}|^2}{\alpha^2 |E_{obs}|^2 + |\eta|^2} \tag{5.10}$$

The uncertainty $|\Delta E_{obs}|^2$ is divided into data uncertainty $\alpha^2|E_{obs}|^2$, and noise $|\eta|^2$. Ideally, the data misfit converges with increasing number of iterations and towards the value of one. This means that the inversion results explain the measured CSEM data within the data uncertainty. A high data misfit reflects inaccurate start model or input parameters or noisy input data. Application of too strong regularization can for example cause high data misfit values as the inversion is not allowed to properly reconstruct the measured data. A data misfit lower than one indicate imprecise estimation of the data uncertainty factor α, which typically is associated with acquisition parameters. α is required input to the inversion. A visual consequence can be more noisy inversion results because the synthetic data tries to fit the measured noise. (Zach and Frenkel, 2009) The data misfit can also be expressed in percentage by multiplying the misfit with the data uncertainty factor. For optimal reconstruction of the subsurface resistivities, the data misfit should be close to the data uncertainty factor.

5.9 Quantitative Integrated Interpretation

Quantitative interpretation has involved combining the CSEM constrained inversion results with petrophysical analysis in order to quantify the gross pay and say something

about the reservoir quality. The reservoir has therefore been in focus. Gross pay represents the thickness of the gas-saturated reservoir rock. Gross pay maps have been created by combining an anomalous transverse resistance (ATR) map with established relationships between ATR and gross pay based on rock physics modeling. The reservoir quality has been evaluated by comparing gross pay maps representing different reservoir qualities with the reservoir thickness interpreted from seismic data along a chosen 2D line. The reservoir quality at the well location has been used as a reference for interpretation of reservoir quality within the seismically derived prospect outline. Figure 5.18 shows the workflow of the method.

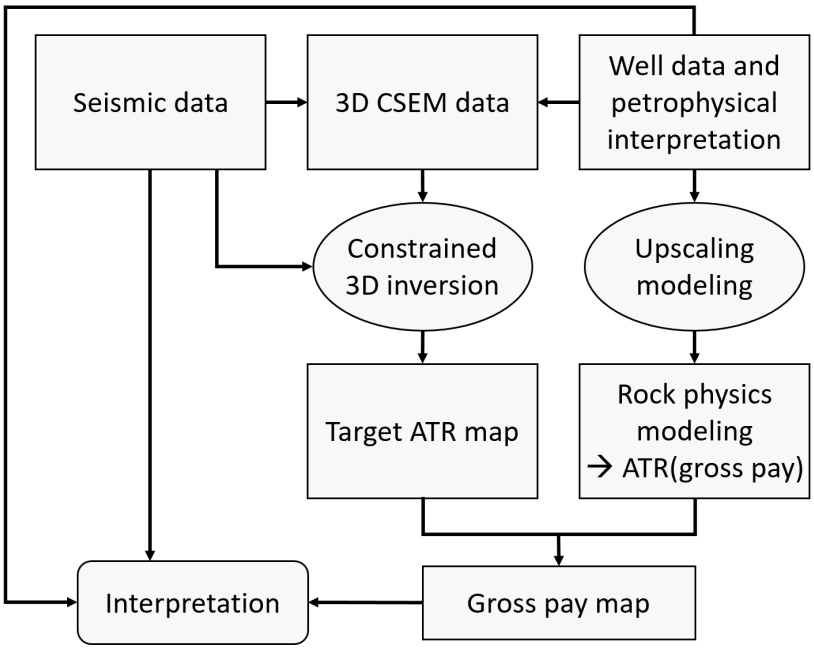

Figure 5.18: *Flow chart explaining the workflow for quantitative interpretation. An anomalous transverse resistance (ATR) map is created based on constrained 3D CSEM inversion results and combined with rock physics models created based on upscaled well data. Relationships between ATR and gross pay are established from the rock physics modeling and used to convert the ATR map to gross pay maps. These thickness maps, representing different reservoir qualities, are compared with results from seismic and petrophysical interpretation for evaluation of reservoir quality. See text for more thorough explanation.*

5.9.1 Anomalous Transverse Resistance Maps

As described in Section 3.1.6, anomalous transverse resistance (ATR) is a property determining the CSEM response, dependent on the difference in resistivity between the target

and the background and the thickness of the target. An ATR map has been created from the constrained inversion results by utilizing Equation 3.3. It is the vertical inversion result that has been used because it is the vertical resistivity component that is sensitive to thin horizontal hydrocarbon-filled layers. First, an average resistivity map has been created by averaging the resistivities within the reservoir layer, i.e. between the top and the base reservoir surfaces used to create the weight grid model. The constant background resistivity value to be used for ATR calculation has been chosen by inspecting the vertical resistivity model in the area surrounding the target. The thickness of the target was set to two cell sizes, which is the distance between the top and base reservoir surfaces. Cells with ATR values less than zero have been set to zero ATR. Figures 5.19 and 5.20 show example of average resistivity map and ATR map respectively.

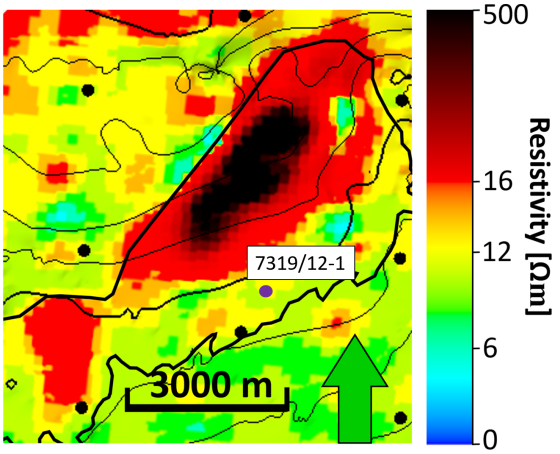

Figure 5.19: *Average resistivity map for the reservoir layer, with high resistivities presented in red to black. The map has been created from the vertical resistivity model from 3D constrained inversion. The black circles represent location of the CSEM receivers. Notice that the cells within the resistivity model are visible.*

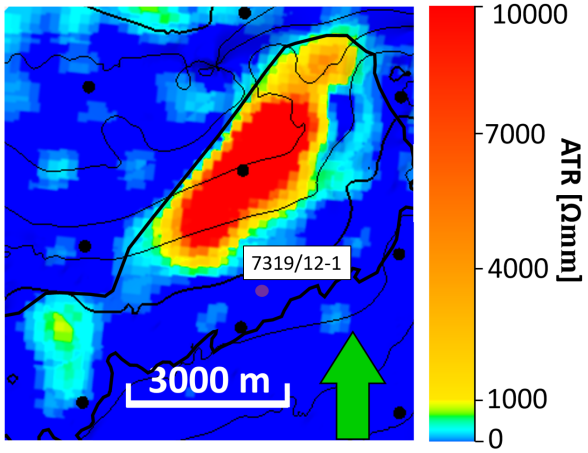

Figure 5.20: *Anomalous transverse resistance (ATR) map of the same target as in the average resistivity map in Figure 5.19. The map has been created by using Equation 3.3, the average resistivity map, a background resistivity of 12 Ωm and a reservoir thickness of 46 meters, i.e. two cell sizes. The black circles represent location of the CSEM receivers. Notice that the cells within the resistivity model are visible.*

5.9.2 Upscaling of Well Data

As CSEM is a low-resolution technique, conductivity variations on a scale similar to well log measurements can not be resolved, hence the need for upscaling of well data. What

is expected from the CSEM data is to measure the bulk resistivity of a rock cube with dimensions in the order of several meters. The bulk resistivity is however determined by the layering of the cube. The horizontal deep resistivity log has been used to calculate the upscaled vertical resistivity (R_v) curve, as it is the vertical resistivity inversion results that have been used to create the ATR map. The upscaling has been done by using moving average, i.e. taking the average of resistivity data points within a six-meter range and assigning the value to the middle data point. The same was done for the other layers. The distance between two data points has been regarded as one layer. The calculation is termed *moving* average because new resistivity values have been accounted for as they become available. The upscaled R_v-curve has been created by stating that resistors in series is the equivalent circuit to a vertical current flow through horizontal bedding, which among others is described by Ellis et al. (2010). The upscaled R_v-curve has been created from

$$R_v^{upscaled} = \frac{1}{L} \sum_i^N R_{v,i} d_i \tag{5.11}$$

where L is the total thickness of N layers, d_i is the thickness of layer i and $R_{v,i}$ is the vertical resistivity of the same layer. L equals six because the average resistivity has been measured every six meters. The horizontal deep resistivity from the well data, $R_{h,i}$, has been used for $R_{v,i}$, as the calculation assumes that each layer is isotropic.

The water saturation estimated from well data has been upscaled by a volume-averaging approach accounting for the effective porosity. The equation is given by

$$S_w^{upscaled} = \frac{1}{\sum_i \phi_{e,i} d_i} \sum_i^N S_{w,i}\, \phi_{e,i}\, d_i \tag{5.12}$$

where $S_{w,i}$, $\phi_{e,i}$ and d_i are the water saturation estimated from the modified Simandoux equation (Equation 5.8), the effective porosity estimated from Equation 5.7 and the thickness of layer i, respectively. It is the effective porosity that has been used and not the total porosity because only the pore volume that can be replaced by hydrocarbons has been considered.

Figure 5.21 shows an example of upscaled vertical resistivity values and upscaled values for water saturation.

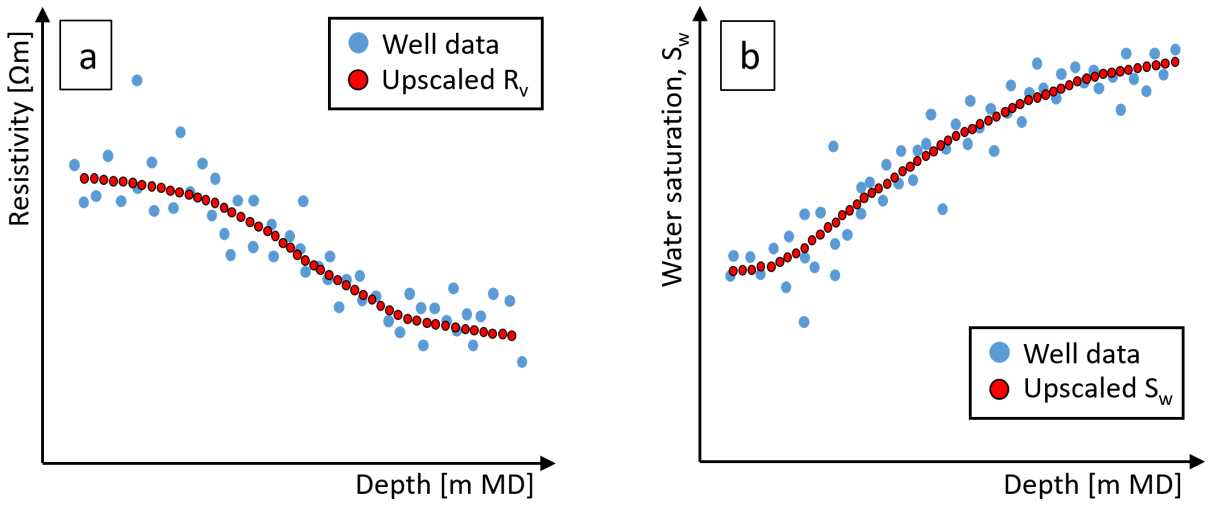

Figure 5.21: *(a) Deep resistivity measurements from well data and the upscaled vertical resistivity (R_v) values as functions of measured depth. The upscaled vertical resistivity values are obtained by using Equation 5.11. (b) Water saturation estimated through petrophysical analysis and upscaled water saturation values as functions of measured depth. The upscaled water saturation values are obtained by using Equation 5.12. The upscaled values show the same trends as the original well data, however with lowered resolution.*

5.9.3 Rock Physics Modeling

Wireline petrophysical measurements and estimations have been utilized for establishing a relationship between ATR and gross pay. Petrophysical data from the sandstone unit only has been used. Non-productive intervals within the sand have been included in the calculations.

Curve Fitting

An empirical relationship between the upscaled R_v and upscaled S_w has been created through curve fitting. The curve shape has been chosen similar to a Simandoux model (Simandoux, 1963) which is given by

$$\frac{1}{R_v} = a\, S_w^{-b} + c \tag{5.13}$$

The curve has been fitted to the data points by altering the coefficients a, b and c. A typical relationship between resistivity and water saturation is presented in Figure 3.9.

In the case of accessibility of only low hydrocarbon saturations at the well location, a synthetic resistivity data point can be created by using the modified Simandoux equation (Equation 5.8), and a presumed irreducible water saturation to establish a relationship between resistivity and water saturation for high hydrocarbon saturations. This fitted curve has been termed guided extrapolation and is presented in Figure 5.22. It is important that the curve is created for a wide range of saturations, as the water saturation might change within the reservoir away from the wellbore.

In addition, a relationship between vertical resistivity and water saturation has been established based on the Archie equation (see Equation 3.1), without consideration of the well data as completely clean formations are rare. This Archie relationship represents a clean reservoir rock.

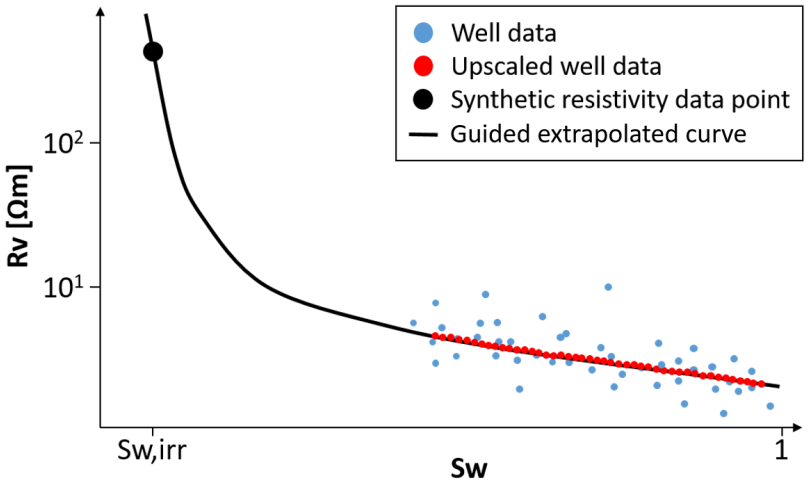

Figure 5.22: *Curve fitting. For this example, the well has not encountered low water saturations. As a consequence, a synthetic data point is constructed for the presumed irreducible water saturation (Sw,irr) by using the modified Simandoux equation (see Equation 5.8). The resistivity and water saturation obtained from well data are upscaled to be comparable with the CSEM data resolution. The guided extrapolated curve is created by using Equation 5.13 and is fitted to the upscaled well data points and the synthetic data point at* $S_{w,irr}$.

Relationship Between Water Saturation and Gross Pay

The water saturation within a reservoir is dependent on the height above free water level (FWL) which is the depth at which the hydrocarbon-water capillary pressure is zero. The relationship between the water saturation and the height above FWL, h, has among others been described by Skelt (1995) (see also (Harrison and Jing, 2001)). A simplified

version of the Skelt saturation-height relationship has been used in this project and is given by

$$S_w(z) \;=\; (1 - Sw, irr)\; exp\Big(\frac{-z}{l}\Big) \;+\; Sw, irr \tag{5.14}$$

where $S_{w,irr}$ is the irreducible water saturation, z is the distance from a chosen reference depth point and l is a scale parameter linked to the radius of the pore throats. Small pore throats require l to be large and large pore throats require a small l. Large pores are often associated with a clean formation. The equation can be applied at all depths, not necessarily within hydrocarbon reservoirs, hence the use of z in the equation instead of h.

Saturations below the hydrocarbon-water contact (HCWC) has not been accounted for and the HCWC has therefore been used instead of the FWL as the reference depth for calculating the water saturation within the reservoir. No resistivity contribution is regardless given by the volume between the HCWC and FWL. Figure 5.23 illustrates how the height above the HCWC changes as a function of water saturation and scale parameter l for a chosen irreducible water saturation. l has been chosen based on the curves presented in this figure and based on the water saturations estimated from the well data within the hydrocarbon zone.

Relationship Between Anomalous Transverse Resistance and Gross Pay

ATR is sensitive to the vertical resistivity which again is sensitive to water saturation which is a function of height above HCWC. The relationship between vertical resistivity and the water saturation and the relationship between water saturation and height above the HCWC are described above. A range of values for height above the HCWC (h) have been assigned ATR values by using the equation given by

$$\mathrm{ATR}(h) \;=\; \int_0^h R_v dz \;-\; R_{bg}h = \int_0^h R_v\Big(S_w(z)\Big)dz \;-\; R_{bg}h \tag{5.15}$$

where R_{bg} is the background resistivity. Equation 3.3 is useful for models with a constant reservoir resistivity. Equation 5.15 is to be used for real reservoirs with changing vertical resistivities with depth (Baltar and Roth, 2013). Tables of ATR values as a function

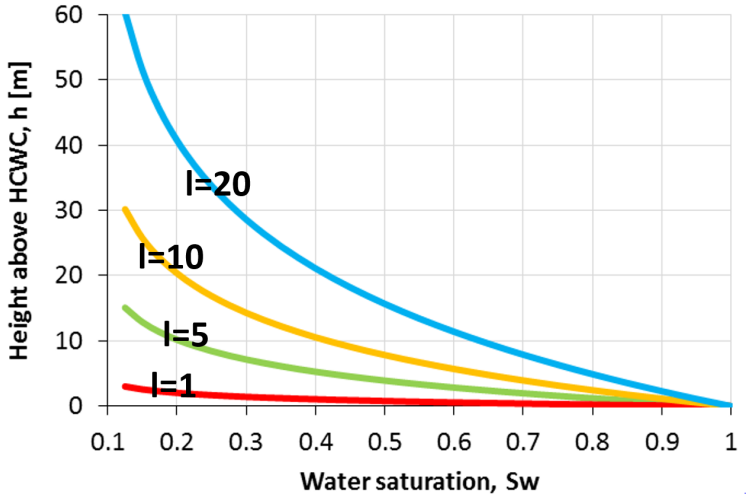

Figure 5.23: *Height above hydrocarbon-water contact (HCWC) as a function of water saturation and scale parameter l. l is linked to the radius of the pore throats; a large l is required for small pore throats. The curves are created by using Equation 5.14 and an irreducible water saturation of 0.08. The figure illustrates that reservoir quality decreases for increasing values of l as the pore throats decrease. Large pores are often associated with clean formations.*

of height above HCWC has been obtained by integrating the vertical resistivity from the reference depth, the HCWC, and to different depth values for the top of the reservoir. One table has been created based on the Simandoux relationship between vertical resistivity and water saturation described by Equation 5.13 and one table has been created based on the same relationship calculated from the Archie equation. 100 meters was set as the maximum gross pay and ATR values associated with higher thicknesses have been given a thickness of 100 meters. Typical relationships between ATR and gross pay are shown in Figure 5.24. For this project, the higher the ATR for a specific gross pay, the better the reservoir quality. Generally, changing ATR with gross pay can for example also be caused by changing pore fluid.

It has been assumed that the base of the reservoir, the base of the sand package, always is below the HCWC to avoid having to account for the level difference between the HCWC and the base of the reservoir (see Figure 5.25). For a reservoir geometry with the base reservoir above the HCWC, the resistivity would have to be integrated from the difference in thickness between the base reservoir and the HCWC in Equation 5.15.

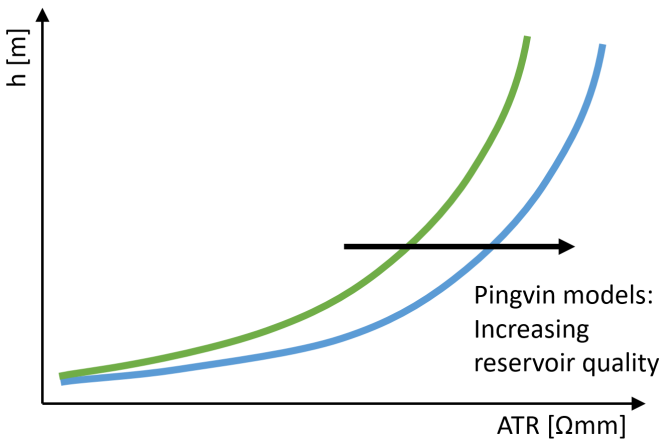

Figure 5.24: *Typical relationships between anomalous transverse resistance (ATR) and height above hydrocarbon-water contact (h). The thickness of the hydrocarbon column increases drastically for high values of ATR. For this project, the blue curve represents a better quality reservoir than the green curve. In general, different curves can represent formations with different pore fluids. The ATR is on logarithmic scale.*

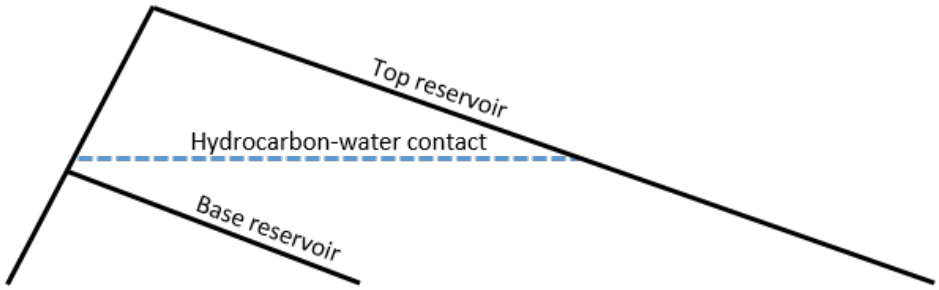

Figure 5.25: *Assumed reservoir geometry. For the calculation of anomalous transverse resistance (ATR) described from Equation 5.15, it was assumed that the base of the reservoir always is below the hydrocarbon-water contact.*

5.9.4 Gross Pay Maps

By the use of the ATR-gross pay tables, each cell in the ATR map created from the CSEM inversion results (see Section 5.9.1) has been assigned gross pay values, i.e. values for height above the HCWC. One gross pay map has been created from the ATR-gross pay relationship based on the Simandoux model and one gross pay map has been created from the ATR-gross pay relationship based on the Archie equation. The Simandoux gross pay map represents the reservoir quality at the well location and the Archie gross pay map represents a clean reservoir. Figure 5.26 shows a reservoir gross pay map associated with the ATR map in Figure 5.20. These maps represent the thickness between the top reservoir and the HCWC.

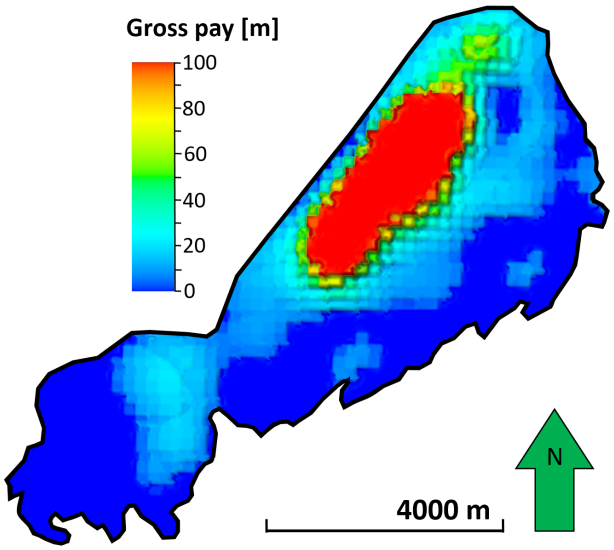

Figure 5.26: *Gross pay map associated with the anomalous transverse resistance (ATR) map presented in Figure 5.20. The map is created from the ATR map obtained from CSEM data and a relationship between ATR and gross pay obtained from rock physics modeling by utilizing petrophysical data. The Simandoux model in Equation 5.13 is used to establish a relationship between vertical resistivity and water saturation for calculation of ATR through Equation 5.15. The gross pay map is bounded by the seismically derived prospect outline.*

5.10 Software

Seismic interpretation, petrophysical analysis and management and inversion of CSEM data have required different geophysical and petrophysical software. Table 5.2 gives an overview of the software used for this project. The E&P software Petrel has been used for interpretation of the 2D seismic data, performance of seismic-well tie, seismic depth conversion and for imaging of seismic and CSEM data. The guided and manual interpretation tools in Petrel have been used for seismic horizon interpretation. 3D resistivity start models and weight grid models have been built in Brickville. It is also possible to use Petrel for model building, but by using Brickville, the workflow is easier and less time-consuming. EMGS' electromagnetic processing, managing and imaging tool, SBLwiz, has been used to perform 2.5D and 3D CSEM inversions. Petrophysical analysis has been performed in Techlog. The codes used to create rock physics models based on petrophysical data and interpretation and to transform an ATR map to gross pay maps have been written in Python.

Table 5.2: *Software used in this project. Petrel has been used for seismic interpretation, performance of seismic-well tie, depth conversion and imaging of seismic and CSEM results. Techlog has been used for petrophysical analysis of data from well 7319/12-1. The EMGS in-house developed programs Brickville and SBLwiz have been used for 3D model building and inversion of CSEM data respectively. The rock physics model building has been performed in Python. In this same program, an ATR map created from the constrained inversion results have been transformed to gross pay maps.*

Data	Software
Seismic interpretation and imaging *Provider: NTNU*	Petrel (Schlumberger, 2016.2)
Petrophysical analysis *Provider: NTNU*	Techlog (Schlumberger, 2016.2)
3D resistivity start model and weight grid model building *Provider: EMGS*	Brickville
Management and inversion of 3D CSEM data *Provider: EMGS*	SBLwiz
Rock physics model building and transformation of ATR map to gross pay maps *Provider: EMGS*	Python

Chapter 6

Results

6.1 Seismic-Well Tie

The available 2D seismic lines from Multiclient Geophysical (MCG), Norsk Hydro (NH) and Norwegian Petroleum Directorate (NPD) have all shown SEG normal polarity. The MCG data was of zero phase and because no other information was given on the type of phase for the NH and NPD data, zero phase was assumed.

The seismic-well tie has been performed as described in Section 5.1. The wavelet has been extracted and estimated from the seismic data itself. The wavelet used was a statistical wavelet as statistical wavelets are regarded as robust (Edgar and van der Baan, 2011; de Macedoa et al., 2016). The match of the reflections at the reservoir depth from the synthetic seismogram and the seismic trace from the closest 2D seismic section, MCG 310, has been regarded as satisfying and no depth shift was therefore applied to the synthetic seismogram (see Figure 6.1). This indicated good quality seismic, check-shot and well data. Figure 6.2 illustrates the seismogram overlain the seismic line MCG 310 crossing the Pingvin discovery. The trough representing the top reservoir identified from well logs matches with the trough believed to represent the top reservoir in the seismic data. The true vertical depth has been assumed equal to the measured depth because of the low maximum inclination of the well.

After time converting the well data, the seabed from the synthetic seismogram did not match the seabed from the seismic data. This was expected because the density log has

been acquired from 936 meters measured depth (MD) and below. As a consequence, the synthetic seismogram was created starting at this same depth. The seismic-well tie has been performed by focusing on the reservoir level. Recall that the top reservoir was encountered by the well at 953 meters MD. As it is the reservoir that has been in focus for this study, the seabed mismatch has therefore not been regarded as an issue.

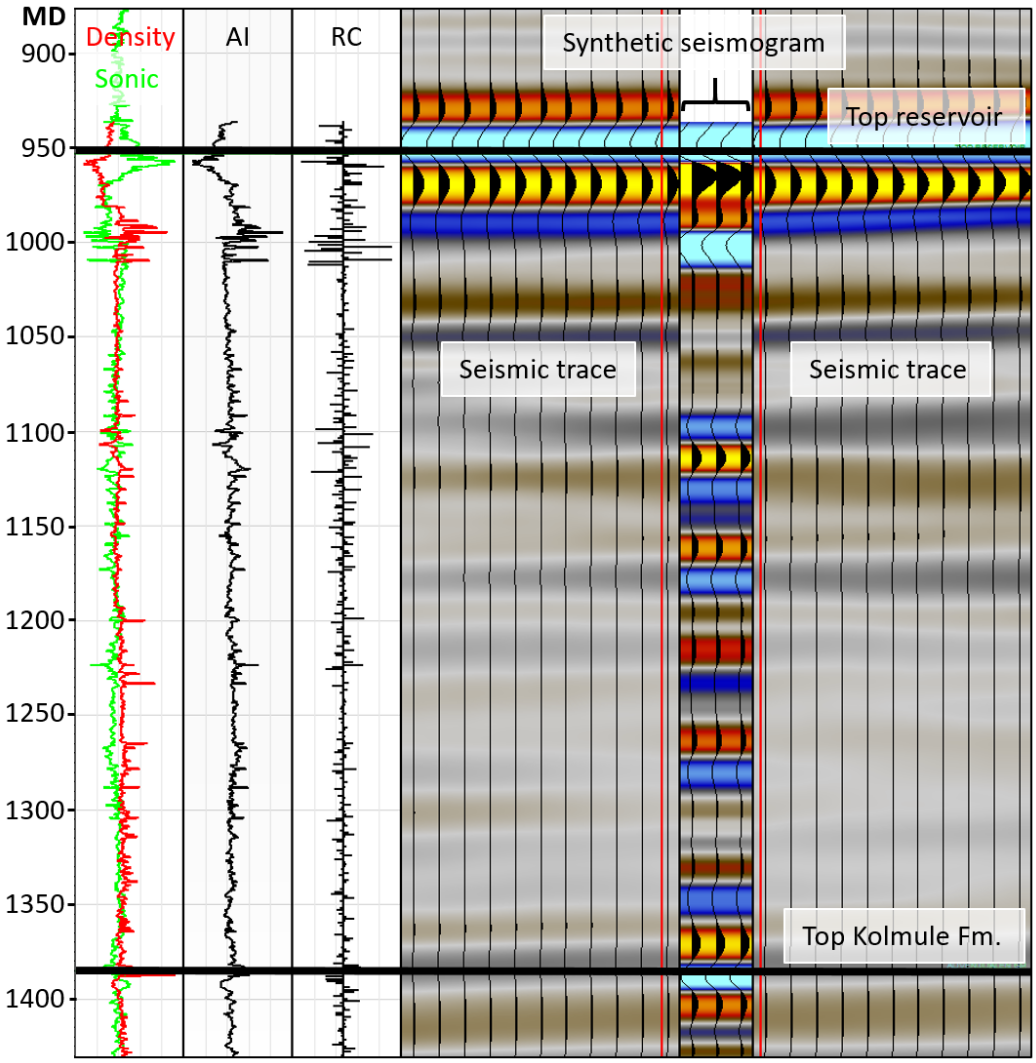

Figure 6.1: *Generated synthetic seismogram. The density and sonic logs, acoustic impedance (AI) and reflection coefficients (RC) are displayed together with the resulting synthetic seismogram and the seismic trace from 2D seismic line MCG 310. No depth shift has been applied to the synthetic seismogram. The red vertical lines close to the seismogram show the well trajectory. The top reservoir and top Kolmule Formation identified from the well data are shown by black horizontal lines. The true vertical depth (TVD) has been assumed equal to the measured depth (MD) because of the low maximum inclination of the well. The sonic scale ranges from 88 $\mu s/ft$ to 173 $\mu s/ft$ and the density scale ranges from 1.9 g/cm^3 to 2.9 g/cm^3.*

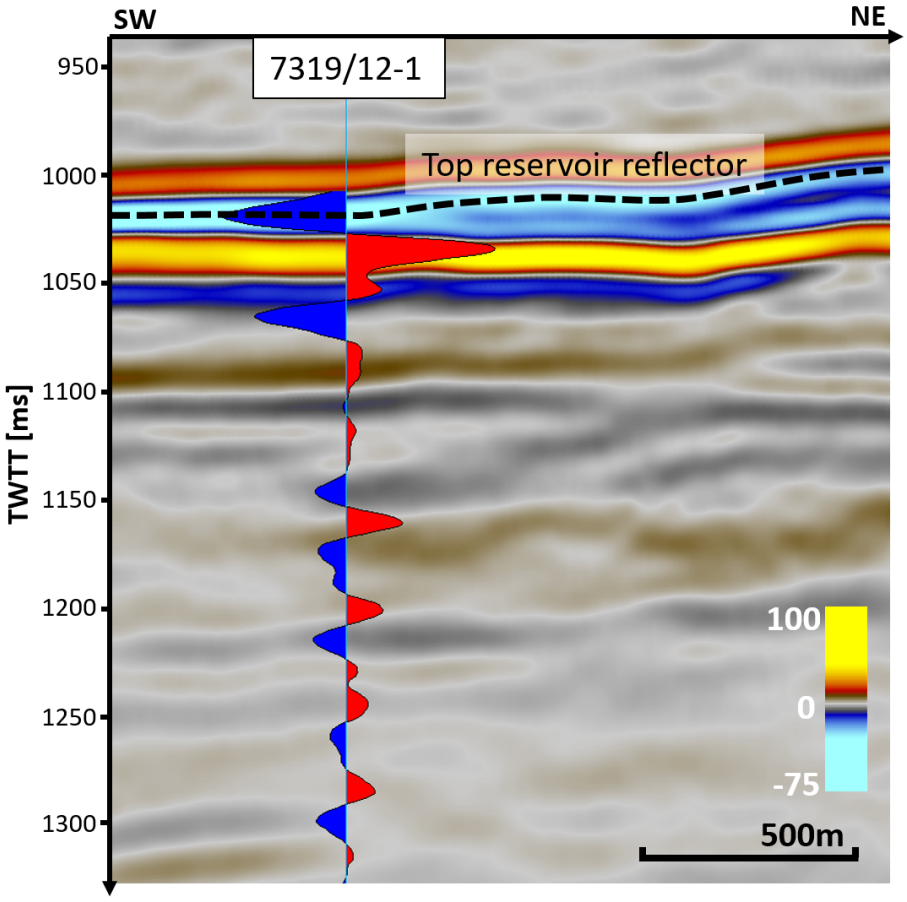

Figure 6.2: *Quality control of the generated synthetic seismogram. The wiggles from the synthetic seismogram match well with the reflections from the 2D seismic line MCG 310 crossing the Pingvin discovery. The strong blue reflector at about 1020 milliseconds (ms), marked by the black dashed line, represents the seismically interpreted top reservoir.*

6.2 Seismic Interpretation

6.2.1 Seismic Stratigraphy of the Study Area

Figure 6.3 shows one of the 2D MCG seismic lines used for interpretation, which is line MCG 308 in Figure 4.1. The associated interpreted section is presented in Figure 6.4. Figures 6.5 and 6.6 show the uninterpreted and interpreted seismic line MCG 310, crossing the Pingvin gas discovery. A total of nine horizons have been interpreted in the study area, dividing the strata into nine seismic units. The characteristics of the units have been based on the interpretation from Figures 6.4 and 6.6 and are discussed below.

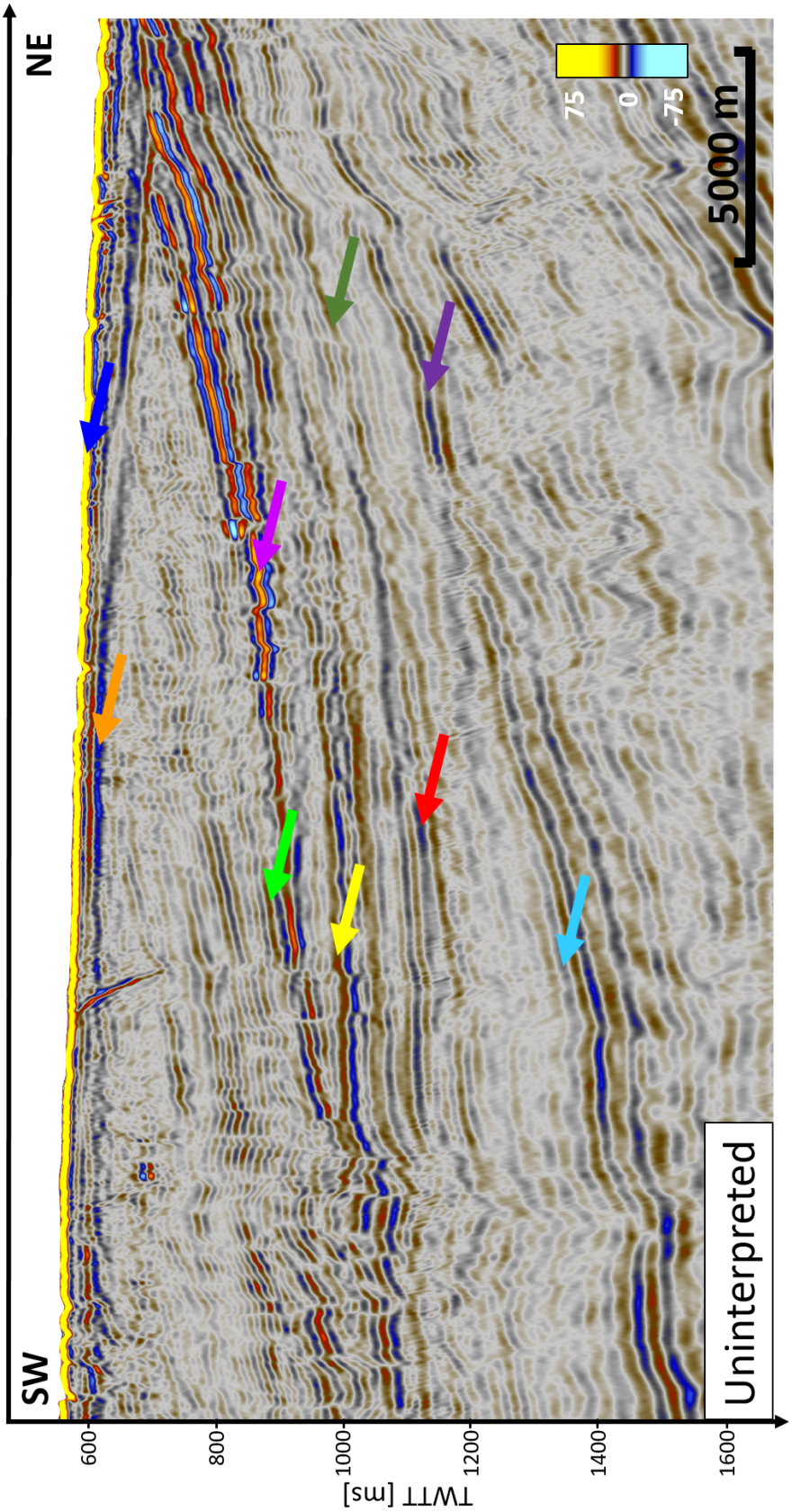

Figure 6.3: *Uninterpreted 2D seismic section MCG 308. See Figure 4.1 for location in map view. Colored arrows indicate the top of the interpreted seismic units. No direct hydrocarbon indicators have been identified. The data is measured in two-way traveltime (TWTT).*

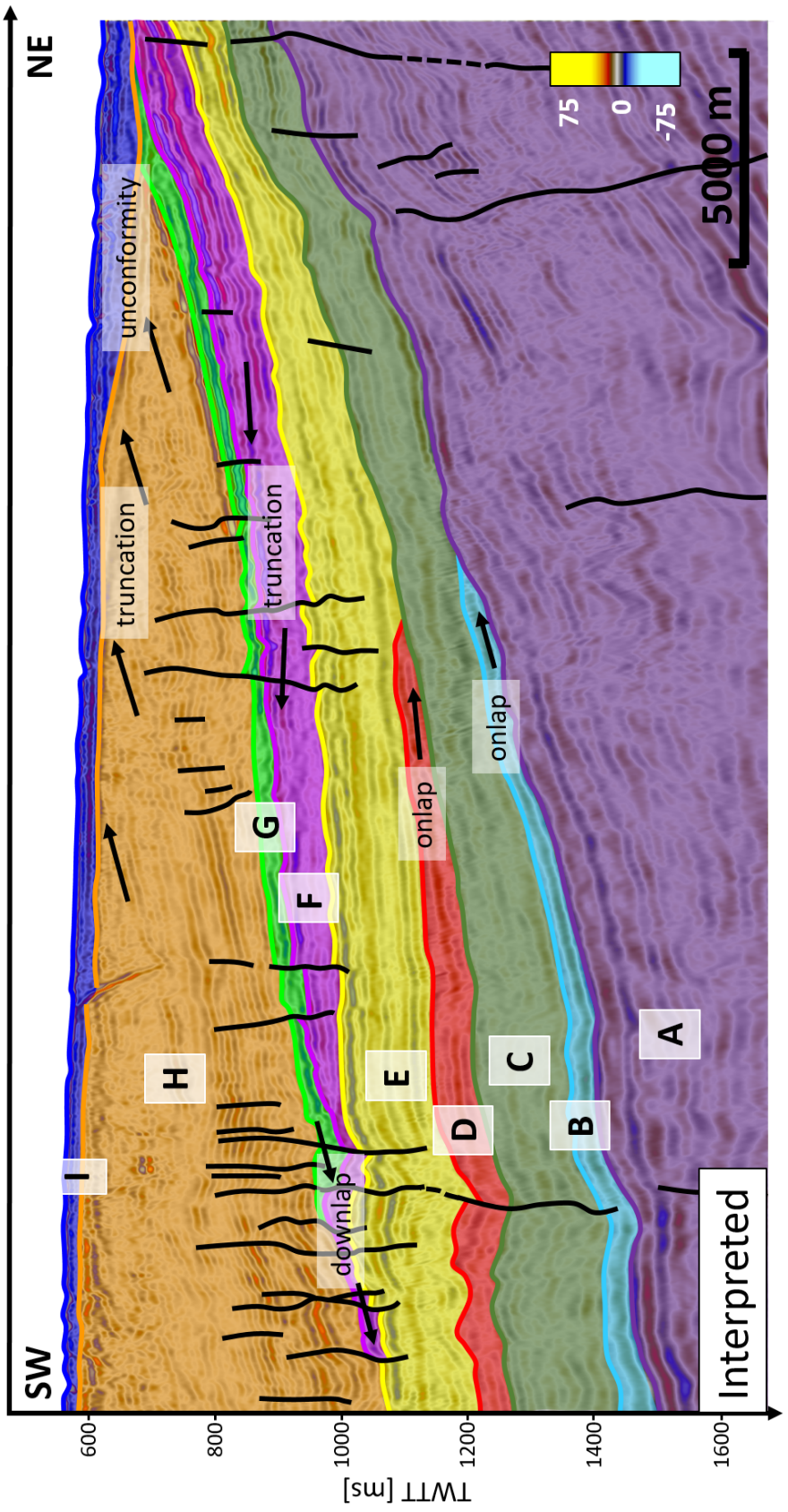

Figure 6.4: *Interpreted 2D seismic section MCG 308. See Figure 4.1 for location in map view. Nine horizons have been interpreted and the most prominent faults are shown. Onlaps, downlaps and truncations have been identified. Seismic facies A to H show reflections dipping towards the southwest. Units F and G are thinning towards the southwest, opposite of the surrounding units. The associated uninterpreted seismic section is presented in Figure 6.3. The data is measured in two-way traveltime (TWTT).*

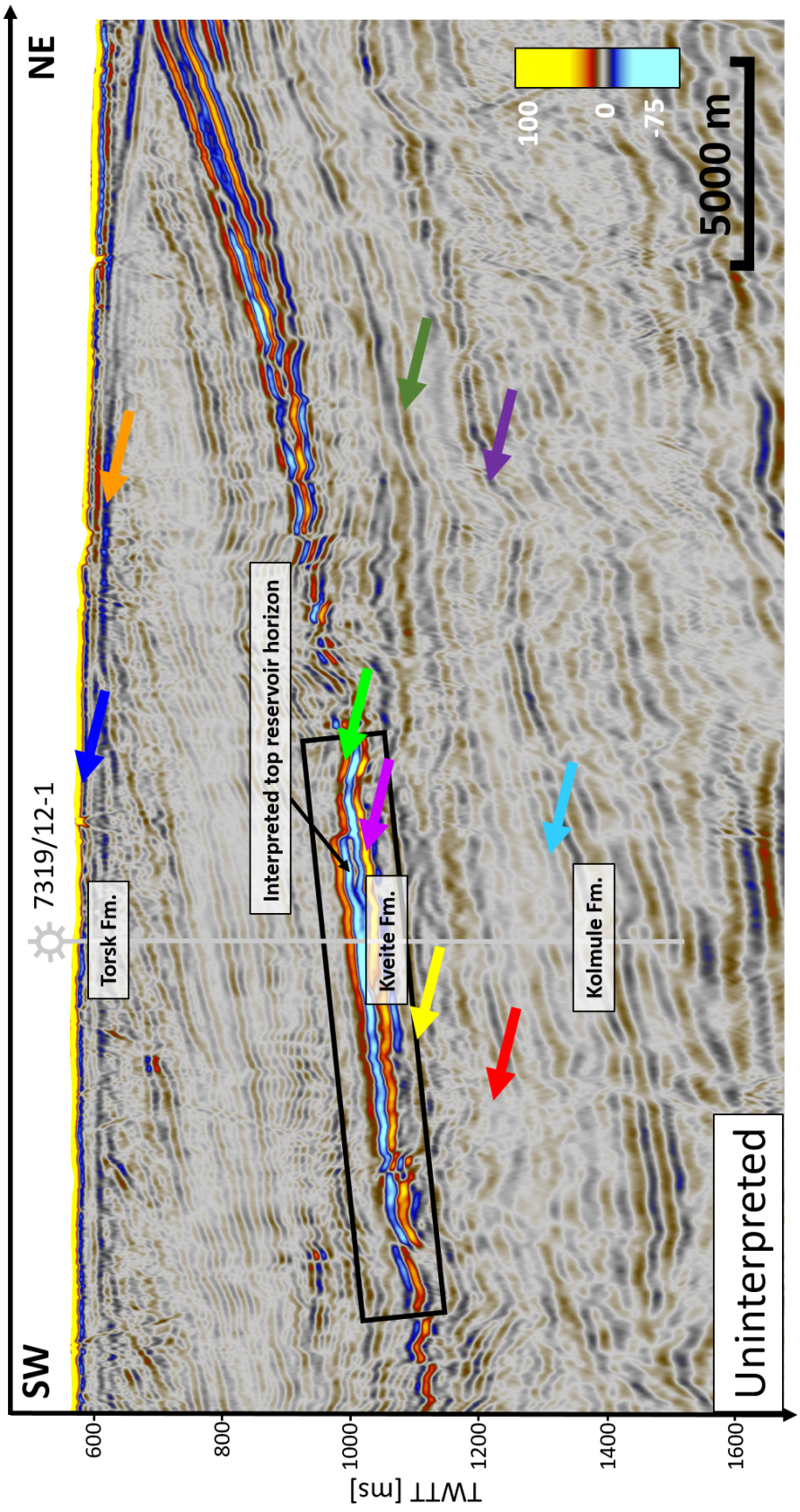

Figure 6.5: *Uninterpreted 2D seismic section MCG 310 and location of well 7319/12-1. See Figure 4.1 for location in maps view. Colored arrows indicate the top of the interpreted seismic units. The black rectangle shows the high amplitude anomaly associated with the Pingvin gas discovery. The well has been drilled through this anomaly. The black arrow shows the interpreted top reservoir horizon. There are large uncertainties in the extent of the seismic anomaly. The data is measured in two-way traveltime (TWTT).*

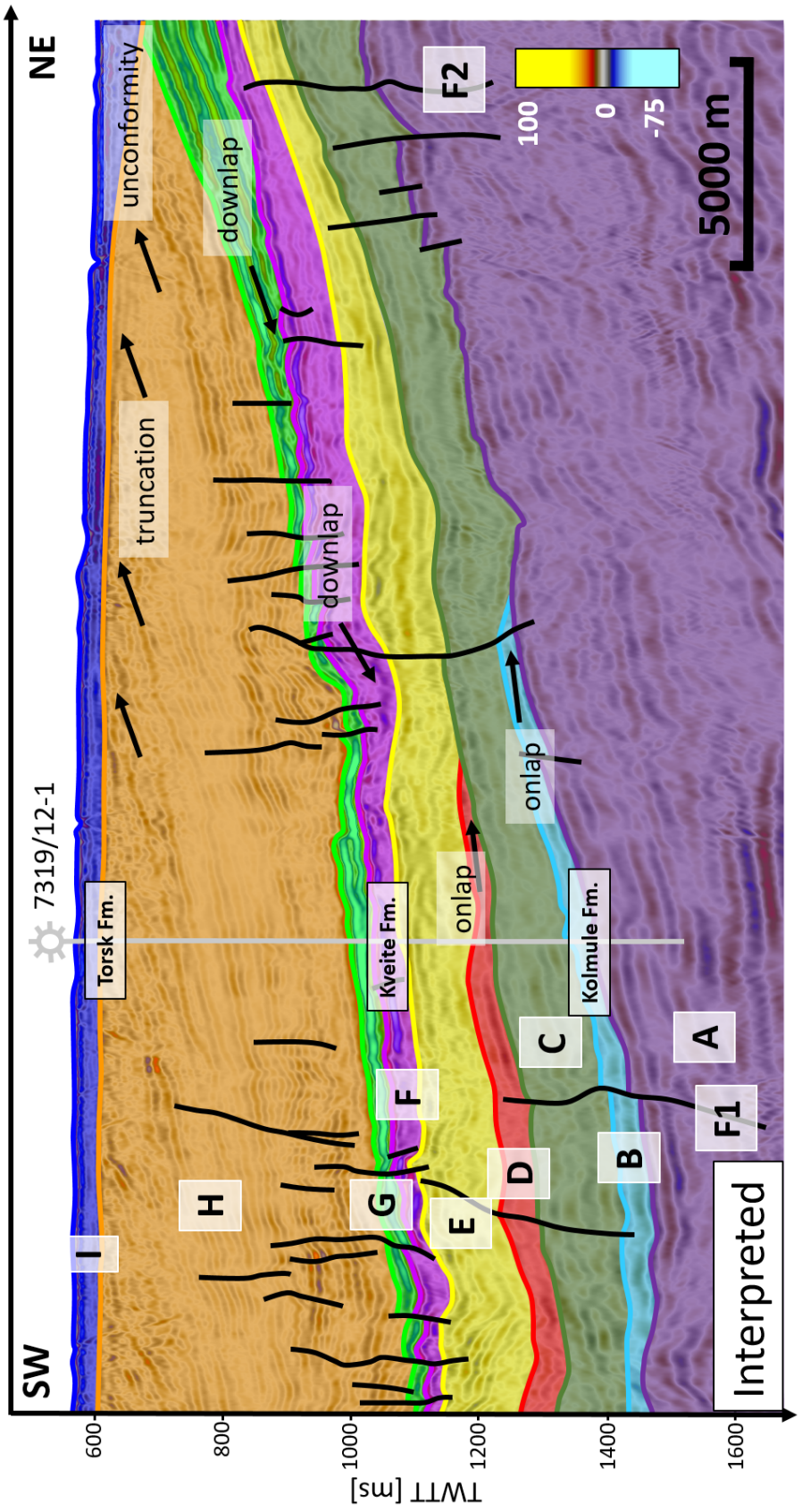

Figure 6.6: *Interpreted 2D seismic section MCG 310 and location of well 7319/12-1. See Figure 4.1 for location in map view. Nine horizons have been interpreted and the most prominent faults are shown. Onlaps, downlaps and truncations have been identified. Seismic facies A to H show reflections dipping towards the southwest. Facies G and F are thinning towards the southwest, opposite of the surrounding units. The area is influenced by normal faults, see e.g. faults F1 and F2. The associated uninterpreted seismic data is shown in Figure 6.5. The data is measured in two-way traveltime (TWTT).*

Seismic facies A:
Seismic facies A is characterized by parallel to sub-parallel reflectors with variations in frequency, amplitude and continuity. The thickness of the unit is relatively constant. According to the well information, the top of unit A corresponds to the top of the Cretaceous Kolmule Formation (see Figure 6.6).

Seismic facies B, C, D and E:
Seismic facies B, C, D and E are all thickening towards the southwest and the units have from well information been identified as being part of the Kveite Formation. The reflectors are semi-continuous and even and wavy parallel, but the units show different internal seismic attributes; parallel, sub-parallel and chaotic. The amplitude changes with depth from medium to high within facies E to low in facies C and B. Onlaps have been identified for facies B and D.

Seismic facies F and G:
Seismic facies F and G are different from the other facies in that they are thickening towards the northeast. Downlaps have been identified in the southwest. The top and base of facies G have been selected because of the very high horizon amplitudes and continuity. The two facies are somewhat faulted, with most of the faults also penetrating the overlying unit, facies H. The seismic anomaly associated with the Pingvin discovery, which is part of the Torsk Formation, has been identified within facies G. The top of the Kveite Formation has been identified within unit F.

Seismic facies H:
Seismic facies H is part of the Torsk Formation. The unit is characterized by even and wavy parallel reflectors with occasional chaotic areas. The frequency is high compared with the facies related to the Kveite and Kolmule Formations and the amplitudes vary between low and high. The facies is relatively thick and faulted in certain areas. The seismic horizon associated with the top of the facies has been difficult to interpret due to low amplitudes and changing colors. This is in accordance with the internal reflectors seen to be truncated by the top facies H horizon. The horizon is an unconformity, indicating a time period of erosion.

Seismic facies I:
The sediments in facies I show parallel, continuous and high amplitude reflectors. The unit corresponds to the Nordland Group, representing the present day seabed deposits.

6.2.2 Structural Surface Maps and Thickness Maps

Selected structural surface maps and thickness maps are presented in this section in order to better understand the development of the basin. The maps are measured in two-way travel time (TWTT). Notice that the distance between the contour lines is not the same for all the maps and that the color scales have been adjusted for each map to clearly see the depth and thickness changes.

The top of the Torsk Formation illustrated in Figure 6.7 incline towards the northeast. Larger depth changes are however observed for the deeper interpreted horizons, like the top of the Kolmule Formation, i.e. the top of seismic facies A (see Figure 6.8). These deeper horizons incline towards the South. The change in dip angle for the reflections within seismic facies I compared with the reflections in H to A indicates a change in the depositional setting marked by the interpreted top facies H horizon.

The seismic facies F and G are suspected of representing fan deposition episodes. This interpretation is based on the observation that these deposits are thickening in different directions than the neighboring units. The top and base surfaces of the suspected fan deposits in facies G incline towards the South (see Figures 6.9 and 6.10), similarly to the neighboring units. Figures 6.11 and 6.12 show that the seismic facies G and F are thickening towards the Northeast and West respectively. The maximum basin subsidence is seen in the South. This interpretation is based on presented 2D seismic sections and the surface and thickness maps. Figures 6.13 and 6.14 indicate larger accumulation space in the South than in the North, considered for deposits below the top of facies H.

6.2.3 Fault Interpretation

It has been observed that the area is mainly influenced by normal faults, indicating an extensional regime. The faults are mainly present in the Torsk and Kveite Formations, with some extending into the Kolmule Formation. The faults F1 and F2 in Figure 6.6 show two of the observed normal faults. The faults are somewhat curved, indicating that the deposits affected by the faulting consist of sediments with changing rock properties.

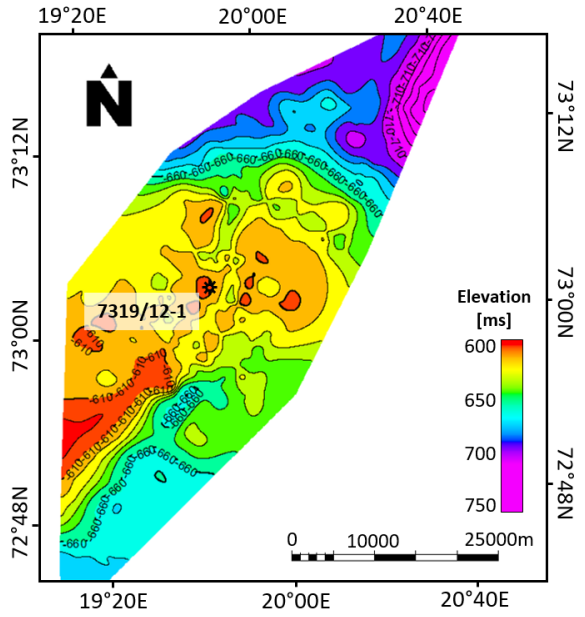

Figure 6.7: *Surface map of the top Torsk Formation, i.e. the top of seismic facies H. The surface incline towards the Northeast. The distance between the contour lines is 10 ms.*

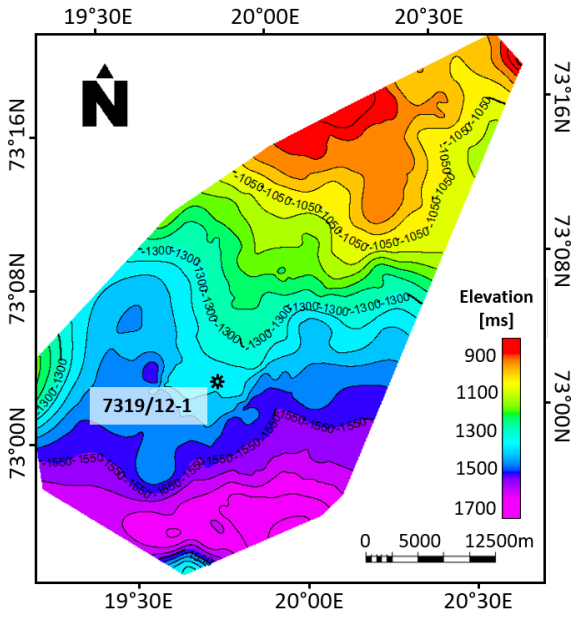

Figure 6.8: *Surface map of the top Kolmule Formation, i.e. the top of seismic facies A. The surface incline towards the South. The distance between the contour lines is 50 ms.*

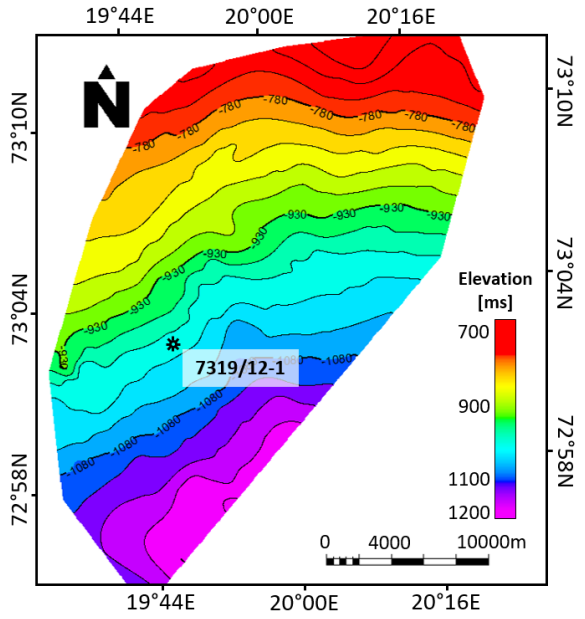

Figure 6.9: *Surface map of the top of the seismic facies G within the Torsk Formation. The surface incline towards the South to Southeast. The distance between the contour lines is 30 ms.*

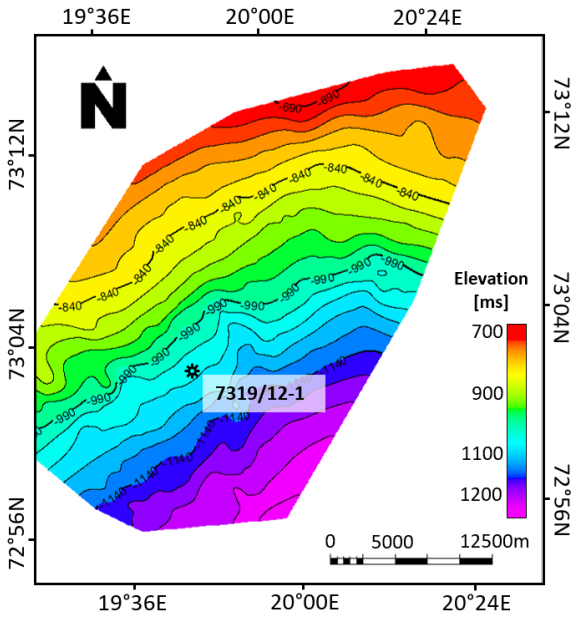

Figure 6.10: *Surface map of the base of the seismic facies G within the Torsk Formation, i.e. the top of facies F. The surface incline towards the South and Southeast. The distance between the contour lines is 30 ms.*

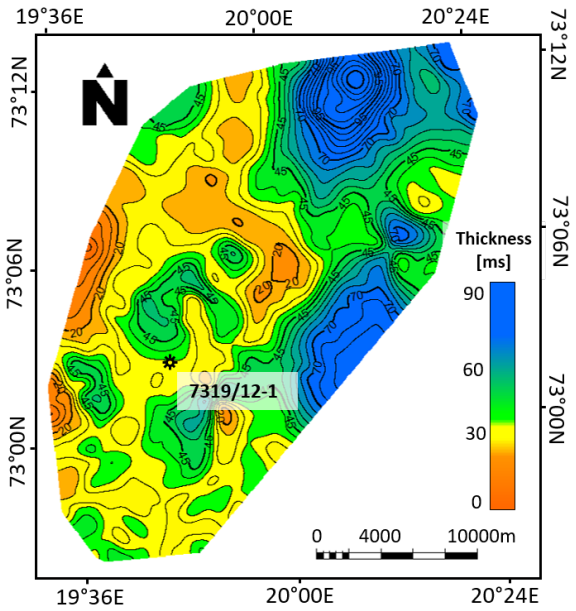

Figure 6.11: *Thickness map of seismic facies G. The seismic unit is thickening towards the East and Northeast. The difference in thickness between the contour lines is 5 ms.*

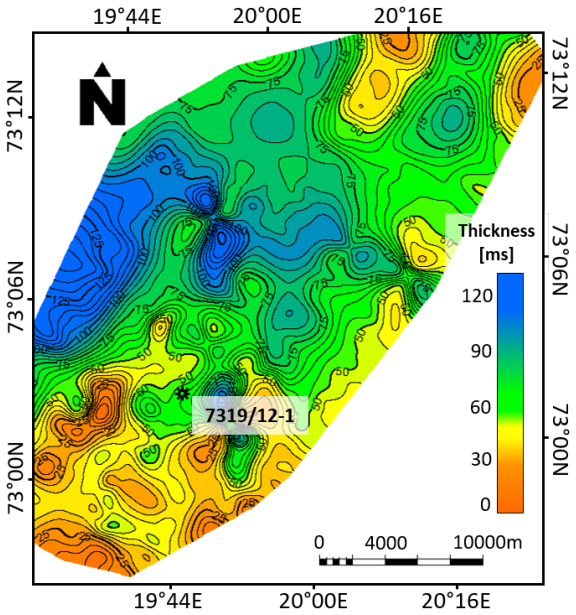

Figure 6.12: *Thickness map of seismic facies F. The seismic unit is thickening towards the West. The difference in thickness between the contour lines is 5 ms.*

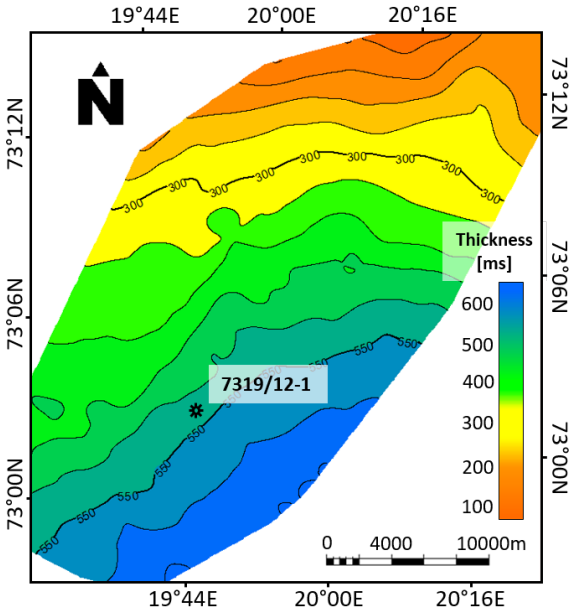

Figure 6.13: *Thickness map between the seabed and the top of seismic facies E. The seismic unit is thickening towards the South to Southeast. The difference in thickness between the contour lines is 50 ms.*

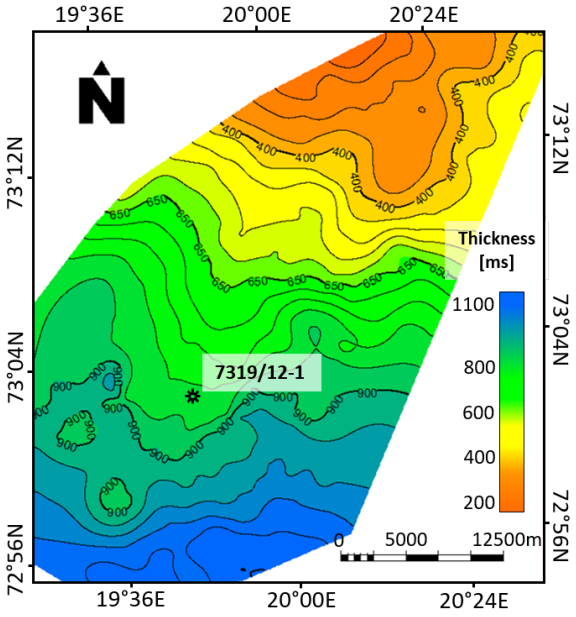

Figure 6.14: *Thickness map between the seabed and the top of seismic facies A. The seismic unit is thickening towards the South. The difference in thickness between the contour lines is 50 ms.*

6.2.4 Interpreted Geological History

The study area represents a subsiding basin, influenced by tectonic forces in an extensional setting. This conclusion is in accordance with the fact that the Bjørnøya Basin developed as a result of the opening of the North Atlantic Ocean (see Section 2.2).

According to Norwegian Petroleum Directorate (ndc), the sediments within the Cretaceous facies A, in the Kolmule Formation, are laterally continuous and consist mainly of claystones and shales. Parallel reflectors and constant unit thickness within this facies indicate uniform basin subsidence. The basin continued to subside in the Late Cretaceous and Tertiary with increased subsidence and accumulation space in the South, indicated by thicker deposits towards the southwest for units B to E in Figures 6.4 and 6.6 and from presented surface and thickness maps. Onlaps have been identified, which is often associated with marine transgression. As the basin has been filling in, the sea level has risen relative to the land. The Kveite Formation's clays and shales have been deposited in a deep shelf environment, supporting the interpretation of a marine depositional environment (Norwegian Petroleum Directorate, ndd).

The seismic units G and F represent a change in the depositional setting. Figures 6.11 and 6.12 show that these facies are not thickening towards the South, but towards the Northeast and West respectively. Downlaps have been identified in the southwest from the seismic sections. It has been believed that these facies are prograding distal fan deposits filling in from the Northeast for facies G and West for facies F. As the Bjørnøya Basin is surrounded by highs and sub-basins, the fan deposits are likely to originate from these areas surrounding the basin (see Figure 4.1). The Kveite Formation has been identified *within* unit F indicating more than one fan deposition event within this unit.

The sediments within seismic facies H have been deposited on top of the fan in facies G. The deposits from A to H have been uplifted and eroded and most likely tilted. This has been indicated by the top Torsk Fm. angular unconformity and the underlying truncated reflectors. Neogene and Quaternary sediments have later been deposited and eroded to today's topography.

6.2.5 The Pingvin Fluid Anomaly

The high amplitude anomaly associated with the Pingvin discovery has been interpreted to be caused by a change in pore fluid content because of the negative change in acoustic impedance at the top of the anomaly, so-called ”soft” event (see Figure 6.5). The reservoir was located within seismic facies G. The top reservoir reflector was continuous and exhibited very high amplitudes. The discovery did not appear to be bound by any prominent faults and no typical hydrocarbon trap structures have been identified. Based on these observations, the reservoir has been identified as a shallow stratigraphic trap.

6.3 Seismic Depth Conversion

The created velocity model is presented in Table 6.1 and the interpreted input horizons are shown in Figure 6.15. The base Cretaceous has mainly been identified based on the regional profile presented in Figure 2.3b and has been given the constant velocity of 2200 m/s. The surfaces assumed to be of Jurassic and Triassic age have been given higher velocities compared with the base Cretaceous, as it was assumed that the velocity increases with depth. The three values are based on sonic log readings from wells 7120/2-1 and 7222/11-1 on the Loppa High. These two wells penetrate the base Cretaceous, unlike the wells 7319/12-1 and 7318/12-1 in the Bjørnøya Basin.

Table 6.1: *Velocity model used for depth conversion. The seabed, top facies F and top Kolmule Formation have been penetrated by the well and the interval velocities between these surfaces have been extracted from the established time-depth relationship from seismic-well tie. The Base Cretaceous, Jurassic and Triassic have been assigned the interval velocities 2200 m/s, 2500 m/s and 2700 m/s respectively.*

Seismic surface	Correction – Well tops	Velocity model	
Seabed	Nordland Group	V = V0 = Vint	V0: Well TDR – Constant
Top facies F	Kveite Fm.	V = V0 = Vint	V0: Well TDR – Constant
Top Kolmule Fm.	Kolmule Fm.	V = V0 = Vint	V0: Well TDR – Constant
Base Cretaceous		V = V0 = Vint	V0 = Constant = 2200 m/s
Jurassic		V = V0 = Vint	V0 = Constant = 2500 m/s
Triassic		V = V0 = Vint	V0 = Constant = 2700 m/s

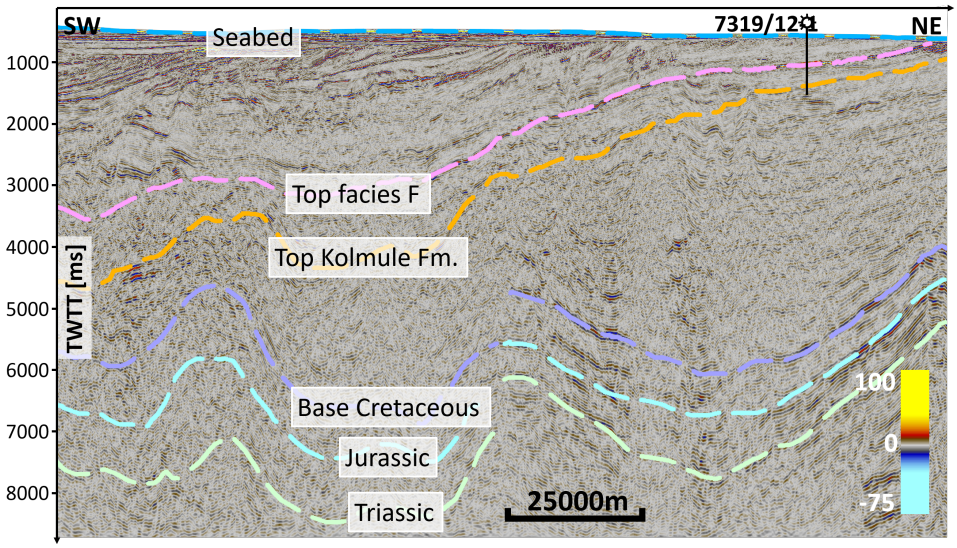

Figure 6.15: *2D seismic section MCG 310 (see Figure 4.1) and interpreted horizons used as input to the velocity model in Figure 6.1.*

Figures 6.16 and 6.17 illustrate the top reservoir surface in time and in depth respectively. The depth converted seismic sections MCG 310 and NH 412-A and the top reservoir surface are shown with the well in Figure 6.18. The depth converted top reservoir surface matches well with the top reservoir in seismic sections and the top reservoir identified from the well, with a maximum of four meters deviation.

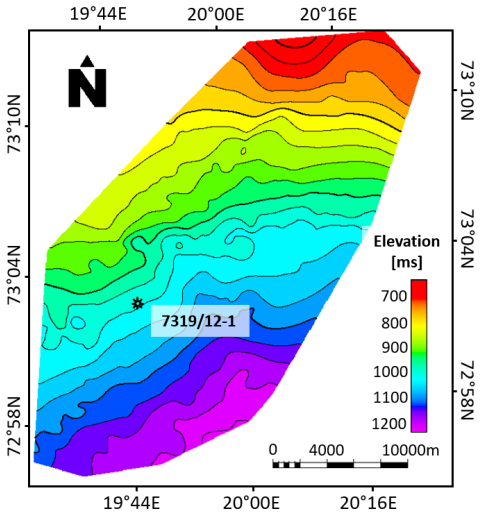

Figure 6.16: *Top reservoir surface in two-way traveltime. The surface incline towards the South to southeast. The distance between the contour lines is 30 ms.*

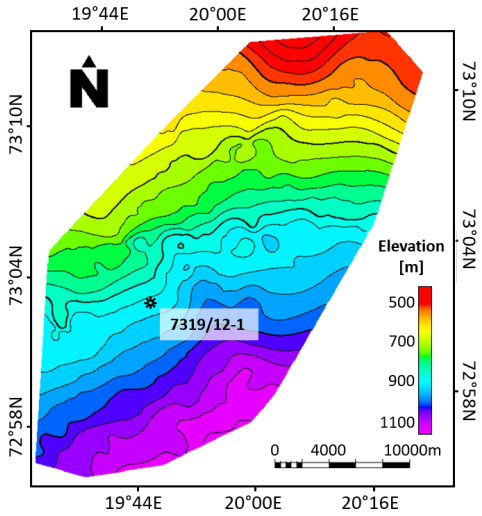

Figure 6.17: *Depth converted top reservoir surface. The surface incline towards the South to southeast. The distance between the contour lines is 30 m.*

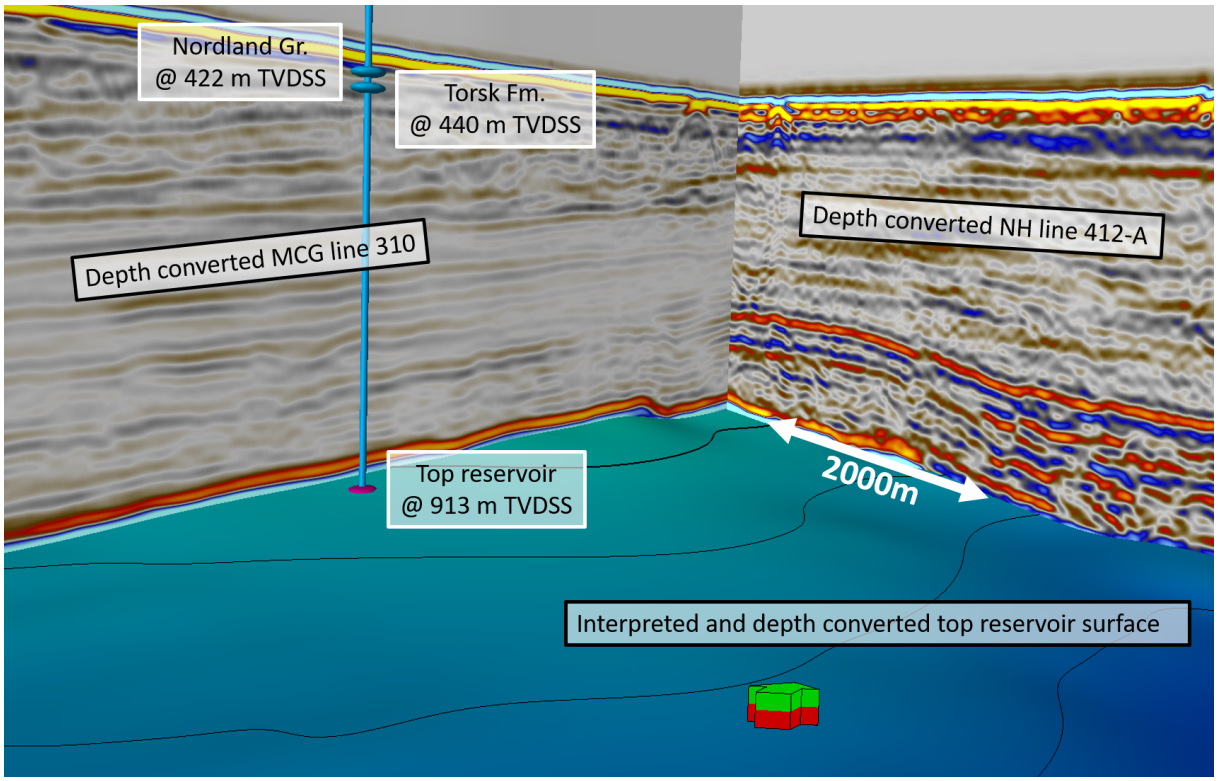

Figure 6.18: *Well tops and depth converted seismic sections MCG 310 and NH 412-A and depth converted top reservoir surface. The depth converted seismic sections and the top reservoir surface match with the top reservoir identified in the well (pink ellipsoid). The match is not as good at the seabed (see the upper continuous, high amplitude, yellow seismic reflector), but it is however the reservoir level that has been in focus in this study. The velocity model presented in Table 6.1 has been used for the depth conversion. The formation tops labeled with white rectangles are those identified in the well. The location of the seismic sections are illustrated in Figure 4.1.*

6.4 Petrophysical Evaluation Results

The available well logs and calculations are presented in Figures 6.19 and 6.20. Be aware that the depths presented in this section are in meters measured depth (MD). The quality of the data has been regarded as good and it has been assumed that the measurements from the well logging tools are correct. The quality of the data is more thoroughly revised in Section 4.2. The well data has been interpreted from 937 to 1015 meters MD which is comprised of the Torsk Formation (480 - 988 m MD) and the Kveite Formation (988 - 1385 m MD) (Norwegian Petroleum Directorate, ndd,n).

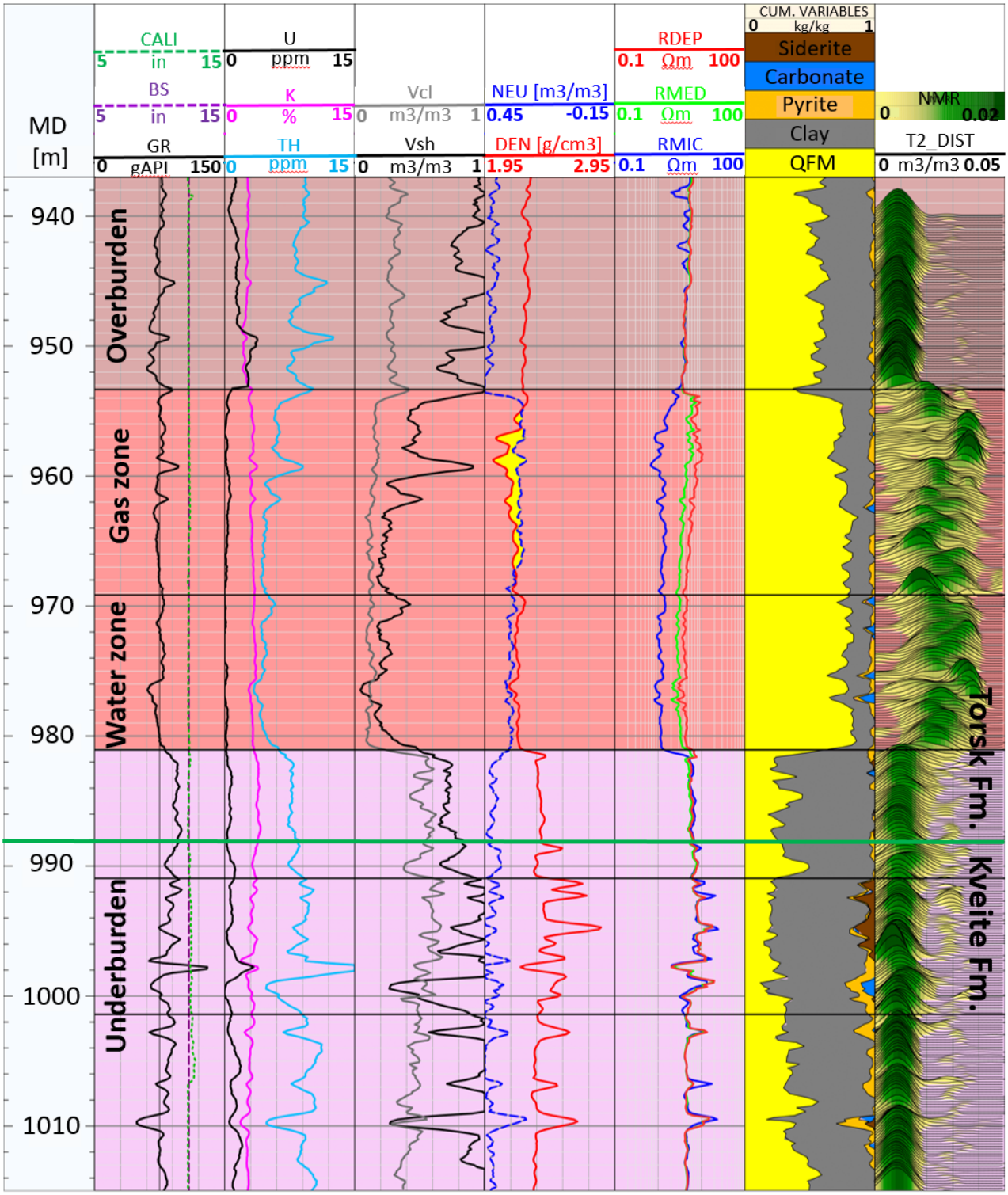

Figure 6.19: *Well log from well 7319/12-1 used for identification of permeable/impermeable beds, lithology and fluid identification and for quantification of shale and clay. The identified overburden shale is colored brown, the sandstone unit is red and the underburden shale is pink. The green horizontal line represents the boundary between the Torsk and the Kveite formations.*

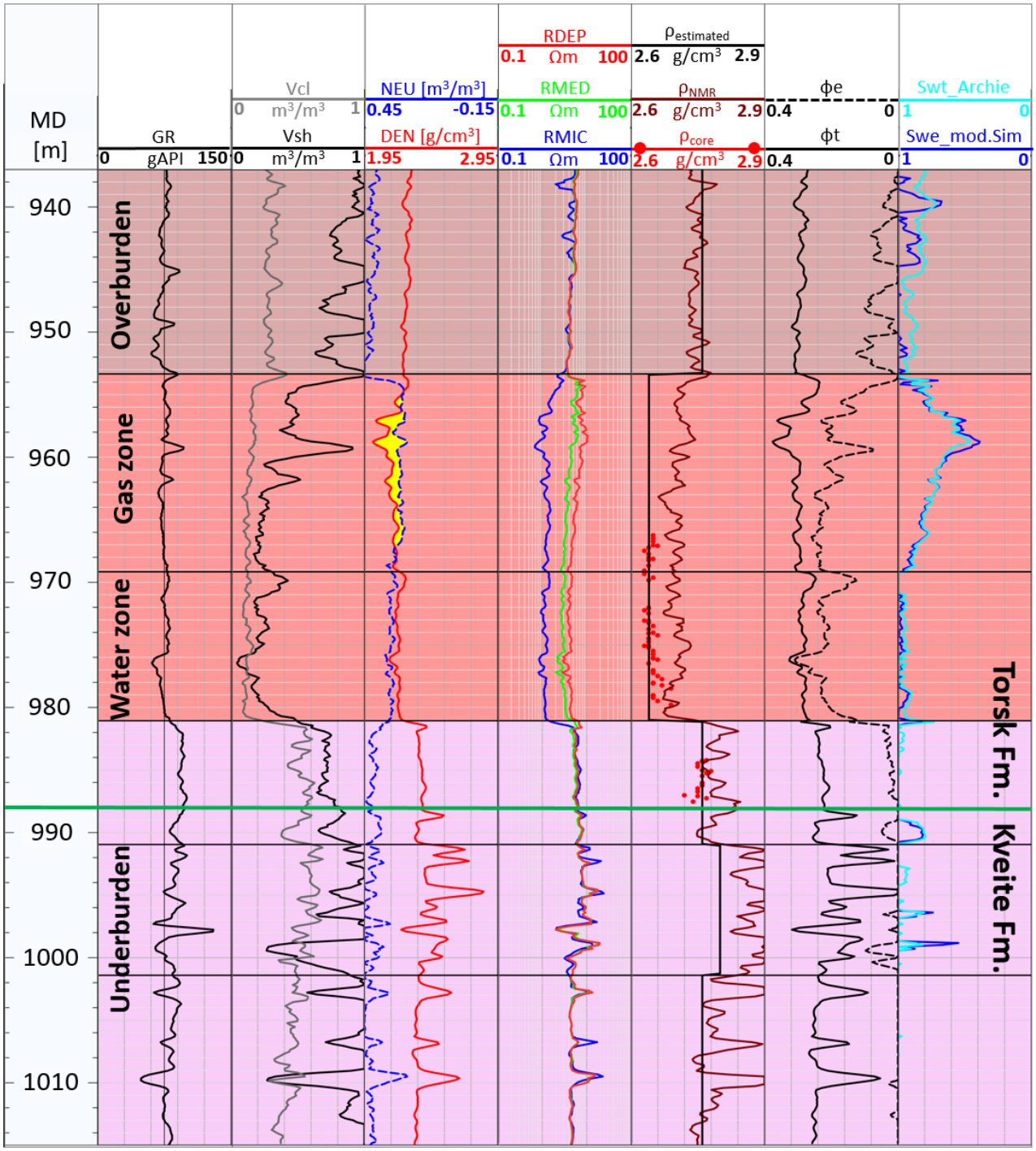

Figure 6.20: *Well log from well 7319/12-1 including estimated effective and total porosity curves and water saturation curves. $\rho_{estimated}$ is the matrix density estimated from core samples and nuclear magnetic resonance (NMR) readings. Curve Swt_Archie represents the total water saturation estimated from the Archie equation and Swe_mod.Sim represents the effective water saturation estimated from the modified Simandoux equation. The identified overburden shale is colored brown, the sandstone unit is red and the underburden shale is pink. The green horizontal line represents the boundary between the Torsk and the Kveite formations.*

6.4.1 Permeable/Impermeable Zones

The interval between 953 and 981 meters stood out from most of the logs. The T2 distribution from the nuclear magnetic resonance (NMR) measurement has within this zone shown larger pores relative to the adjacent zones and resistivity logs with different depth of investigation have measured different values within the interval. The combination of these observations has been interpreted as evidence of invasion of mud filtrate and hence permeability.

The impermeable zones above and below this permeable zone were characterized by overlapping micro, medium and deep resistivity curves. Small pores from the T2 distribution was also a characteristic.

6.4.2 Lithology Identification

The identified permeable zone, ranging from 953 to 981 meters, has been associated with sand deposits. The density log has read values between 2.04 and 2.26 g/cm^3 in the permeable zone and values over 2.26 g/cm^3 in the impermeable zones. Low neutron porosities were encountered in the permeable zone, which is expected for sand deposits. The permeable zone is dominated by weight fractions of quartz, feldspar and mica (QFM). Clay, pyrite and some carbonate and siderite have also been identified, all from the elemental capture spectroscopy (ECS) measurements. For the same zone, core analysis has described a medium to well sorted, poorly cemented and laminated sandstone formation influenced by clay and mica. The lower impermeable zone was dominated by siltstone, which was observed through core analysis. A high clay content has been recognized by the ECS measurements and from the neutron porosity curve, relative to the measurements within the sandstone unit. No cores from the upper impermeable zone have been acquired, but as the log trends are similar to those of the lower impermeable zone, both the zones have been interpreted as shales. Spiking logs in the underburden are likely to have been caused by the presence of a combination of carbonate, siderite and pyrite.

For this case, there has not been any obvious difference between the total gamma ray log reading in the permeable sandstone unit and in the impermeable shales (see Figure 6.19). Mica influences the potassium measurement, which was believed to be the cause of the high total gamma ray readings within the sandstone unit. The results from the cross-plots

in Figures 6.21 and 6.22 support the theory that mica, in addition to clay minerals, are contained within the sandstone deposits. Illite has been identified as the most likely type of clay.

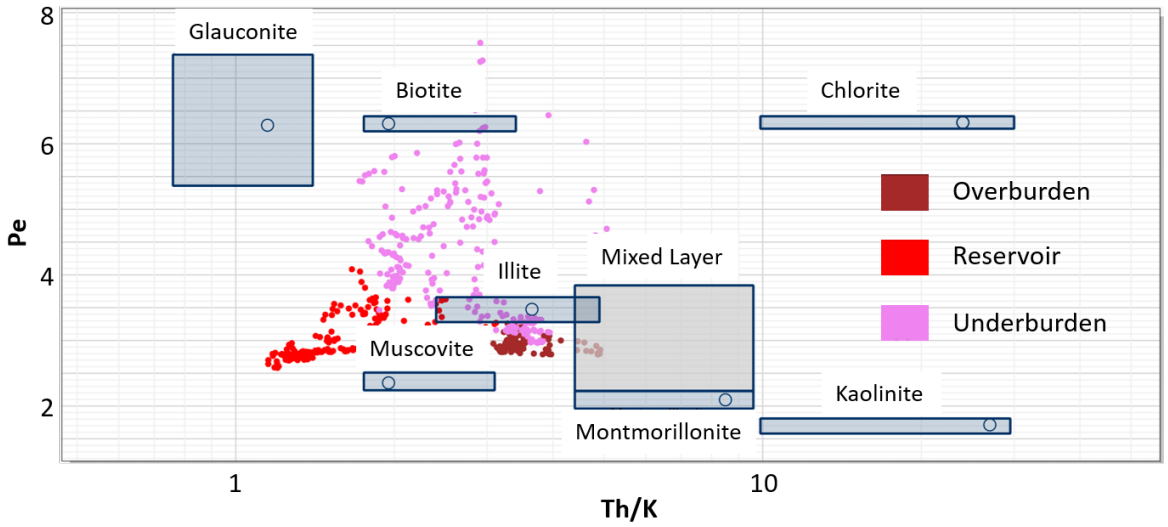

Figure 6.21: *Cross-plot between photoelectric factor (Pe) and thorium-potassium radio (Th/K). The red data points represent the permeable sandstone unit and the brown and pink data points represent the upper and lower impermeable shales respectively. Micas and some clay are suspected contained within the sandstone unit as the data points indicate presence of muscovite and illite.*

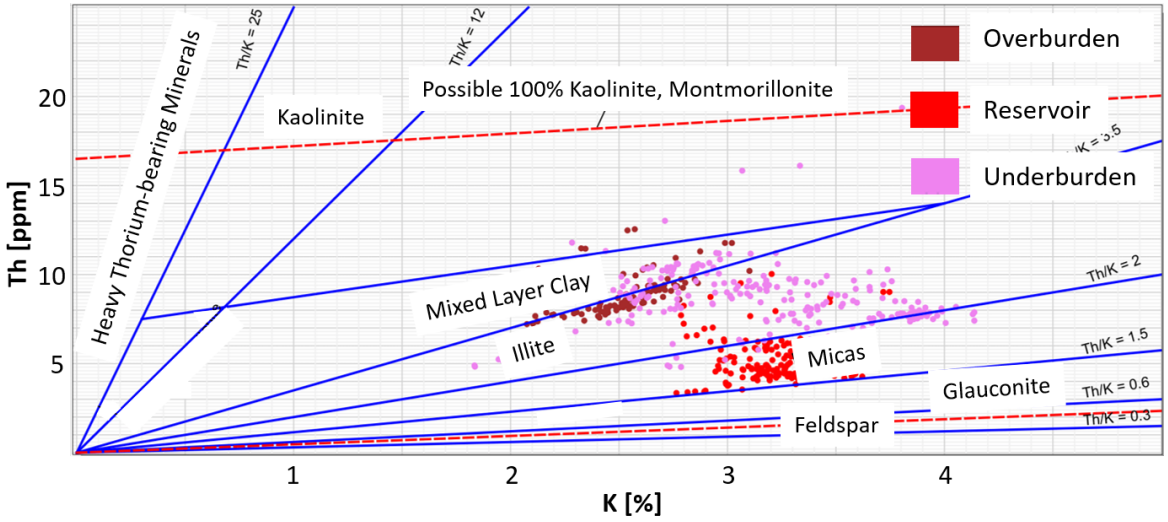

Figure 6.22: *Cross-plot between thorium (Th) and potassium (K) content. The red data points represent the permeable sandstone unit and the brown and pink data points represent the upper and lower impermeable shales respectively. The data points from the sandstone unit indicate presence of mica and illite.*

Shale and Clay Quantification

The bulk volume fraction of shale has been estimated by the use of Equation 5.2 and with GR_{clean}=3 ppm and GR_{sh}=9.6 ppm. The thorium curve has been utilized because of the high total gamma ray and potassium readings within the sand. The GR_{sh}-value has been taken from the overburden shale, as this shale unit and the sandstone unit both correspond to the Torsk Formation (see Figures 6.19). It was assumed that the clay minerals are the same within these two zones. No clean sandstone was encountered by the well and the GR_{clean}-value has therefore been chosen below the lowest thorium reading of 3.1 ppm.

The log representing the bulk volume fraction of shale shows lower volumes of shale within the sandstone compared to the shale units, and decreasing shale volumes with depth internally in the sandstone unit. The volume of clay shows the same trend, with the bulk volume fraction of clay ranging from 16% at the top of the sandstone unit to 9% at the base. The matrix density used for calculating the volume of clay was the $\rho_{estimated}$-curve in Figure 6.20 and the density of illite of 2.77 g/cm^3 has been used as the clay density (Schlumberger, 2009). The clay was believed to be illite because both the charts in Figures 6.21 and 6.22 indicate the presence of illite within the shales. The matrix density was estimated based on core sample measurements and NMR readings.

6.4.3 Fluid Identification

The distinct neutron-density crossover, indicative of gas, has been identified (see Figure 6.19). In combination with the responses from the resistivity curves, the gas zone has been identified within the sandstone unit, from 953 to 969 meters depth. The deep resistivity tool has measured horizontal resistivity values higher than those of the adjacent shales. The gas-water contact (GWC) has been determined at 969 meters because of constant resistivity measurements and no neutron-density crossover below the contact, and based on fluid samples (see Section 4.2) and saturation estimations.

6.4.4 Porosity Estimation

The total porosity presented in Figure 6.20 is a result of the density porosity in combination with the NMR porosity in the gas zone (see Equation 5.6). For the density porosity, different matrix densities have been used for the identified zones; 2.76 g/cm^3 for the overburden shale, 2.64 g/cm^3 for the sandstone unit and 2.76 g/cm^3 and 2.78 g/cm^3 for different zones in the underburden shales (see the $\rho_{estimated}$-curve in Figure 6.20). The water density has been determined at 1.1 g/cm^3 from Chart A.3 with a formation temperature of 21°C, water salinity of 140 000 ppm and a formation pressure of 1360 psi. The combined density and NMR porosity curve has shown total porosities between 28% and 30% in the overburden, between 25% and 35% in the gas zone and between 25% and 32% in the sandstone water zone. The porosities within the reservoir were close to those measured by the core samples. The porosities in the underburden have shown a large range of porosities, between zero to 26%.

As expected, the effective porosity was lower than the total porosity for all the identified zones, with the same trends as the shale volume curve. The effective porosities in the shales in the over- and underburden were low, whereas porosities up to 26% have been estimated within the gas zone. The upper part of the gas zone was characterized by a higher shale content and lower effective porosities than the lower part.

6.4.5 Water Saturation Estimation

The water saturation estimated from the Archie and the modified Simandoux equations are presented in Figure 6.20. The input porosity curves and the volume fraction of shale are given in the same figure. For the Archie equation, the water resistivity (R_w) has been set to 0.304 Ωm. In lack of information on the lithology coefficient a, cementation exponent m and saturation exponent n, one, two and two have respectively been used. R_w, a, m and n used for the Archie equation has also been used for the modified Simandoux equation. The resistivity log reading in 100% shale has been determined at 5 Ωm and extracted from the deep resistivity curve in the overburden shale.

The two resulting curves representing water saturation have shown similar values, but were slightly different because the modified Simandoux equation accounts for the volume of shale. Recall that the curves are not directly comparable because different porosities

have been considered. The average gas saturation from the modified Simandoux equation was 27% within the gas zone and the maximum gas saturation was 61% at 958 meters MD. The gas saturation at the determined gas-water contact was zero.

6.5 3D Unconstrained CSEM Inversion

The 3D unconstrained inversion results are presented in this section, in addition to evaluation of resistivity start model, input parameters and 2.5D inversion results. The location of the CSEM sections presented is shown in map view in Figure 4.3. The depths presented have been measured from the sea level. The objective of running unconstrained inversion has been to test different input parameters and the color scale has not been as thoroughly evaluated for the inversion results as what is described in Section 5.7.

6.5.1 Data Quality Control

Two receivers have been identified from the originally selected receivers (see Figure 4.3), suspected of causing noisy inversion results. Higher data misfit values have been observed for these receivers than for the surrounding receivers. The southernmost of the two receivers has in particularly shown deviating magnitude and phase trends (see Figure 6.23). It was decided to remove the recordings from the two receivers from the data set to prevent the inversions from concentrating on reducing this local misfit instead of focusing on the target and other background areas. Normally, it is not common to remove all data points from one or more receivers, but in this case, the data coverage has not been significantly reduced. Data has been available from the close neighboring receiver of the removed receiver in the North. The southernmost removed receiver was positioned at the edge of the selected receivers, about 15-20 kilometers Southwest of the target. Removing this receiver from the data set has most likely not affected the update of the target.

6.5.2 Parameter Selection and Testing

The cell size and offset ranges have been predetermined prior to running inversion. 200 meters has been used as the horizontal cell size in x and y directions and the vertical cell

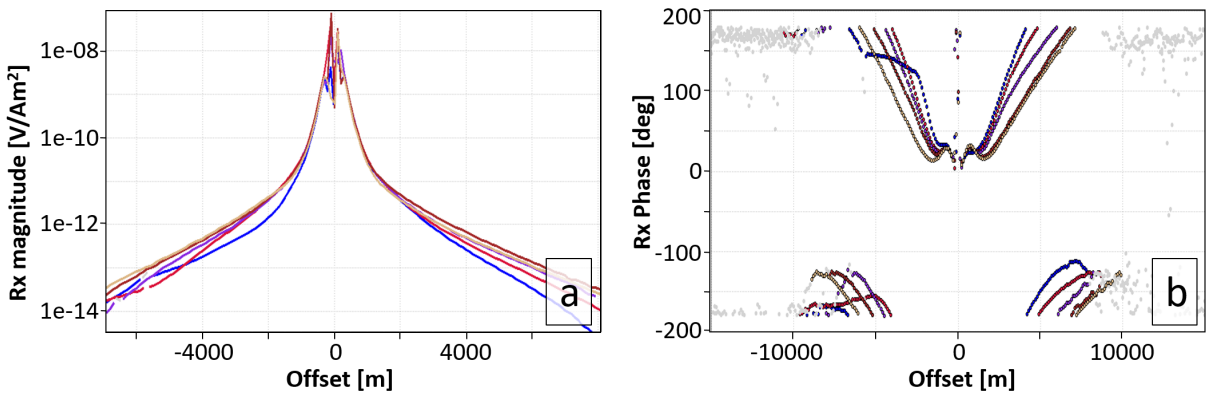

Figure 6.23: *Data quality control through (a) magnitude and (b) phase curves for 1 Hz. The response from the southernmost bad quality receiver removed from the data set for unconstrained inversion (see Figure 4.3) is colored blue and is characterized by deviating magnitude and phase curves relative to the surrounding receivers (the other curves).*

size was set to 47 meters. The minimum offset was set to 1500 meters for all frequencies, whereas the outer offsets were cut at 11 000 meters for 1 Hz, 10 000 meters for 2 Hz, 8 000 meters for 4 Hz, 5 700 meters for 8 Hz, 4 900 meters for 10 Hz and 3 600 meters for 16 Hz.

The frequency spectrums for the two merged CSEM surveys have shown relatively similar amplitude trends. As already indicated, the frequencies chosen for the first inversion job was 1 Hz, 2 Hz, 4 Hz, 8 Hz, 10 Hz and 16 Hz as these exhibited relatively high source signals. The frequency spectrum for survey BSTEN05 is shown in Figure 6.24. The skin depth curve in Figure 6.25 shows that the accumulated gas at Pingvin theoretically can be detected by frequencies up to 25 Hz as the well has proven that the reservoir is located at 913 meters true vertical depth subsea (TVDSS).

The impact of the selected frequencies has mainly been evaluated based on 2.5 inversion results, some of which presented in Figure 6.26. The 2D resistivity start model was designed as a halfspace model with a vertical resistivity of 10 Ωm and a horizontal resistivity of 5 Ωm. The exact same mask file as presented in Figure 5.10 was used. The cell size was set to 100 meters in the horizontal direction and 25 meters in the vertical direction. The resulting background resistivities ranged from 10 to 12 Ωm for all frequencies and at all depths, whereas the abundance of high-resistive anomalies changed. The low-frequency inversion results have been more contaminated by noise than the high-frequency results, but have however been able to image at larger depths. Higher spatial resolution at shallow

depths has been obtained by including the high frequencies. One distinct high-resistive anomaly has been detected for all frequencies, but with more detailed imaging for the high frequencies. It was concluded that all the evaluated frequencies; 1, 2, 4, 8, 10 and 16 Hz, should be included for the unconstrained inversions in order to obtain relatively high spatial resolution at shallow depths and to detect possible deeper geological features.

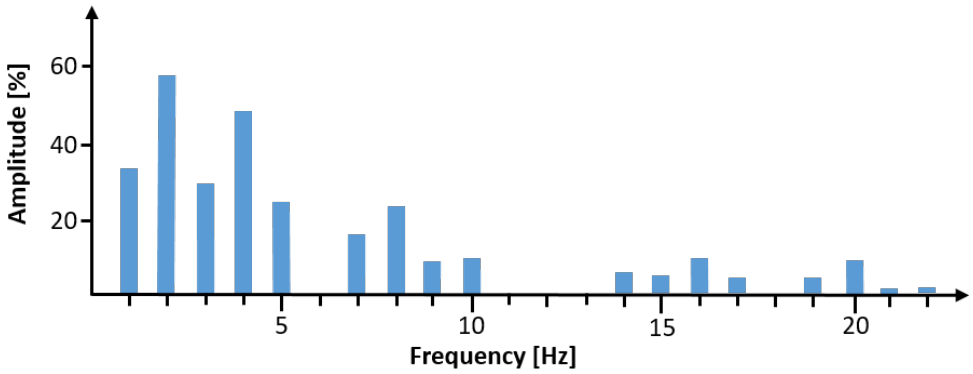

Figure 6.24: *Frequency spectrum for survey BSTEN05 used as basis for the selection of the frequency content to be evaluated through running unconstrained inversions. The frequencies 1, 2, 4, 8, 10 and 16 Hz show relatively high source signals. The frequency spectrum for survey BSTEN04 has shown the same trends.*

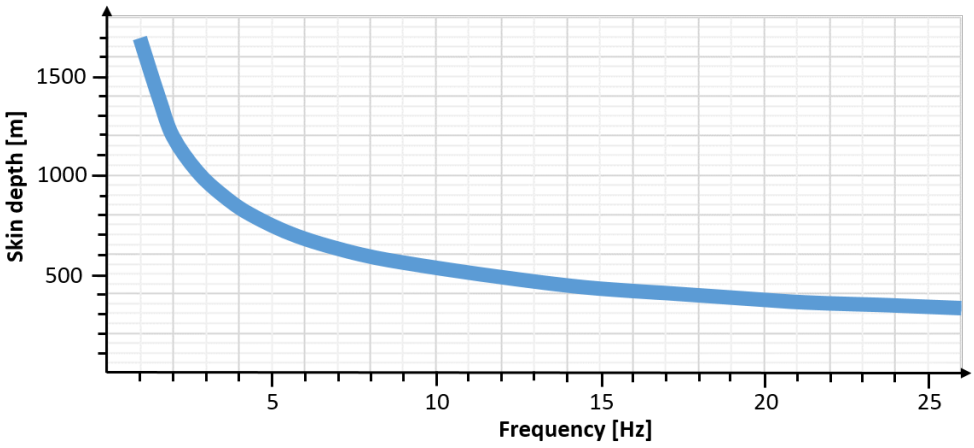

Figure 6.25: *Skin depth curve calculated by using equation 3.2. Based on 2.5D inversion results, a background resistivity of 11 Ωm has been used for the calculation. The Pingvin discovery, with a depth of 913 m TVDSS at the well location, can theoretically be detected by frequencies up to 25 Hz. It was assumed that the depth of investigation is 1.5 times the skin depth.*

Inversion results have proven that regularization has had a considerable effect on the modeling. Applying inadequate regularization, varying degrees of noise were introduced

to the resistivity model, contaminating the target response. Figure 6.27 shows the impact regularization cooling has had on the modeling. The regularization strength has been reduced by one percent for each iteration. The spatial resolution has been greatly improved compared with using constant regularization for all iterations. The model is less smoothed and more detailed.

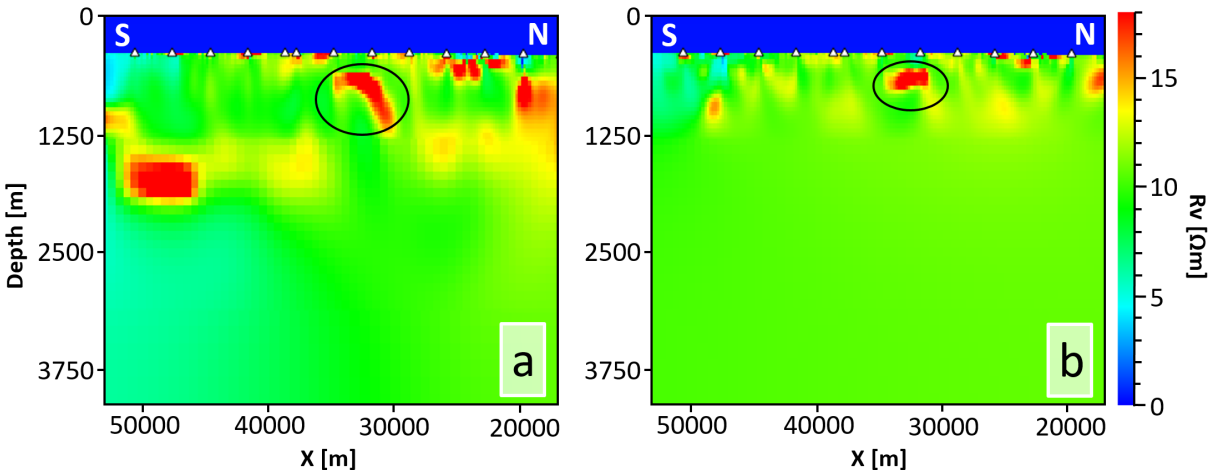

Figure 6.26: *2.5D unconstrained inversion results with frequency as the changing variable. The low-frequency result (1 Hz) in (a) shows noisier imaging of the subsurface than the high-frequency result (16 Hz) in (b), but has been able to detect resistivity trends at larger depths. The high-resistive anomaly observed from all the 2.5D results is marked with a black circle. Recall that X is the source-receiver offset.*

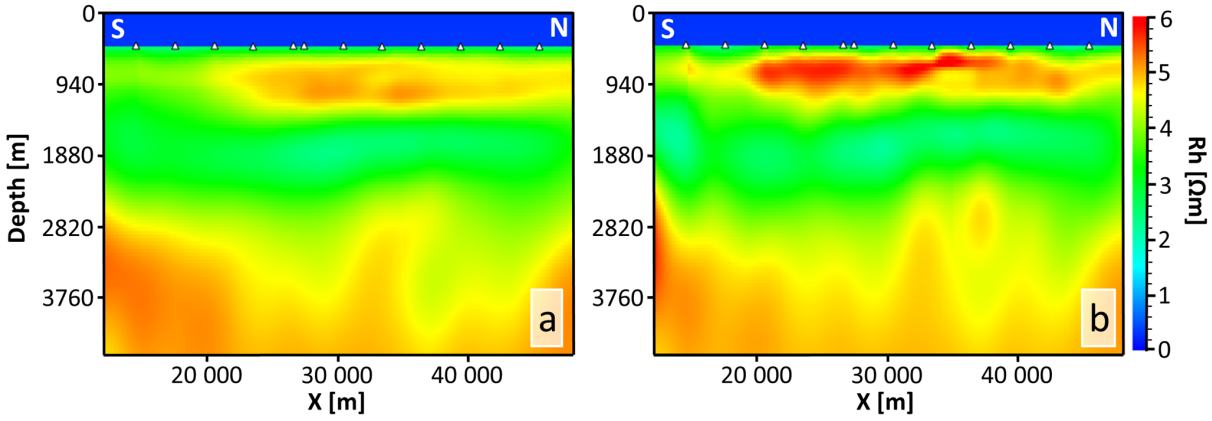

Figure 6.27: *The impact of adjusting regularization parameters for 3D unconstrained inversion results. The horizontal resistivity model in (a) is more smoothed and less detailed than that in (b), respectively created without and with regularization cooling. The cooling has been applied both in the vertical and in the horizontal directions. The regularization cooling showed the largest effect on the horizontal resistivity models compared to the vertical models.*

6.5.3 Start Model

The final start model is presented in Figure 6.28. The model is gradient-based and believed to represent the subsurface resistivity trends. No lateral variations in resistivity have been applied. The model has been built with increasing resistivity with depth. A more complicated model has not been used because it was preferred to let the inversion be largely data-driven. Regardless of the start model used, the target has been detected for all the performed inversions designated to test different start models.

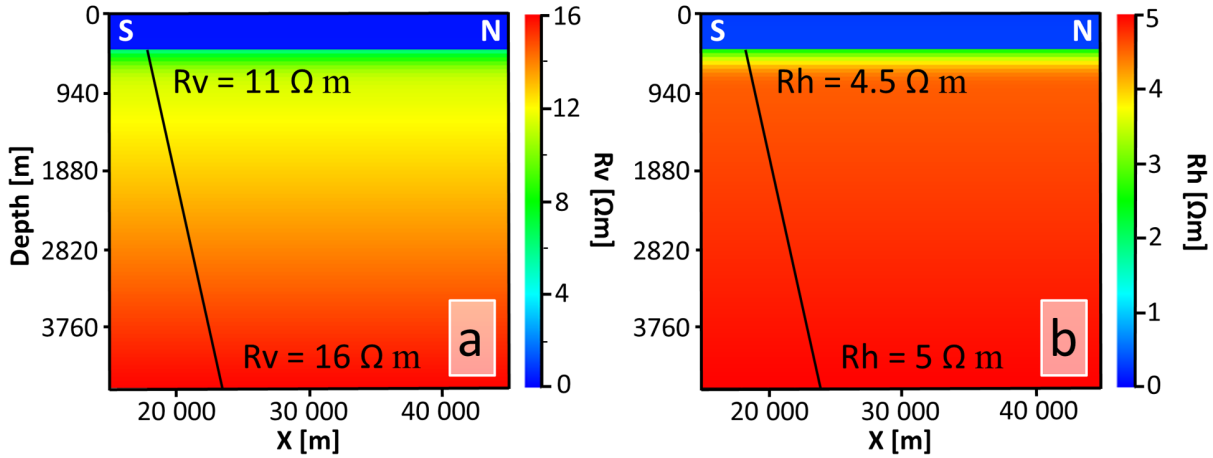

Figure 6.28: *Final (a) vertical and (b) horizontal 3D start model for unconstrained inversion. The models are gradient-based and a resistivity of 11 Ωm at the seabed and 16 Ωm at 4500 meters depth have been assigned to the vertical model. The horizontal resistivity was set to increase from 4.5 Ωm at the seabed to 5 Ωm at 4500 meters depth. It was preferred to let the inversion be largely data-driven and a more complicated model has therefore not been used.*

6.5.4 Unconstrained Inversion Results

Inputs discussed in Sections 6.5.2 and 6.5.3 including the bathymetry file presented in Figure 4.3 have been used to create the final 3D unconstrained inversion result. 26 unconstrained inversion jobs have been run in order to find the most optimal input parameters. The high-resistive shallow anomaly believed to represent the Pingvin discovery has been detected by all the inverted models, regardless of inputs to the inversion. Figure 6.29 shows some of the results from the inversions that have been run. The figure illustrates the impact of start model, frequency and regularization. The final inverted resistivity model, created with the selected input parameters, is presented in Figure 6.30. The model was

chosen based on the relatively high spatial resolution at the reservoir level. The high-resistive anomaly has been detected by the vertical, but not the horizontal resistivity model, indicating that the target is a thin and approximately horizontal resistor. The horizontal background resistivities increased slightly with depth and resistivities ranging from 3 Ωm to 5 Ωm were observed at the reservoir level, i.e. between 600 and 1000 meters depth. The vertical background resistivities also increased with depth, but with relatively high resistivities in the North. Vertical background resistivities between 11 and 15 Ωm have been obtained at the reservoir level. Both the resistivity models have been updated more at shallow than at large depths (below 3000 m). The maximum vertical resistivity obtained within the high resistive anomaly for the section presented was 95 Ωm.

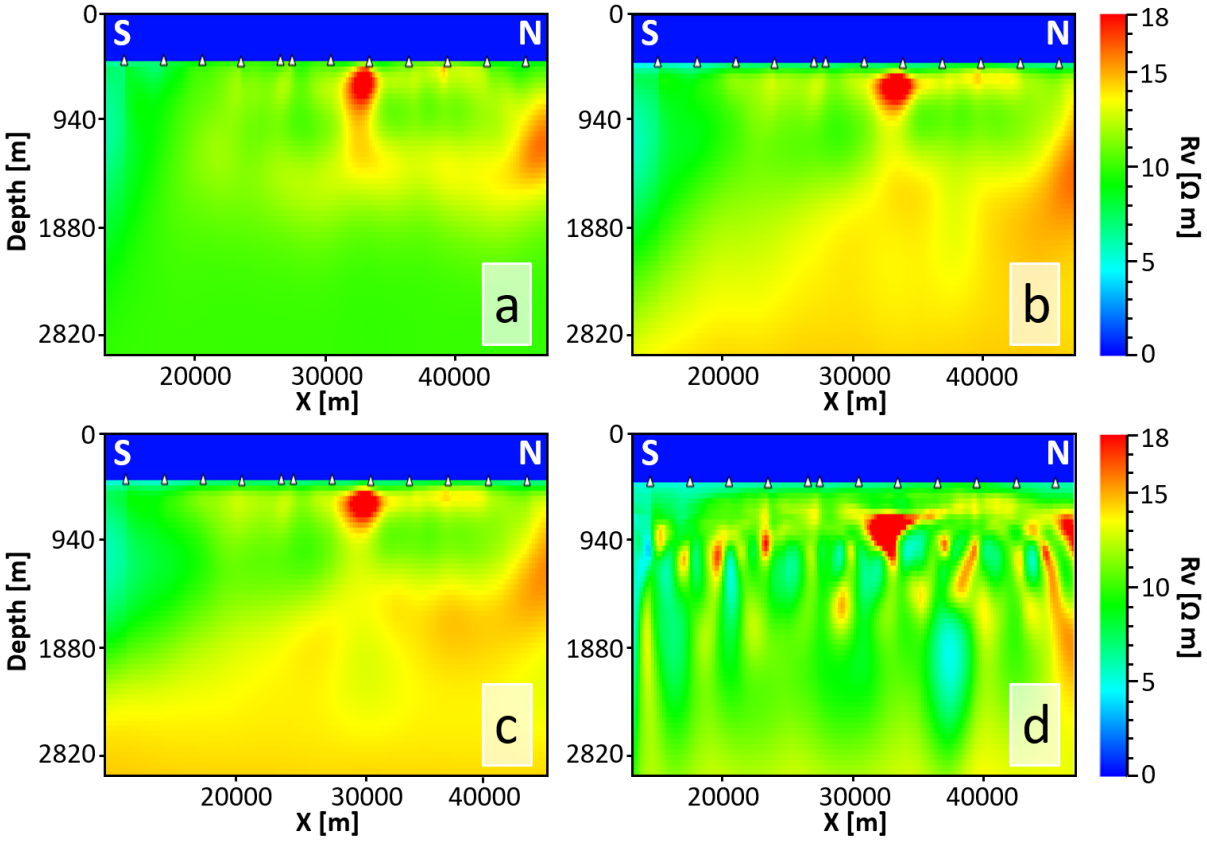

Figure 6.29: *3D unconstrained vertical resistivity models. The background resistivity has not been properly updated in (a), which was built with a halfspace start model with a constant sub-surface resistivity of 10 Ωm. The result in (b) was created by using the frequencies 1, 2, 4, 8 and 10 Hz, i.e. excluding 16 Hz. The result in (c) was created only with the frequencies 4 and 10 Hz. Compared to the final vertical resistivity model in Figure 6.30a, the spatial resolution at shallow and large depths have been considered as not satisfying in (b) and (c). The end data misfit for the model in (d) was close to one, but the model has been influenced by a lot of noise, mainly caused by incorrect regularization parameters.*

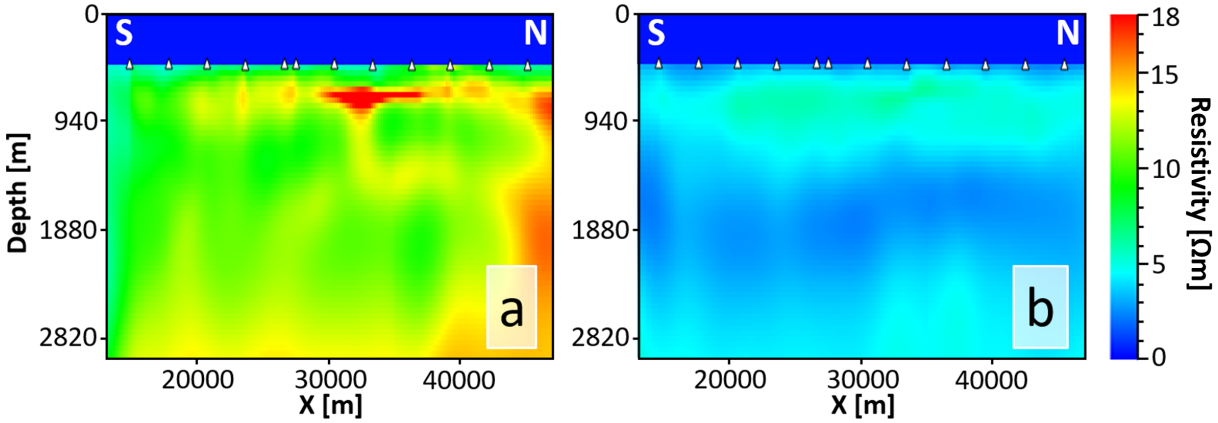

Figure 6.30: *Final 3D unconstrained (a) vertical and (b) horizontal resistivity model. As expected for thin horizontal high-resistive layers, a response has been observed from the vertical, but not the horizontal model.*

6.5.5 Uncertainty Evaluation

The curve in Figure 6.31 represents the total data misfit associated with the final unconstrained inversion result in Figure 6.30. The start data misfit multiplied by the data uncertainty of 3% has given a start misfit of about 62%. The data misfit converged with increasing number of iterations giving an end misfit of 4.6% (end misfit of 1.54 times data uncertainty of 3%) at iteration 100. Iteration 100 was selected for the final inversion result because features believed to represent noise from receivers have been updated for higher iterations. The distinct high-resistive anomaly was not changed for higher iterations.

In terms of the resistivity model, the Pingvin anomaly has been easily seen from the vertical resistivity cube with minimal noise like noise associated with the CSEM receivers.

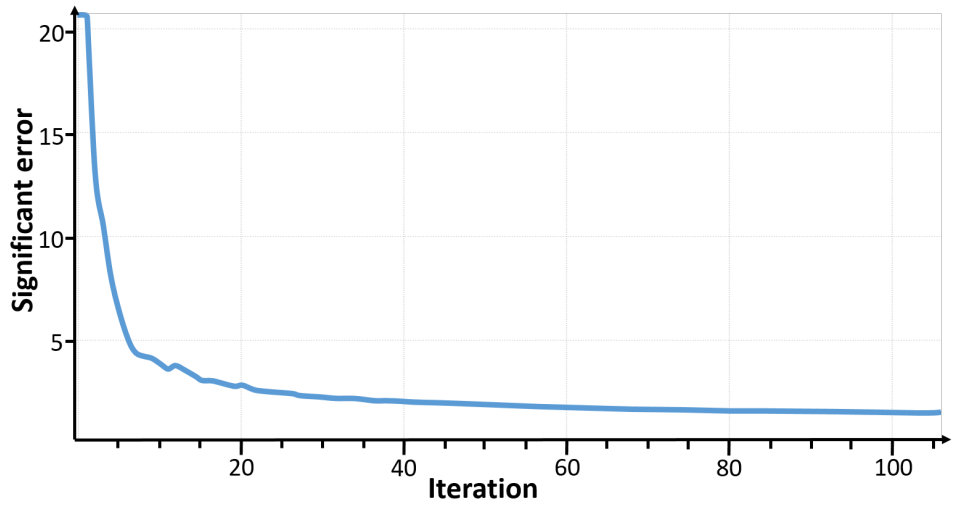

Figure 6.31: *Total data misfit for the final unconstrained inversion result in Figure 6.30. The misfit converged with increasing iterations, giving an end misfit of 4.6%. Ideally, the end misfit should however be closer to the data uncertainty of 3%.*

6.6 3D Constrained CSEM Inversion

The location of the CSEM sections presented in this section is shown in map view in Figure 4.4. The depths presented have been measured from the sea level. The color scale has not been as thoroughly evaluated for the constrained inversion results as what is described in Section 5.7.

6.6.1 Start Model Evaluation and Building

Slightly different resistivities have been observed for the final unconstrained inversion result than for the associated start model. Vertical resistivity contents from selected average resistivity maps from the start model and the inversion result are shown in Figures 6.32 and 6.33. From the unconstrained inversion result, the subsurface vertical resistivities are seen to decrease from about 12 Ωm between the seabed and 900 meters depth towards 10.5 Ωm between 900 meters depth and 1400 meters depth, before constantly increasing to 16 Ωm at 4000 meters depth. Approximately the same trend has been observed for the horizontal background resistivity. Figures 6.34 and 6.35 show two of the histograms used to build the new horizontal start model for constrained inversion.

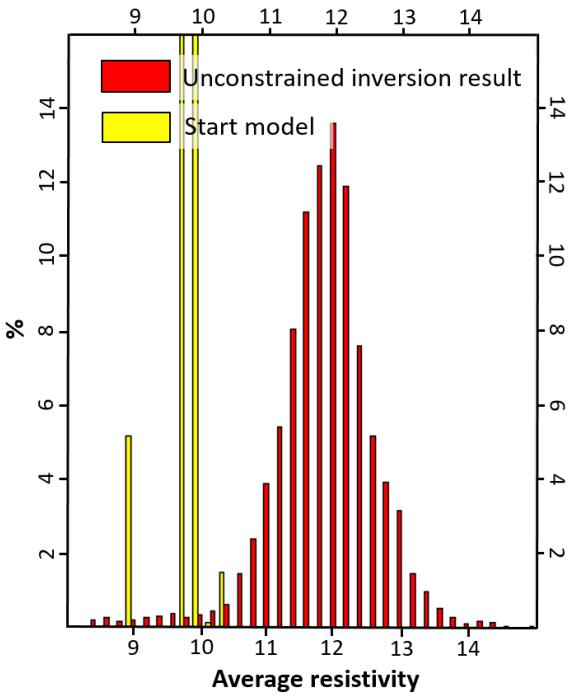

Figure 6.32: *Average vertical resistivities for the final unconstrained inversion result and the associated start model from the seabed and to 900 meters depth. The resistivity content from the inversion result shows a large contribution of resistivities around 12 Ωm and the start model to be used for constrained inversion should therefore be build with approximately this same value within this depth interval.*

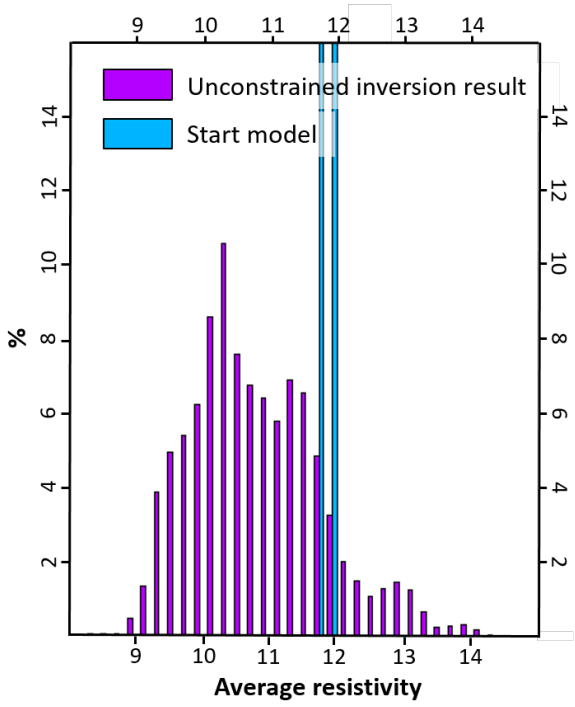

Figure 6.33: *Average vertical resistivities for the final unconstrained inversion result and the associated start model from 900 meters to 1400 meters depth. The resistivity content from the inversion result shows a large contribution of resistivities between 10 and 11 Ωm and the start model to be used for constrained inversion should therefore be build with approximately these same values within this depth interval.*

The final vertical and horizontal start models, which have been created based on the results from the histogram comparisons, are presented in Figure 6.36. The histograms demonstrated that the vertical resistivity decreased from the seabed and down to approximately 1000 meters and that the horizontal resistivity decreases from the seabed and down to 1500 meters depth. Both the horizontal and the vertical resistivities increased for larger depths. As a compromise, the final vertical and horizontal start models have been built with decreasing resistivities down to 1200 meters depth and increasing resistivities down to 4000 meters. The start models were considered as not too simple, nor too complicated and believed to reflect the background resistivity trends.

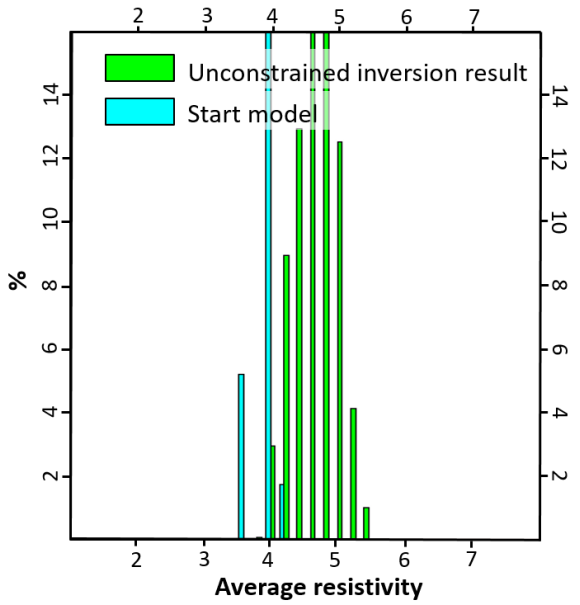

Figure 6.34: *Average horizontal resistivities for the final unconstrained inversion result and the associated start model from the seabed and to 900 meters depth. The resistivity content from the inversion result shows a large contribution of resistivities around 4.5 Ωm and the start model to be used for constrained inversion should therefore be build with approximately this same value in this depth interval.*

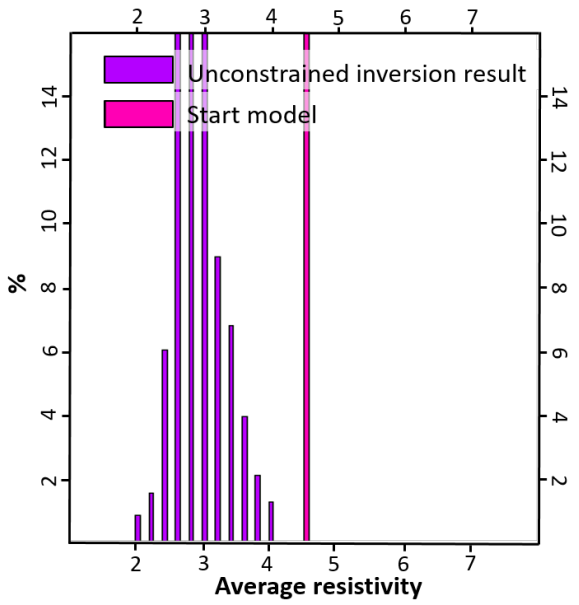

Figure 6.35: *Average horizontal resistivities for the final unconstrained inversion result and the associated start model from 1400 meters to 1900 meters depth. The resistivity content from the inversion result shows a large contribution of resistivities around 3 Ωm and the start model to be used for constrained inversion should therefore be build with approximately this same value in this depth interval.*

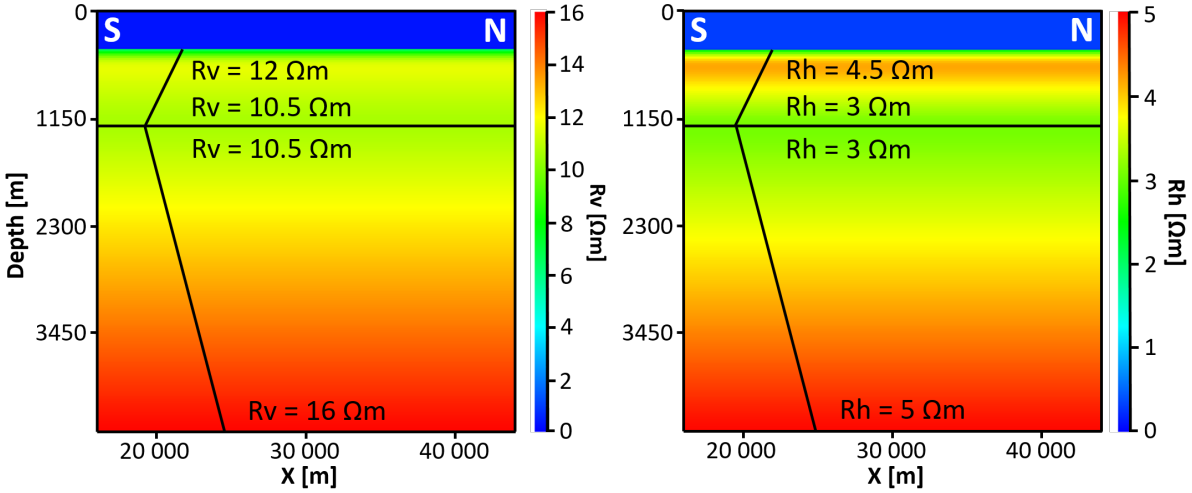

Figure 6.36: *Final start model for 3D constrained inversion. Flat surfaces have been inserted at 470 meters depth (right below the seabed) and at 1200 meters depth to account for changing resistivity trends. Both the vertical and the horizontal start models have been created with decreasing resistivities from the seabed to about 1200 meters depth and increasing down to 4000 meters depth.*

6.6.2 Weight Grid Model Building

Figures 6.37 and 6.38 represent the types of regularization weight grid models that have been evaluated. Regarding the model in Figure 6.37, the higher the regularization weight applied in the over- and underburden, the higher the end data misfit. Based on the total misfit and the abundance of noise in the inverted resistivity model, 0.1 was considered as the most optimal of the tested background regularization weights.

For the model in Figure 6.38, an extra layer, between the seabed surface and the same surface copied and moved two cells down, has been included. As with the reservoir layer, the inversion was allowed to update freely within the seabed layer without being penalized, as the regularization weight was set to zero. The intention was to let the inversion ”move” noise and other anomalies located close to the seabed to this seabed layer, instead of contaminating the high-resistive anomaly associated with Pingvin discovery within the reservoir layer. For this type of regularization weight grid model, 1.0 was regarded as the most optimal of the tested background regularization weights.

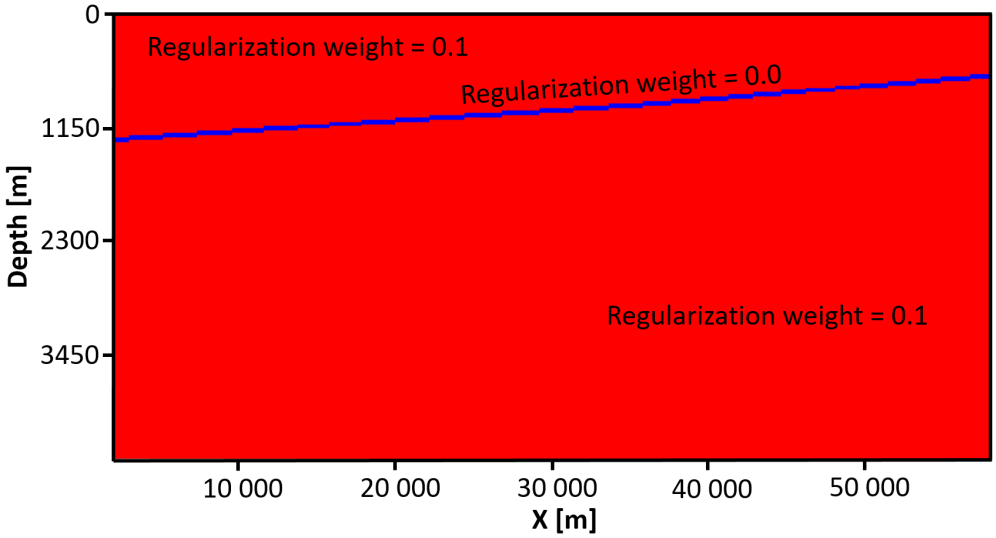

Figure 6.37: *Regularization weight grid model #1. The over- and underburden have been assigned a regularization weight of 0.1 (red), whereas the reservoir layer has been given the value zero (blue). The inversion has been allowed to update freely within the reservoir, but the regularization misfit has been penalized if resistivity changes have been made in the background. 0.1 was selected as the background regularization weight because of more optimal total misfit and minimal noise in the inverted resistivity model, compared to using higher and lower values.*

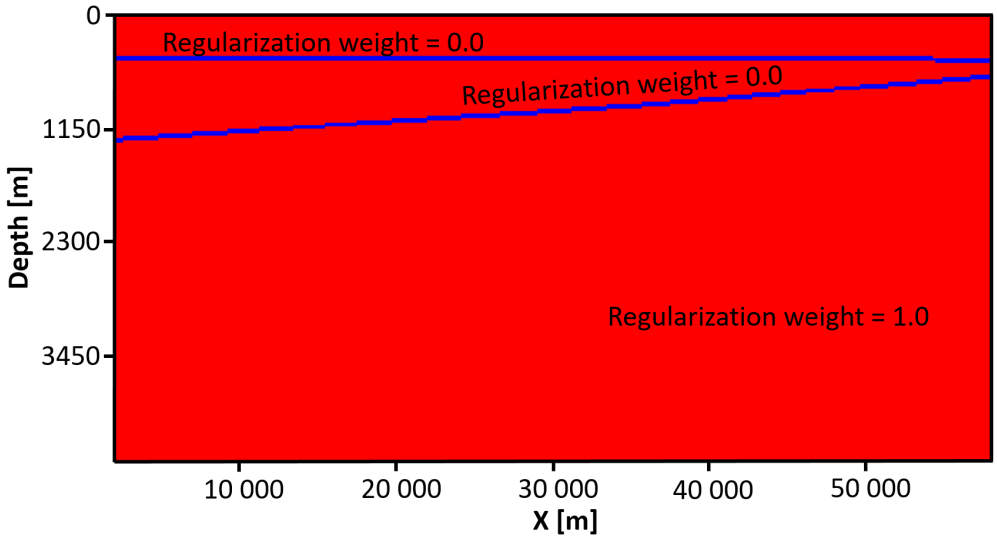

Figure 6.38: *Regularization weight grid model #2. The over- and underburden have been assigned a regularization weight of 1.0 (red), whereas the reservoir layer and the layer below the seabed, both with equal thicknesses, have been given the value zero (blue). The seabed layer was inserted with the intention to "move" noise and other anomalies close to the seabed to this layer, instead of contaminating the Pingvin anomaly within the reservoir layer. The inversion has been allowed to update freely within the reservoir and the seabed layer, but the regularization misfit has been penalized if resistivity changes were made in the background. 1.0 was selected as the background regularization weight because of more optimal total misfit and minimal noise in the inverted model, compared to using higher and lower values.*

6.6.3 Selection of Input Parameters

To increase the spatial resolution, about half the vertical cell size used for unconstrained inversion have been used for constrained inversion, i.e. 23 meters. The horizontal cell size was set to 200 meters. All the frequencies with the highest source signals; 1, 2, 4, 8, 10 and 16 Hz, have proven useful for unconstrained inversion (see Section 6.5.2) and have therefore also been used as input to constrained inversion. The minimum offset was set to 1500 meters for all frequencies, whereas the outer offsets were cut at 8 000 meters for 1 Hz, 8 000 meters for 2 Hz, 8 000 meters for 4 Hz, 5 700 meters for 8 Hz, 4 900 meters for 10 Hz and 3 600 meters for 16 Hz.

6.6.4 Constrained Inversion Results and Uncertainty Evaluation

Inputs discussed in Sections 6.6.1, 6.6.2 and 6.6.3, including the bathymetry map presented in Figure 4.4 have been used to create the final 3D constrained inversion results. 21 inversion jobs have been run to find the most optimal regularization weight grid model. Regardless of the design of the regularization weight grid model, the high-resistive anomaly believed to represent the Pingvin discovery was detected by all the vertical resistivity models. The resistivity values within this anomaly and the abundance of noise did however change. Figure 6.39 shows how different regularization weight grid models have affected the vertical resistivity model and the associated misfit. The type of regularization weight grid model shown in Figure 6.37 was used for the inversion results presented, but with different background regularization weights. For background regularization weights above 0.1, the higher the background regularization weight, the higher the end data misfit for the associated inversion result. Regularization weight grid models with background regularization weights lower than 0.1 provided noisy inversion results.

The two inversion results in Figure 6.40 are presented as the constrained inversion results to be used for qualitative and quantitative interpretation. These models have been chosen because of their data misfits converging towards one for high iterations and because of minimal noise in the vicinity of the high-resistive Pingvin anomaly. The inversions in Figures 6.40(a) and 6.40(b) have been run with regularization weight grid models equal to those presented in Figures 6.37 and 6.38 respectively. The distinct high-resistive anomaly in 6.40(a) has slightly been pulled towards the seabed, indicating that the maximum reservoir resistivity of 873 Ωm observed from the section was too low. With a data uncertainty of 3%, the end data misfit was 2.4% (i.e. below the data uncertainty), indicating that the synthetic data has attempted to fit the measured noise.

Figure 6.41 shows that most of the noise within the seabed layer from the model in Figure 6.40b was related to the receivers, but with one high-resistive anomaly between two receiver lines. This anomaly was located right above the Pingvin anomaly. It was believed that this shallow anomaly is a part of the Pingvin anomaly, indicating that the maximum reservoir resistivity was too low. The maximum resistivity that the inversion was allowed to update for, which was set to 1000 Ωm, was reached for several cells within the Pingvin anomaly. For the same model, the data misfit and regularization misfit

spiked around iteration 150, before the data misfit continued to converge giving an end data misfit of 4.8%.

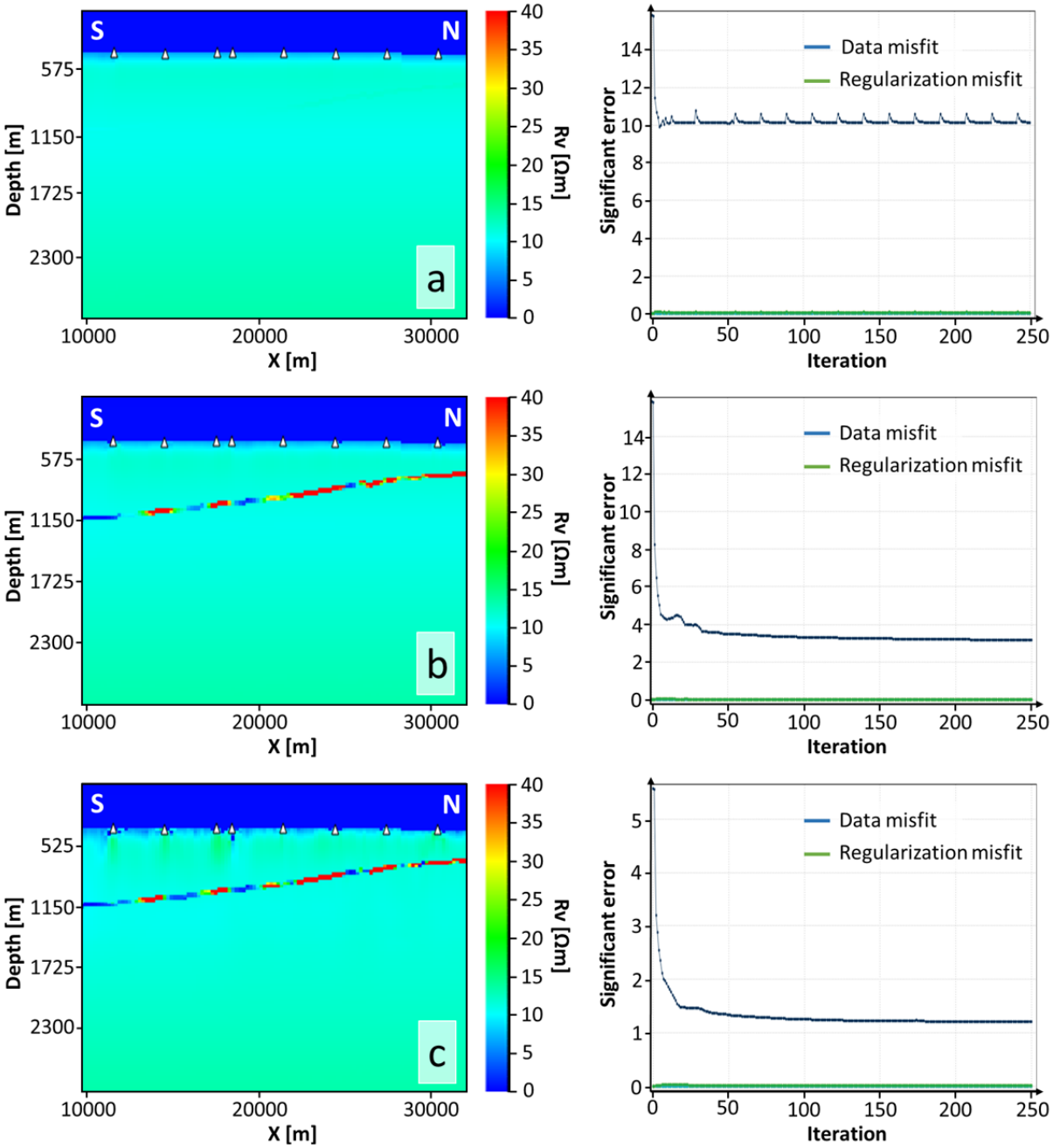

Figure 6.39: *3D constrained inversion results created with different background regularization weights and associated misfit function. The inversions have been run with the type of regularization weight grid model as that presented in Figure 6.37, however with different background regularization weights; 5 in (a), 1 in (b) and 0.5 in (c). The higher the background regularization weight used, the higher the data misfit for the inverted resistivity models.*

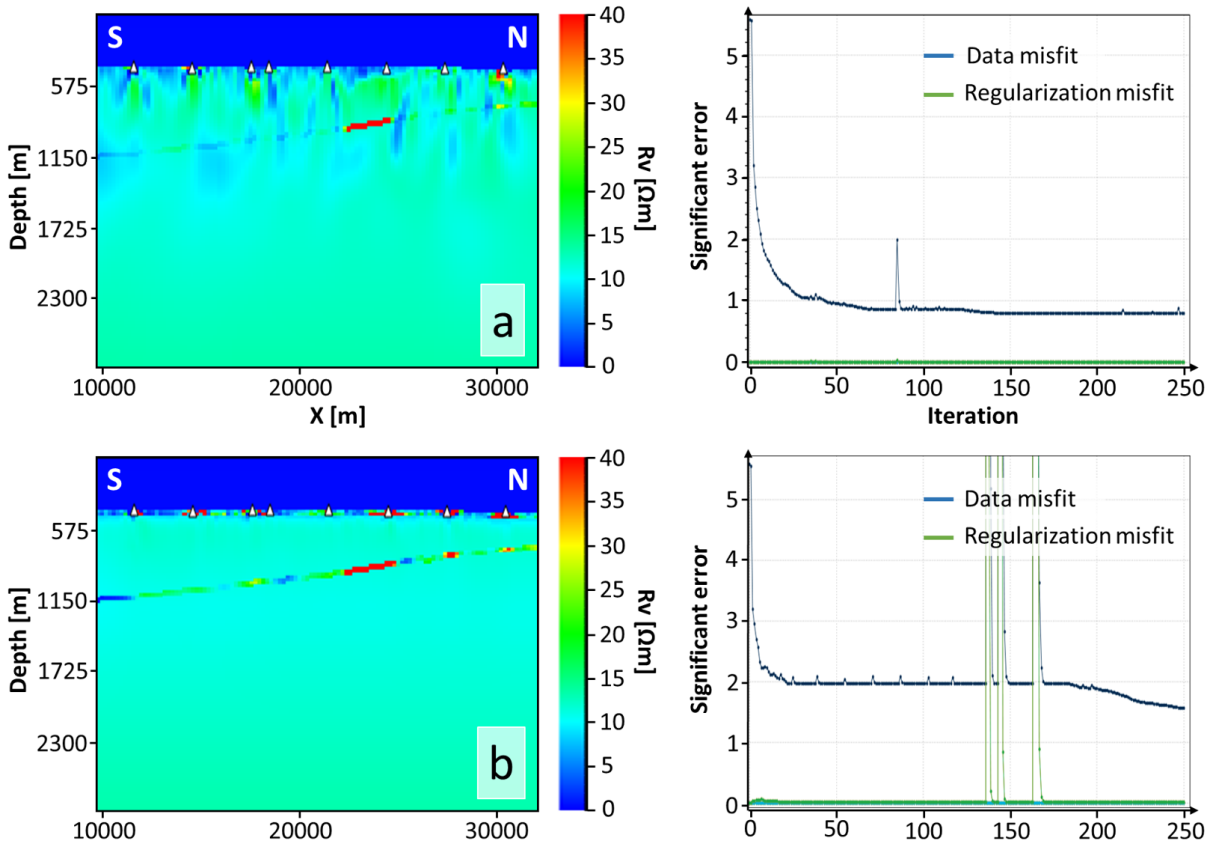

Figure 6.40: *Final 3D constrained inversion results and associated misfit function. The inversions in (a) and (b) have been run with the regularization weight grid models presented in Figures 6.37 and 6.38 respectively. See text for more information. The vertical resistivity models presented are those obtained at iteration 250. The maximum vertical resistivity obtained for the Pingvin anomaly from the section was 873 Ωm for the model in (a). For the model in (b), the maximum resistivity that the inversion was allowed to update for, which was set to 1000 Ωm, was reached for several cells within the anomaly.*

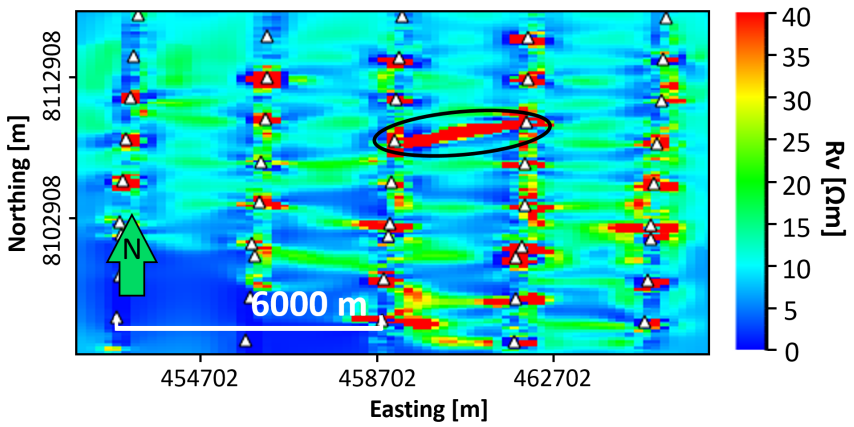

Figure 6.41: *The 3D constrained inversion result presented in Figure 6.40b in map view at 437 meters TVDSS. Most of the high resistive anomalies within the seabed layer, believed to represent noise, were linked with the receivers. The black ellipse shows a high-resistive anomaly believed to be part of the underlying Pingvin anomaly.*

6.7 Quantitative Interpretation

6.7.1 Anomalous Transverse Resistance Maps

The average resistivity map for the reservoir layer created from the vertical resistivity model presented in Figure 6.40a, is shown in Figure 6.42. The associated anomalous transverse resistance (ATR) map in Figure 6.43 has been created with a background resistivity of 12 Ωm and a reservoir layer thickness of 46 meters, corresponding to two times the vertical cell size. The Pingvin anomaly was easily distinguished from the background areas for both the average resistivity map and the ATR map. From Figure 6.42, the anomaly is seen to be divided into one high-resistive part and one part in the Southwest with lower resistivities. The resistivity and ATR at the well location were equal to the background values. The average resistivity map and the ATR map associated with the inverted resistivity model in Figure 6.40b are presented in Figures 6.44 and 6.45 respectively. The ATR map has been created with a background resistivity of 12 Ωm and a reservoir layer thickness of 46 meters. These two maps were heavily contaminated by noise. Based on the presence of noise, the strange behaviour of the misfit function (see Figure 6.40b) and the high-resistive anomaly within the seabed layer believed to be a part of the Pingvin anomaly (see Figure 6.41), it was decided to discard this resistivity model to be used for quantitative analysis of the reservoir.

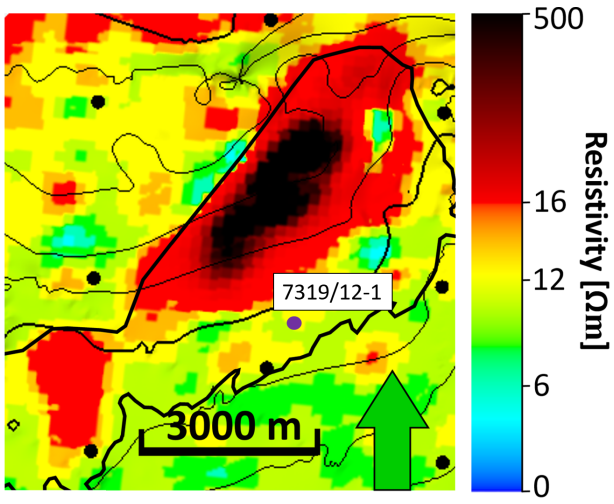

Figure 6.42: *Average resistivity map for the reservoir layer, with anomalous resistivities presented in red to black. The map has been created from the vertical resistivity model presented in Figure 6.40a. The Pingvin anomaly, which consisted of one high-resistive part and one lower resistive part in the Southwest, was easily distinguished from the background. In terms of color scale, resistivities under 16 Ωm have been associated with the background resistivities and resistivities over 16 Ωm have been associated with anomalous resistivity values. The black dots represent the locations of the CSEM receivers and the purple dot shows the well location. The seismically derived prospect outline (black) has been downloaded from (Norwegian Petroleum Directorate, nde).*

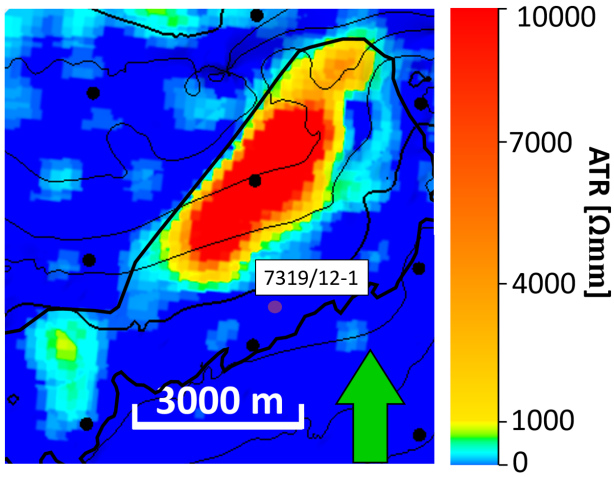

Figure 6.43: *Anomalous transverse resistance (ATR) map associated with the resistivity model in Figure 6.40a. The map has been created by utilizing Equation 3.3, the average resistivity map in Figure 6.42 as the target resistivity, a background resistivity of 12 Ωm and a reservoir layer thickness of 46 meters. In terms of color scale, ATR values under 1000 Ωmm have been associated with the background ATR values and ATR values over 1000 Ωm have been associated with anomalous ATR values. The black dots represent the locations of the CSEM receivers and the purple dot shows the well location. The seismically derived prospect outline (black) has been downloaded from (Norwegian Petroleum Directorate, nde).*

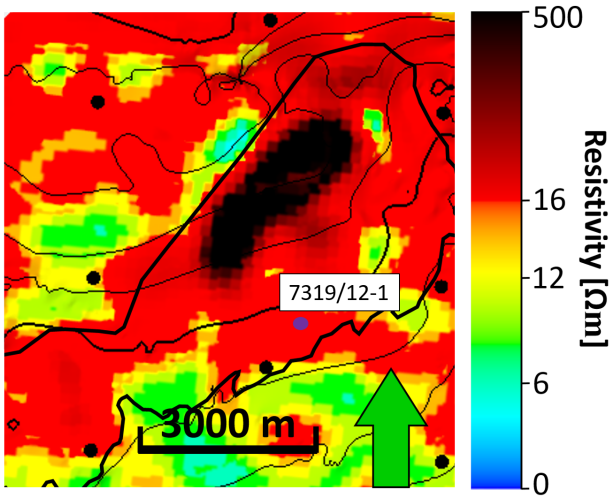

Figure 6.44: *Average resistivity map for the reservoir layer, with anomalous resistivities presented in red to black. The map has been created from the vertical resistivity model presented in Figure 6.40b. The map was contaminated by noise, complicating the process of distinguishing the Pingvin anomaly from the background. In terms of color scale, resistivities under 16 Ωm have been associated with the background resistivities and resistivities over 16 Ωm have been associated with anomalous resistivity values. The black dots represent the locations of the CSEM receivers and the purple dot shows the well location. The seismically derived prospect outline (black) has been downloaded from (Norwegian Petroleum Directorate, nde).*

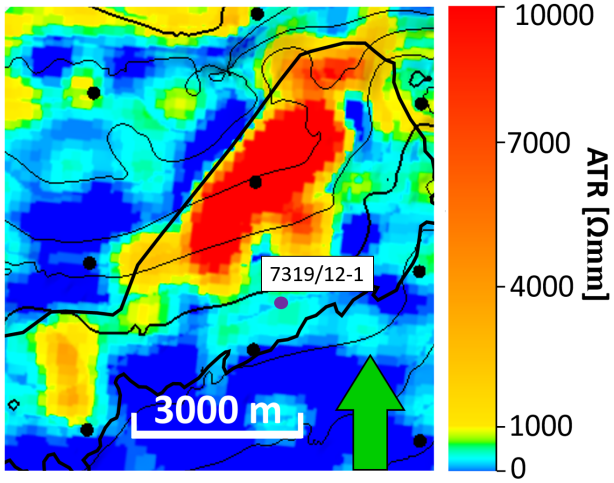

Figure 6.45: *Anomalous transverse resistance (ATR) map associated with the resistivity model in Figure 6.40b. The map has been created by utilizing Equation 3.3, the average resistivity map in Figure 6.44 as the target resistivity, a background resistivity of 12 Ωm and a reservoir layer thickness of 46 meters. In terms of color scale, ATR values under 1000 Ωmm have been associated with the background ATR values and ATR values over 1000 Ωm have been associated with anomalous ATR values. The black dots represent the locations of the CSEM receivers and the purple dot shows the well location. The seismically derived prospect outline (black) has been downloaded from (Norwegian Petroleum Directorate, nde).*

6.7.2 Upscaling of Well Data

The upscaled vertical resistivity and the upscaled water saturation values from the sandstone reservoir are presented in Figures 6.46 and 6.47 respectively. The resolution of the petrophysical data has been lowered through upscaling, but the upscaled values have shown the same trends as the original well data. The figures show that the highest vertical resistivities have been attained within the same depth range as the lowest values for water saturation.

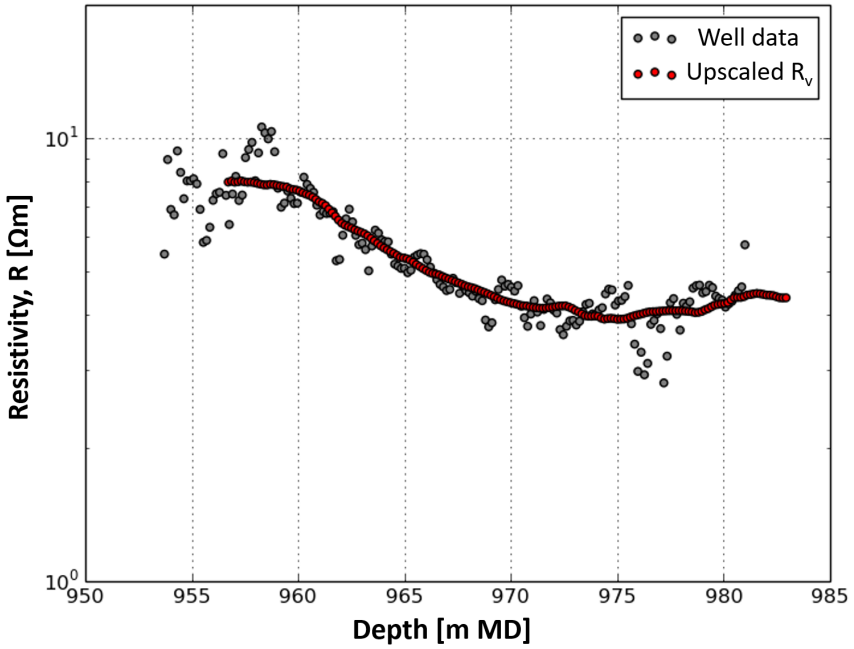

Figure 6.46: *Deep horizontal resistivity measurements from well data and the upscaled vertical resistivity values as functions of measured depth. The upscaled values show the same trend as the original well data, however with lowered resolution.*

6.7.3 Rock Physics Modeling

The relationship between the upscaled vertical resistivity and the upscaled water saturation is shown in Figure 6.48. The highest gas saturation encountered in the wellbore was 61% and no resistivity values for high gas saturations have been available. The curve was for that reason fitted to the upscaled data points and extrapolated for high gas saturations. The scale parameter linked to the radius of the pore throats, l, was set to 5. This relationship was considered as not being physically meaningful, as high resistivities were

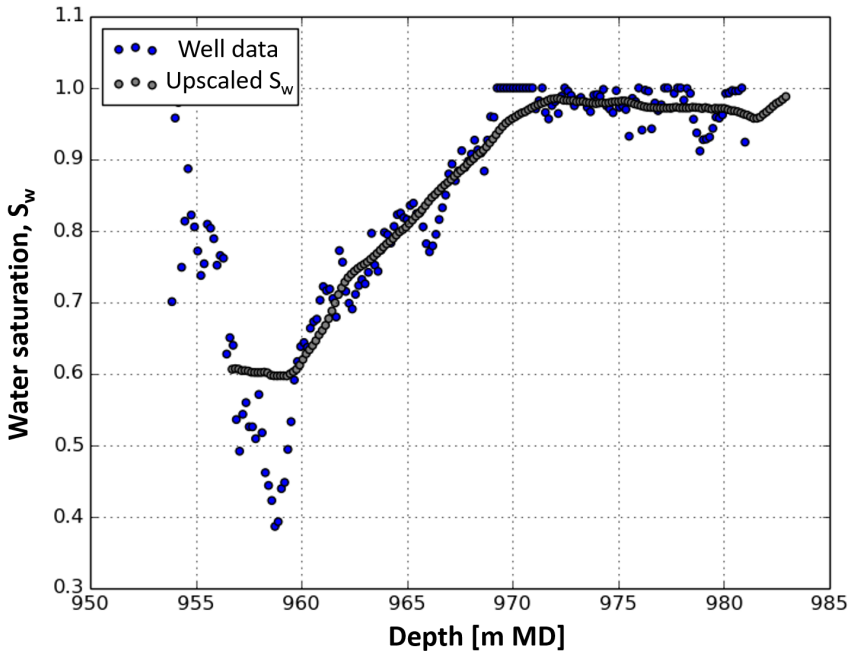

Figure 6.47: *Water saturation estimated from the modified Simandoux equation and upscaled water saturation values as functions of measured depth. The upscaled values show the same trend as the original well data, however with lowered resolution.*

never reached. A synthetic resistivity data point created from the modified Simandoux equation was therefore created for an assumed irreducible water saturation of 0.08. The same values were used for the constants in the modified Simandoux equation as those used to calculate effective water saturation through petrophysical analysis (see Section 6.4.5). Average values for the bulk volume fraction of shale and the effective porosity within the sandstone reservoir zone, 0.3861 and 0.1901 respectively, have been used as input. The calibrated curve, the guided extrapolated curve, created and shown in Figure 6.48, fitted with the upscaled well data and the synthetic data point at the assumed irreducible water saturation. The obtained constants in Equation 5.13 were; a = 4.0201, b = 1.4343 and c = 2.6331e-03. To create this relationship between vertical resistivity and water saturation, the irreducible water saturation in Equation 5.14 was set to 0.08 and l, the scale parameter, was set to 5.

The Archie relationship between the upscaled vertical resistivity and water saturation has been created by using the same constant values as those used to estimate the total water saturation in the well through petrophysical analysis (see Section 6.4.5). The scale parameter l was set to 2, which is smaller than 5, because the pore throats are most likely

larger for a clean formation than for the shaly sandstone encountered by the well. The Archie curve, which is presented in Figure 6.48, shows approximately the same trend as the Simandoux relationship, but with higher resistivities for each water saturation value under 0.75.

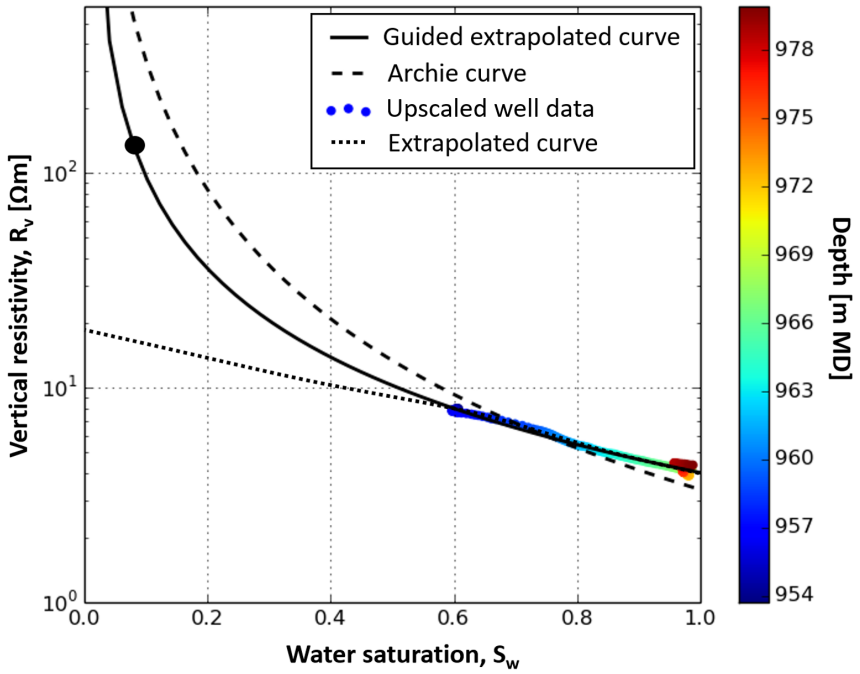

Figure 6.48: *Relationships between upscaled vertical resistivity (R_v) and water saturation (S_w). The curve named "extrapolated curve" has been fitted to the upscaled well data and extrapolated for high gas saturations. A synthetic data point has been created at the assumed irreducible water saturation of 0.08 by using the modified Simandoux equation. The "guided extrapolated curve", which is based on a Simandoux model, has been determined to fit with the upscaled well data and intersect this synthetic data point. The "Archie curve" has been created exclusively by the use of the Archie equation and with the same constant parameters used to create the synthetic modified Simandoux data point. The upscaled well data is a function of measured depth.*

The relationships between anomalous transverse resistance and gross pay have been created by integrating the upscaled vertical resistivity from the gas-water contact at 969 meters MD. The obtained anomalous transverse resistance–gross pay relationship based on the well data, the relationship based on the well data *and* the modified Simandoux equation and the relationship based on the Archie equation are plotted in Figure 6.49. The associated data files are given in Appendix B.

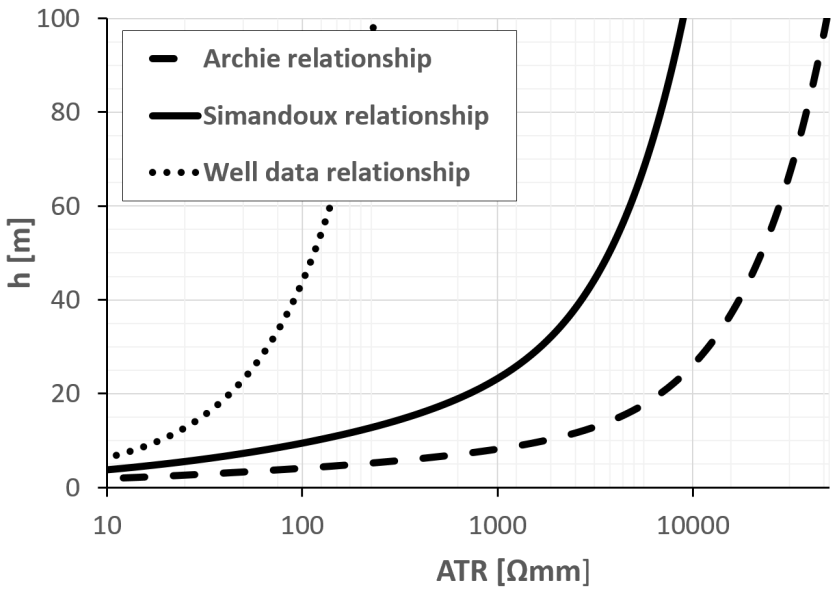

Figure 6.49: *Relationships between anomalous transverse resistance (ATR) and gross pay (h). The curves have been created from the curves in Figure 6.48 of equal dash type. The relationship created based on the Archie equation showed a better quality reservoir than that based on well data and that based on well data and the modified Simandoux equation.*

Gross Pay Maps

The gross pay maps have been created from the ATR map presented in Figure 6.43 and the relationships between ATR and gross pay presented in Figure 6.49.

The gross pay map associated with the relationship between ATR and gross pay based on well data is presented in Figure 6.50. The gross pay map in Figure 6.51 was created from the Simandoux relationship and the gross pay map in Figure 6.52 was created from the Archie relationship. Significantly lower gross pay values have been obtained from the Archie gross pay map than for the map based on the well data.

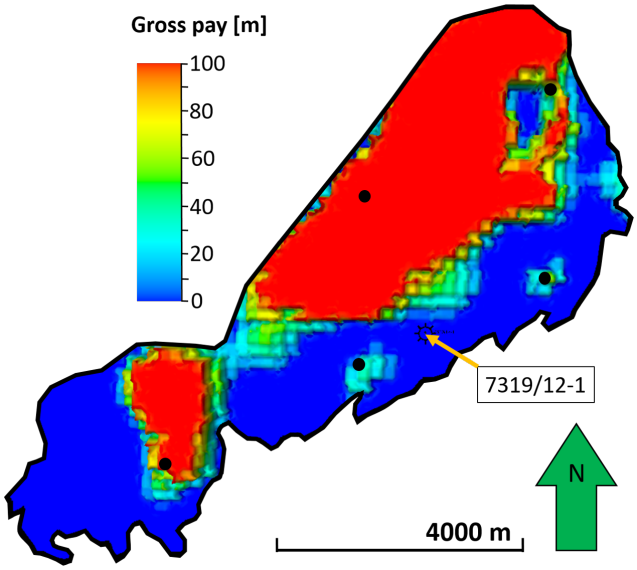

Figure 6.50: *Gross pay map created from the relationship between upscaled vertical resistivity and water saturation based on well data and the anomalous transverse resistance map presented in Figure 6.43. Gross pays over 100 meters have been obtained in large parts within the seismically derived prospect outline downloaded from (Norwegian Petroleum Directorate, nde). The black dots show the locations of the CSEM receivers. The location of well 7319/12-1 is indicated.*

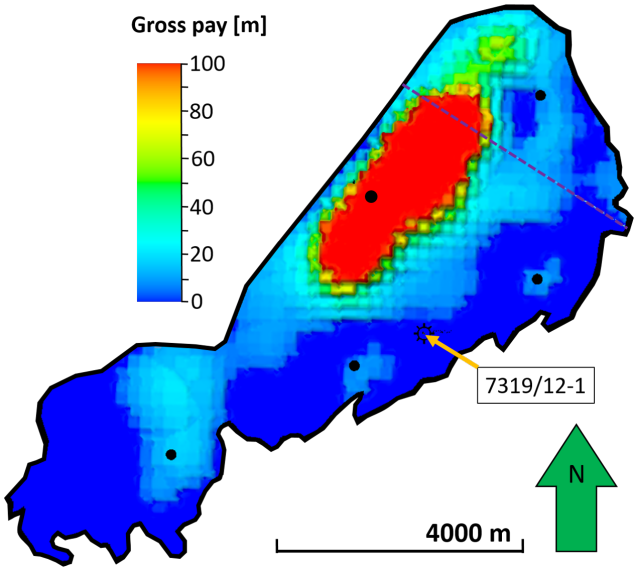

Figure 6.51: *Gross pay map created from the relationship between upscaled vertical resistivity and water saturation based on well data and the modified Simandoux equation and the anomalous transverse resistance map presented in Figure 6.43. Gross pays of over 100 meters have been obtained within the seismically derived prospect outline downloaded from (Norwegian Petroleum Directorate, nde). The dashed purple line shows the intersection of seismic line NH 412-A (see Figure 4.1). The black dots show the locations of the CSEM receivers. The location of well 7319/12-1 is indicated.*

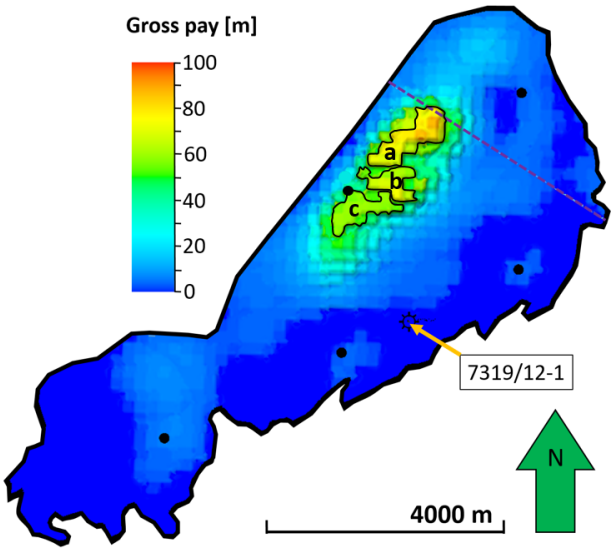

Figure 6.52: *Gross pay map created from the relationship between upscaled vertical resistivity and water saturation based on the Archie equation and the anomalous transverse resistance map presented in Figure 6.43. The maximum reservoir thickness obtained was 92 meters. The thickness "anomaly" has been divided into three distinct parts labeled a, b and c. The map is bounded by the seismically derived prospect outline downloaded from (Norwegian Petroleum Directorate, nde). The dashed purple line shows the intersection of seismic line NH 412-A (see Figure 4.1). The black dots show the locations of the CSEM receivers. The location of well 7319/12-1 is indicated.*

Chapter 7

Integrated Interpretation and Discussion

7.1 Evaluation of Inversion Results

Figures 7.1b and 7.2b show that the high-resistive anomaly obtained from constrained inversion matched well with the high-amplitude seismic anomaly associated with the Pingvin discovery, both laterally and vertically. From the final unconstrained vertical resistivity model in Figure 7.1a, the high-resistive anomaly was positioned some hundred meters above the seismic anomaly. This high-resistive anomaly was more smeared out and lower resistivities were observed compared to the constrained CSEM anomaly. A larger target response was obtained at the thicker updip part of the seismic anomaly than from the thinner part towards the Southeast. The vertical average resistivity map in Figure 7.2a shows how the unconstrained CSEM anomaly coincided with the seismically derived prospect outline. The high-resistive constrained anomaly has been focused within the updip part of the seismic anomaly, whereas no CSEM anomaly was exhibited from the thinner part. As the thickness of the anomaly was decreased compared to the thickness of the unconstrained high-resistive anomaly by constraining the inversion, the target resistivities increased. As explained in Section 3.1.6, this was expected since the CSEM method is sensitive to the difference in resistivity between the target and the background *and* to the target thickness, combined referred to as anomalous transverse resistance (ATR). From the average vertical resistivity maps, the CSEM anomaly was seen to be divided

into one high-resistive part and one part in the Southwest with lower resistivities. The lower-resistive part was most pronounced for the constrained model.

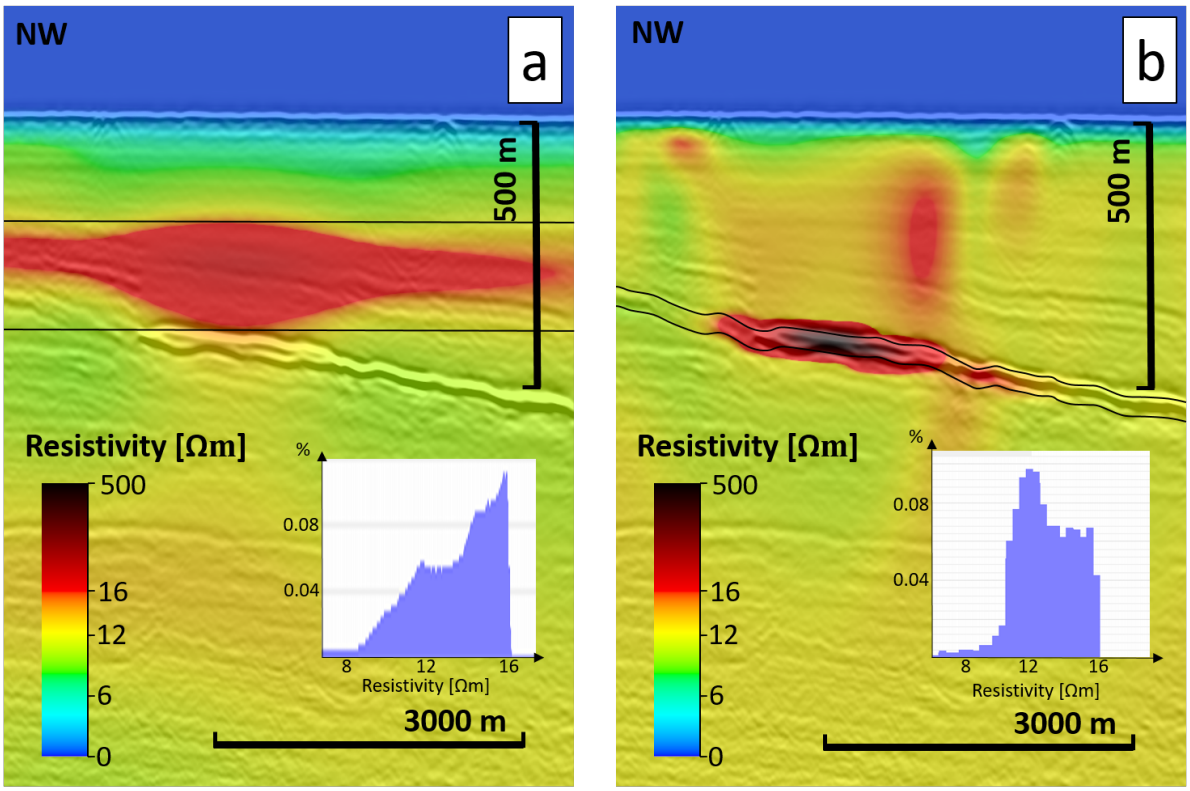

Figure 7.1: *(a) Unconstrained and (b) constrained vertical resistivity model compared with the seismic section NH 412-A (see Figure 4.1). The high-resistive anomaly obtained from unconstrained inversion has been characterized by unrealistic thicknesses and has been positioned some hundred meters shallower than the high-amplitude seismic anomaly. The energy has been focused at the thicker updip part of the seismic anomaly for the unconstrained and the constrained inversion, whereas no constrained CSEM anomaly was observed at the thinner part. The black lines represent the surfaces bounding the anomalies. The color scale has been chosen similar for both the models and has been based on the resistivity contents visualized in histograms. Resistivities under 16 Ωm have been associated with the background resistivities and resistivities over 16 Ωm have been associated with anomalous resistivity values.*

Figure 7.3 shows the horizontal and vertical resistivity curves extracted from the unconstrained and constrained resistivity models at the well location and compared with the deep resistivity measurement from the wireline logging. Approximately equal horizontal resistivity values have been obtained from the deep resistivity wireline measurement and from both the resistivity models. As it was the horizontal resistivity that was measured by the tool in the well, only the horizontal curves from the inversion results were directly

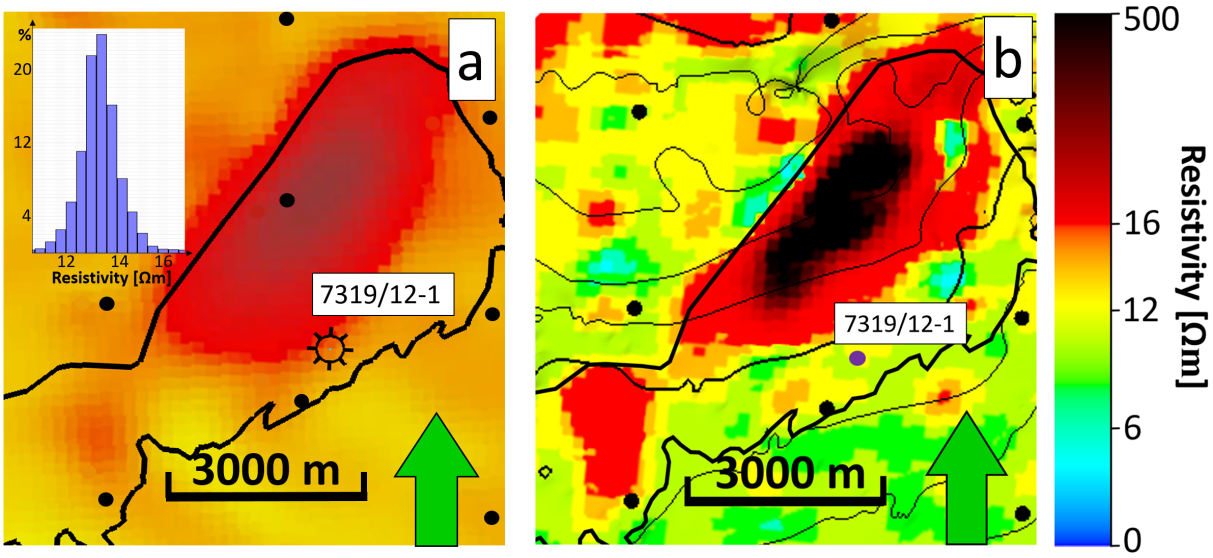

Figure 7.2: *Average vertical resistivity maps from (a) unconstrained and (b) constrained inversion. The map in (a) is associated with the resistivity model in Figure 7.1a and the map in (b) is associated with the resistivity model in Figure 7.1b. The unconstrained average resistivity map has been created by averaging the resistivities between two horizontal surfaces bounding the CSEM anomaly; one at 560 meters and the other at 760 meters TVDSS (see Figure 7.1a). The constrained average resistivity map has been created by averaging the resistivities between the top reservoir surface interpreted from seismic data and a surface of equal shape positioned 46 meters deeper (see Figure 7.1b). Both the high-amplitude anomalies matched well with the northern part of the seismically derived prospect outline (downloaded from Norwegian Petroleum Directorate (nde)). The color scale has been chosen similar for both the models and has been based on the resistivity contents illustrated in histograms. Resistivities under 16 Ωm have been associated with the background resistivities and resistivities over 16 Ωm have been associated with anomalous resistivity values. The black dots represent the locations of the CSEM receivers.*

comparable with the well log readings. A peak vertical resistivity of 11 Ωm was observed at 680 meters TVDSS from the log extracted from the unconstrained resistivity model, whereas the vertical resistivity curve from the constrained resistivity model showed constant values with depth. This is supported by the observation that the well has been drilled at the edge of the unconstrained CSEM anomaly and outside the constrained CSEM anomaly (see Figure 7.2). The vertical resistivity (see Figure 7.2b) and ATR (see Figure 6.43) values from the constrained resistivity model at the well location were equal to the background values, indicating that 16 meters of gas with an average gas saturation of 27% is below the CSEM resolution. Based on the location of the high-resistive Pingvin anomalies obtained from unconstrained and constrained inversion, it has been interpreted that there are higher gas saturations at the updip part of the seismic anomaly than what was encountered by the well.

Regularization has been the input parameter having influenced the inversion results the most. Applying inadequate regularization, varying degrees of noise were introduced to the resistivity model, contaminating the target response. The noise in the overburden in Figure 7.1b is for example believed to be linked to the regularization strength applied. The constrained inversion results showed the same background resistivity trends as the a priori model because the misfit was punished if changes in terms of resistivity in the background were made. It was however promising that similar background resistivity trends were recovered by the unconstrained inversion, indicating that the a priori model has provided resistivities close to the true subsurface resistivities.

Trusting the constrained inversion results required that the seismically interpreted top reservoir surface and the seismic depth conversion were trusted. The depth of the continuous, high-amplitude seismic horizon associated with the top reservoir matched well with the depth of the top reservoir encountered by the well. There has been no reason not to trust the constrained inversion results.

From the study performed by Fanavoll et al. (2014a), the unconstrained high-resistive anomaly coincided with the thicker updip part of the high-amplitude seismic anomaly, whereas the thinner part exhibited no CSEM anomaly. These observations correspond with the unconstrained results obtained from this study, increasing the confidence in the resistivity models obtained.

7.2 Interpretation of Reservoir Quality

The Pingvin reservoir quality has been evaluated by comparing the Simandoux gross pay map in Figure 6.51 and the Archie gross pay map in Figure 6.52 with the reservoir thickness interpreted from the 2D seismic line NH 412-A (see Figure 4.1 for location). The gross pay map created based on well data (see Figure 6.50) has been discarded because of the associated unrealistic relationship between upscaled vertical resistivity and water saturation presented in Figure 6.48. Figure 7.4 shows the gross pay from the Simandoux and Archie maps and the reservoir thickness interpreted from seismic data along the seismic line NH 412-A. Data only along the part of the seismic section showing the distinct seismic Pingvin anomaly is presented. The curves representing gross pay showed an overall match with the curve representing the seismic reservoir thickness. Significant gross pays

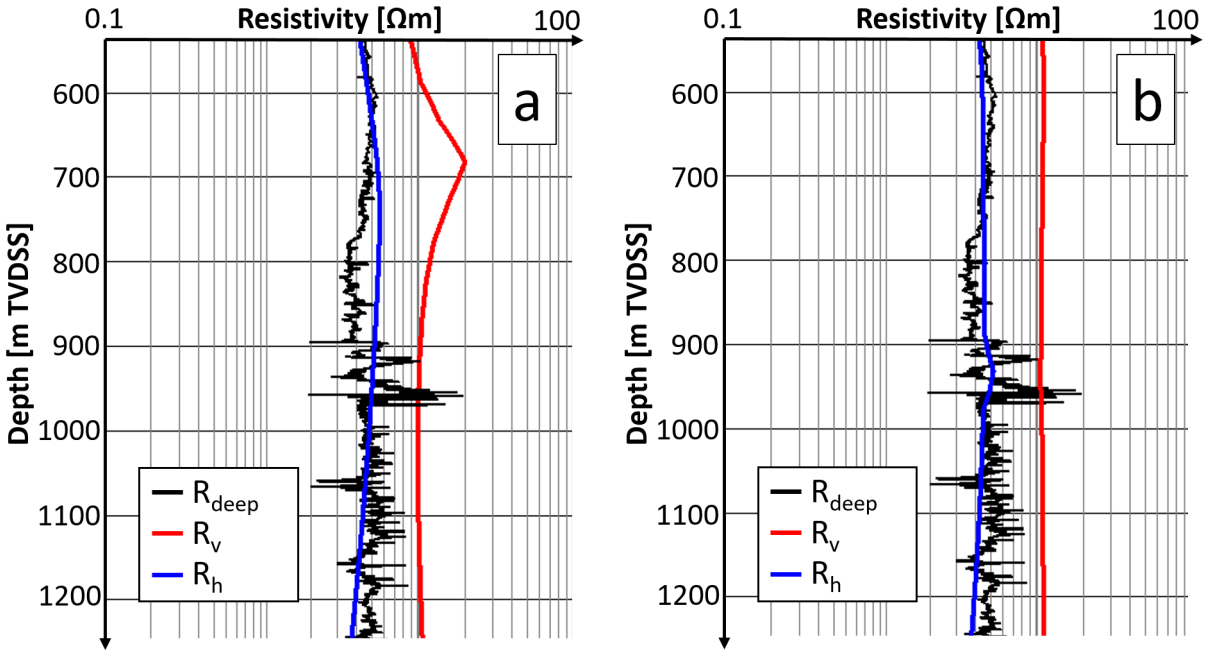

Figure 7.3: *The deep resistivity measured from wireline logging compared with the vertical and the horizontal resistivity curves extracted from inversion results at the well location. The curves in (a) have been extracted from the final unconstrained resistivity model and the curves in (b) have been extracted from the final constrained resistivity model. The deep resistivity curve, representing the measured horizontal resistivity component, coincided with the horizontal resistivities obtained from the CSEM inversions. A peak vertical resistivity of 11 Ωm can be observed at 680 meters depth in (a). The vertical resistivity curve from the constrained resistivity model has shown constant values with depth.*

have been obtained only in the updip part of the seismic anomaly associated with the Pingvin discovery. Low to no gross pay has been observed towards the Southeast in the thinner part of the seismic anomaly. Notice that the thickness derived from the seismic data is the thickness of the reservoir rock, whereas the gross pay represents the thickness of the gas-saturated reservoir rock. The seismic thickness should therefore be larger or equal to the thickness from the gross pay maps in all positions. The seismic reservoir thickness ranged approximately from 15 meters to 45 meters. The Simandoux gross pay curve showed values up to 100 meters in the updip part of the seismic anomaly. Such large thicknesses have been considered as unrealistic compared to the seismic reservoir thicknesses. For the creation of the Simandoux gross pay map, it was assumed that the reservoir rock encountered by the well was representative for the entire reservoir. This model, created from petrophysical data from the well location, has been considered as not being representative for the reservoir rock in this upper part of the seismic anomaly.

The Archie gross pay map showed thicknesses closer to the seismic thicknesses in the updip part of the seismic anomaly than those obtained from the Simandoux gross pay map. This has been interpreted as indication of improved reservoir quality from the well location and towards the updip part of the seismic anomaly, i.e. towards the North, as the Archie model assumes a clean formation. With improved reservoir quality means higher permeability, net-to-gross ratio and/or lower clay content. Keep in mind that changing the parameters a, m and n in the Archie equation (see Equation 3.1), can have large effects on the Archie gross pay calculation. Towards the Southeast along seismic section NH 412-A, the Simandoux gross pay was closer to the seismic reservoir thickness than the Archie gross pay, indicating that the reservoir quality in the thinner part of the seismic anomaly was closer to the reservoir quality encountered by the well than a clean sandstone formation.

The Archie gross pay curve peaked at about seismic inline position 365, whereas the seismic thickness decreased. Receiver noise was the suspected cause of the spiking gross pay, but no CSEM receiver was located in this position. It has been interpreted that neither the Archie model, nor the Simandoux model is representative for the reservoir rock and fluid in this position.

Looking closely at the Archie gross pay map in Figure 6.52, the thickness "anomaly" seemed to be divided into three distinct parts. The pattern identified within the thickness "anomaly" with increasing thickness from c to a, can possibly be linked to internal reservoir structures. Additional information, preferably from 3D seismic data, can be used to support or contradict this interpretation. Access to 3D seismic data would be preferred also for better geological understanding of the basin and for obtaining a more detailed top reservoir surface used as input to the constrained inversion.

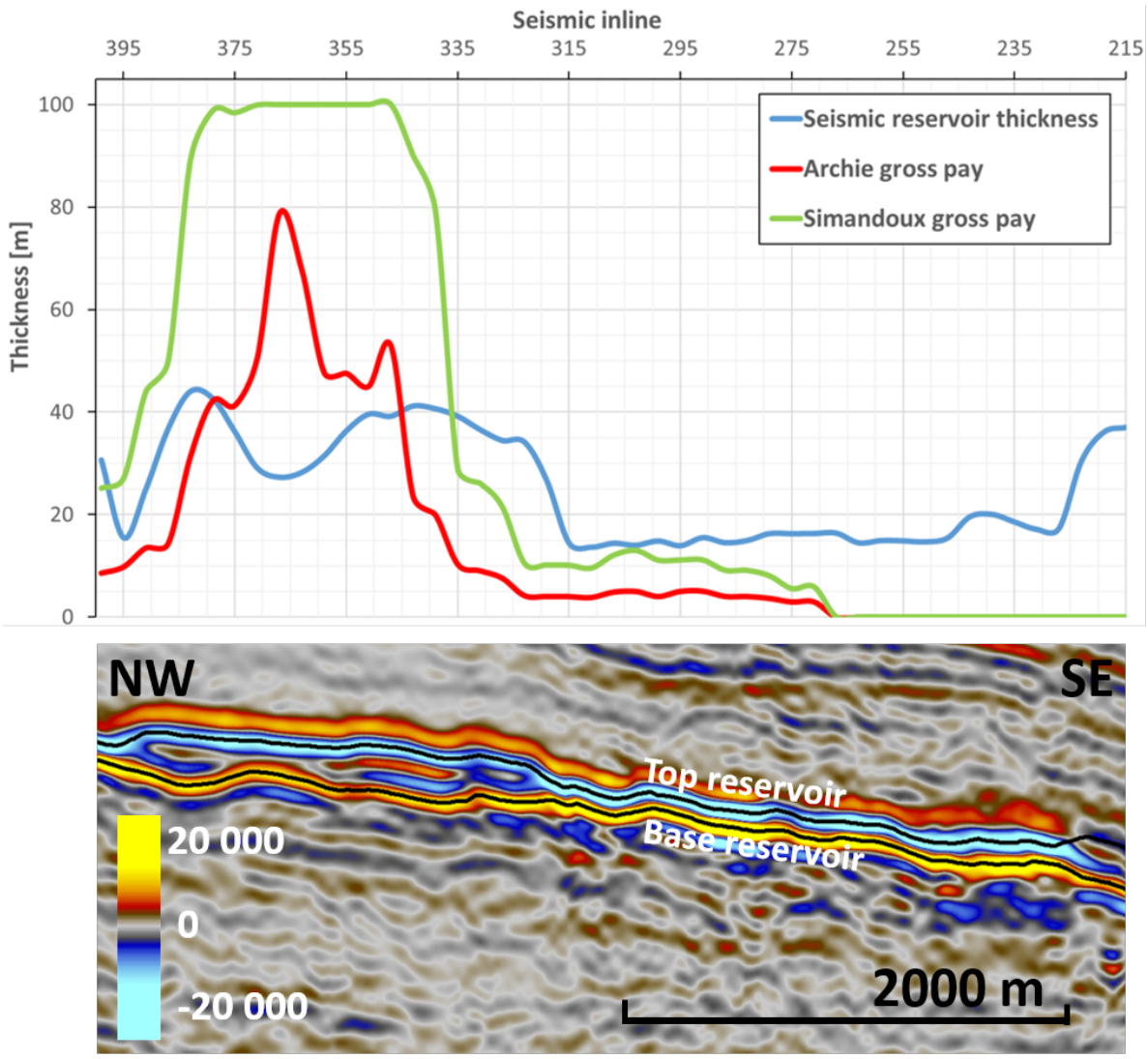

Figure 7.4: *Simandoux gross pay from Figure 6.51 and Archie gross pay from Figure 6.52 compared with the interpreted seismic reservoir thickness. The thicknesses represented through the curves have been extracted along the seismic line NH 412-A (see Figure 4.1 for location). This line is shown in both the gross pay maps. The interpreted seismic horizons representing the top and the base reservoir are shown together with the depth converted seismic section. Significant gross pays have been obtained only in the updip part of the seismic anomaly associated with the Pingvin discovery. The Archie gross pay is closer to the seismic reservoir thickness curve between the seismic inline positions 340 and 380 compared to the Simandoux gross pay. The Simandoux gross pay is closer to the seismic reservoir thickness curve for the seismic inline positions between 265 and 340 compared to the Archie gross pay. The increase in seismic reservoir thickness at seismic inline position 220 is caused by inaccurate seismic interpretation.*

Chapter 8

Conclusion

An innovative method of combining CSEM data with seismic and petrophysical data for qualitative and quantitative reservoir interpretation has been presented in this study. From the work performed, the following conclusions were made:

- The Pingvin discovery has been identified as a shallow stratigraphic trap. It has been interpreted that the reservoir has likely been deposited as part of a prograding fan with sediments originating from the Northeast or East of the Bjørnøya Basin.
- The seismic velocity model created is believed to be representative of the true subsurface velocity distribution between the seabed and the reservoir.
- From the petrophysical analysis, the Pingvin reservoir has been described as a shaly sandstone reservoir with mica minerals. A 16-meter gas column has been identified between the top reservoir at 913 meters TVDSS and the gas-water contact at 929 meters TVDSS. The average effective gas saturation was estimated to 27% within the gas zone with a maximum gas saturation of 61% at 918 meters TVDSS.
- Thorough evaluation of input parameters for unconstrained and constrained CSEM inversions has proven essential for obtaining a resistivity model representative of the true subsurface resistivity trends. Regularization was the parameter influencing the inversion results the most. Creating a precise a priori model for constrained inversion, representative of the background resistivity trends, has also been important.
- The high-resistive shallow anomaly associated with the Pingvin discovery has been detected by all the inverted resistivity models, regardless of inputs to the inversion.

- The high-resistive anomaly obtained from unconstrained inversion coincided with the location of the seismic anomaly, however positioned some hundred meters too shallow.
- This high-resistive anomaly has successfully been focused below the top reservoir surface interpreted from the 2D seismic data by performing constrained inversion. The high-resistive constrained Pingvin anomaly matched well with the updip part of the seismic anomaly, both laterally and in depth.
- Results have shown that higher gas saturations are likely to be encountered at the updip part of the seismic anomaly than what was estimated from the well data.
- It has been proven that it is useful to consider anomalous transverse resistance for evaluation of high-resistive CSEM anomalies associated with hydrocarbon accumulations.
- It has been interpreted that the reservoir quality improves from the well location towards the updip part of the seismic anomaly and the stratigraphic trap.
- A distinct pattern has been identified from the Archie gross pay map, possibly linked to internal reservoir structures.

Chapter 9

Recommendations for Further Work

The work presented in this study has been performed with limited time. In order to fully utilize the potential of the workflow shown in Figure 5.18, it is recommended to more thoroughly evaluate and interpret the input data for more effective and precise data integration. For further work, the following should be considered:

- It is recommended to expand the project by integrating 3D seismic data for increased confidence in the seismic interpretation. 3D seismic data can also be useful for investigating whether the pattern within the Archie gross pay "anomaly" can be linked with internal reservoir structures.
- Amplitude versus offset (AVO) analysis should be performed for additional information on reservoir rock properties and pore fluid.
- Input parameters used to estimate water saturation through petrophysical analysis should be more thoroughly evaluated. Uncertainties have especially been associated with the lithology coefficient, cementation exponent and saturation exponent, as standard values have been used. These rock properties should be tuned by matching well data with information from core samples and core photos.
- Reservoir quality at the well location should be evaluated by investigating the relationship between porosity and permeability from the well data.
- More regularization weight grid models should be considered for constrained inversion because regularization has proven to greatly influence the CSEM inversion results.

- Additional relationships between upscaled vertical resistivity and water saturation should be established and considered for more accurate interpretation of reservoir quality.
- Different relationships between anomalous transverse resistance and gross pay should be evaluated in terms of changing the scale parameter l in Equation 5.14.
- The well encountered relatively low saturations of gas and the value for the irreducible water saturation was therefore presumed rather than extracted from the well data. It is recommended to estimate the irreducible water saturation from well data from wells in the Southwestern Barents Sea penetrating reservoirs similar to the Pingvin reservoir, however with high saturations of gas.

References

Al-Ruwaili, S. B. and Al-Waheed, H. H. (2004). Improved Petrophysical Methods and Techniques for Shaly Sands Evaluation. 2004 SPE International Petroleum Conference in Mexico.

Allen, D., Crary, S., Freedman, B., Andreani, M., Klopf, W., Badry, R., Flaum, C., Kenyon, B., Kleinberg, R., Gossenberg, P., Horkowitz, J., Logan, D., Singer, J., and White, J. (1997). How to Use Borehole Nuclear Magnetic Resonance. *Oilfield Review*, 9(2):34–57.

Alvarez, P., Alvarez, A., MacGregor, L., Bolivar, F., Keirstead, R., and Martin, T. (2017). Reservoir properties prediction integrating controlled-source electromagnetic, prestack seismic, and well-log data using a rock-physics framework: Case study in the Hoop Area, Barents Sea, Norway. *Interpretation*, 5(2):SE43–SE60.

Archie, G. (1942). The Electrical Resistivity Log as an Aid in Determining Some Reservoir Characteristics. *Petroleum Technology*, 146(1):54–62.

Avseth, P., Mukerji, T., and Mavko, G. (2005). *Quantitative Seismic Interpretation - Applying Rock Physics Tools to Reduce Interpretation Risk*. Cambridge University Press. Chapter 4: Common techniques for quantitative seismic interpretation.

Baig, I., Faleide, J. I., Jahren, J., and Mondol, N. H. (2016). Cenozoic exhumation on the southwestern Barents Shelf: Estimates and uncertainties constrained from compaction and thermal maturity analyses. *Marine and Petroleum Geology*, 73:105–130.

Baltar, D. and Roth, F. (2013). Reserves estimation methods for prospect evaluation with 3D CSEM data. *First Break*, 31(6):103–111.

Bardon, C. and Pied, B. (1969). Formation water saturation in shaly sands. Society of

Professional Well Log Analysts10th Annual Logging Symposium Transactions: Paper Z, 19 pp.

Barker, N. and Baltar, D. (2016). CSEM anomaly identification. *First Break*, 34(4):47–50.

Bhuiyan, A. H., Thrane, B. P., Landrø, M., and Johansen, S. E. (2010). Controlled source electromagnetic three-dimensional grid-modelling based on a complex resistivity structure of the seafloor: effects of acquisition parameters and geometry of multi-layered resistors. *Geophysical Prospecting*, 58(3):505–533.

Bhuiyan, A. H., Vesterås, E., and McKay, A. (2015). Frontier Exploration using a Towed Streamer EM system - Barents Sea Examples. SEG New Orleans Annual Meeting.

Bhuyan, K. and Passey, Q. R. (1994). Clay Estimation From GR and Neutron-Density Porosity Logs. SPWLA 35th Annual Logging Symposium.

Breivik, A., Gudlaugsson, S., and Faleide, J. (1995). Ottar Basin, SW Barents Sea: A major Upper Paleozoic rift basin containing large volumes of deeply buried salt. *Basin Research*, 7(4):299–312.

Breivik, A. J., Faleide, J. I., and Gudlaugsson, S. T. (1998). Southwestern Barents Sea margin: late Mesozoic sedimentary basins and crustal extension. *Tectonophysics*, 293(1-2):21–44.

Breivik, A. J., Mjelde, R., Grogan, P., Shimamurac, H., Muraic, Y., and Nishimurac, Y. (2005). Caledonide development offshore-onshore Svalbard based on ocean bottom seismometer, conventional seismic, and potential field data. *Tectonophysics*, 401(1-2):79–117.

Commer, M. and Newman, G. A. (2008). New advances in three-dimensional controlled-source electromagnetic inversion. *Geophysical Journal International*, 172(2):513–535.

Constable, S. (2010). Ten years of marine CSEM for hydrocarbon exploration. *Geophysics*, 75(5):67–81.

Constable, S., Orange, A., and Key, K. (2015). And the geophysicist replied: "Which model do you want?". *Geophysics*, 80(3):E197–E212.

Constable, S., Parker, R., and Constable, C. (1987). Occams' inversion: A practical algo-

rithm for generating smooth models from electromagnetic sounding data. *Geophysics*, 52(3):289–300.

Constable, S. and Weiss, C. J. (2006). Mapping thin resistors and hydrocarbons with marine EM methods: Insights from 1D modeling. *Geophysics*, 71(2):G43–G51.

Dalland, A., Worsley, D., and Ofstad, K. (1988). NPD bulletin no. 4: A lithostratigraphic scheme for the Mesozoic and Cenozoic succession offshore mid-and northern Norway.

Danielsen, J. and Bekker (2011). The future of marine CSEM. *First Break*, 29(4):77–81.

de Macedoa, I. A., da Silvaa, C. B., de Figueiredoa, J., and Omoboyac, B. (2016). Comparison between deterministic and statistical wavelet estimation methods through predictive deconvolution: Seismic to well tie example from the North Sea. *Journal of Applied Geophysics*, 136:298–314.

Doré, A. G. (1991). The structural foundation and evolution of Mesozoic seaways between Europe and the Arctic Sea. *Palaeogeography Palaeoclimatology Palaeoecology*, 87(1-4):441–492.

Doré, A. G. (1993). Barents Sea Geology, Petroleum Resources and Commercial Potential. *Arctic*, 48(3):207–221.

Doveton, J. H. (2001). All Models Are Wrong, but Some Models Are Useful: "Solving" the Simandoux Equation. From Session J of the International Association for Mathematical Geology Conference, Cancun, Mexico.

Edgar, J. A. and van der Baan, M. (2011). How reliable is statistical wavelet estimation? *Geophysics*, 76(4):V59–V68.

Eidesmo, T., Ellingsrud, S., Kong, F., Westerdahl, H., and Johansen, S. (2002a). Method and apparatus for determining the nature of subterranean reservoirs. Patent application number WO 00/13046, filed Aug. 1998.

Eidesmo, T., Ellingsrud, S., MacGregor, L., Constable, S., Sinha, M., Johansen, S., Westerdahl, H., and Kong, F. (2002b). Remote detection of hydrocarbon filled layers using marine controlled source electromagnetic sounding. EAGE 64th Conference & Exhibition - Florence, Italy.

Eidesmo, T., Ellingsrud, S., MacGregor, L., Constable, S., Sinha, M., Johansen, S., Wes-

terdahl, H., and Kong, F. (2002c). Sea Bed Logging (SBL), a new method for remote and direct identification of hydrocarbon filled layers in deepwater areas. *First Break*, 20(3):144–152.

Ellingsrud, S., Eidesmo, T., Johansen, S., Sinha, M., MacGregor, L., and Constable, S. (2002). Remote sensing of hydrocarbon layers by seabed logging (SBL): Results from a cruise offshore Angola. *The Leading Edge*, 21(10):972–982.

Ellis, D. (2003). Formation Porosity Estimation from Density Logs. *Petrophysics*, 44(5):306–316.

Ellis, D. V. and Singer, J. M. (2007). *Well Logging for Earth Scientists*. Springer, second edition.

Ellis, M., Sinha, M., and Parr, R. (2010). Role of fine-scale layering and grain alignment in the electrical anisotropy of marine sediments. *First Break*, 28(9):49–57.

EMGS (n.d.a). 2.5D inversion of CSEM data. SBLwiz technical appendix.

EMGS (n.d.b). 3D Inversion of EM data. SBLwiz technical appendix.

EMGS (n.d.c). CSEM Inversion Report. SBLwiz 3D CSEM inversion template.

Faleide, J. I., Bjørlykke, K., and Gabrielsen, R. H. (2015). Geology of the Norwegian Continental Shelf. *Petroleum Geoscience: From Sedimentary Environments to Rock Physics - Second Edition*, pages 603–637.

Faleide, J. I., Tsikalas, F., Breivik, A. J., Mjelde, R., Ritzmann, O., Engen, O., Wilson, J., and Eldhol, O. (2008). Structure and evolution of the continental margin off Norway and the Barents Sea. *Episodes*, 31(1):82–91.

Faleide, J. I., Vågnes, E., and Gudlaugsson, S. T. (1993). Late Mesozoic-Cenozoic evolution of the south-western Barents Sea in a regional rift-shear tectonic setting . *Marine and Petroleum Geology*, 10(3):186–214.

Fanavoll, S., Ellingsrud, S., Gabrielsen, P. T., Tharimela, R., and Ridyard, D. (2012). Exploration with the use of EM data in the Barents Sea: the potential and the challenges. *First Break*, 30(4):89–96.

Fanavoll, S., Gabrielsen, P. T., and Ellingsrud, S. (2014a). CSEM as a tool for better

exploration decisions: Case studies from the Barents Sea, Norwegian Continental Shelf. *Interpretation*, 2(3):55–66.

Fanavoll, S., Gabrielsen, P. T., and Ellingsrud, S. (2014b). The impact of CSEM on exploration decisions and seismic: two case studies from the Barents Sea. *First Break*, 32(11):105–110.

Freedman, R., Minh, C. C., and Gubelin, G. (1998). Combining NMR And Density Logs For Petrophysical Analysis In Gas-Bearing Formations. SPWLA 39th Annual Logging Symposium, 26-28 May, Keystone, Colorado.

Gabrielsen, P. T., Abrahamson, P., Panzner, M., Fanavoll, S., and Ellingsrud, S. (2013). Exploring frontier areas using 2D seismic and 3D CSEM data, as exemplified by multi-client data over the Skrugard and Havis discoveries in the Barents Sea. *First Break*, 31(1):63–71.

Gabrielsen, R., Færseth, R., Hamar, R., and Rønnevik, H. (1984). Nomenclature of the main structural features on the Norwegian Continental Shelf north of the 62nd parallel. In: Spencer et. al. (eds.): *Petroleum Geology of the North European margin*. Norwegian Petroleum Society. (Graham and Trotman), 40-60.

Gabrielsen, R. H., Færseth, R. B., Jensen, L. N., Kalheim, J. E., and Riis, F. (1990). NPD Bulletin No. 6: Structural elements of the Norwegian continental shelf. Part I: The Barents Sea Region.

Glover, P. (n.d.). The Spectral Gamma Ray Log. Petrophysics MSc Course Notes, Chapter 12. `http://homepages.see.leeds.ac.uk/~earpwjg/PG_EN/CD%20Contents/GGL-66565%20Petrophysics%20English/Chapter%2012.PDF` [Online: accessed 28 Apr 2017].

Granli, J. R., Veire, H. H., Gabrielsen, P., and Morten, J. P. (2017). Maturing broadband 3D CSEM for improved reservoir property prediction in the Realgrunnen Group at Wisting, Barents Sea. SEG International Exhibition and 87th Annual Meeting, September 2017 Houston, Texas.

Gudlaugsson, S. T., Faleide, J. I., Johansen, S. E., and Breivik, A. J. (1998). Late Palaeozoic structural development of the South-western Barents Sea. *Marine and Petroleum Geology*, 15(1):73–102. Elsevier.

Harris, P., Du, Z., MacGregor, L., Olsen, W., Shu, R., and Cooper, R. (2009). Joint interpretation of seismic and CSEM data using well log constraints: an example from the Luva Field. *First Break*, 27(5):73–81.

Harris, P. and MacGregor, L. (2007). Enhancing the resolution of CSEM inversion using seismic constraints. SEG San Antonio 2007 Annual Meeting.

Harrison, B. and Jing, X. (2001). Saturation Height Methods and Their Impact on Volumetric Hydrocarbon in Place Estimates. SPE Annual Technical Conference.

Hesthammer, J. and Boulaenko, M. (2005). The offshore EM challenge. *First Break*, 23(11):59–66.

Johansen, N. J. (2016). Regional net erosion estimations and implications for seismic AVO signatures in the Western Barents Sea. Master's thesis, Norwegian University of Science and Technology.

Johansen, S., Ostisty, B., Birkeland, O., Fedorovsky, Y., Martirosjan, V., Bruun Christensen, O., Cheredeev, S., Ignatenko, E., and Margulis, L. (1993). *Hydrocarbon Potential in the Barents Sea region: play distribution and potential*. Elsevier. In: Vorren, T.O., Bergsager, E., Dahl-Stamnes, Ø.A., Holter, E., Johansen, B., Lie, E., and Lund, T., eds. *Arctic geology and petroleum potential*. Norwegian Petroleum Society (NPF) Special Publication 2. Amsterdam: Elsevier. 273-320.

Johansen, S., Wicklund, T., and Amundsen, H. (2007). Interpretation example of marine CSEM data. *The Leading Edge*, 26(3):348–354.

Johansen, S. E., Amundsen, H. E., Røsten, T., Ellingsrud, S., Eidesmo, T., and Bhuiyan, A. H. (2005). Subsurface hydrocarbons detected by electromagnetic sounding. *First Break*, 23(3):31–36.

Johansen, S. E., Brauti, K., Fanavoll, S., Amundsen, H., Wicklund, T. A., Danielsen, J., Gabrielsen, P. T., Lorentz, L., Frenkel, M., Dubois, B., Christensen, O., Elshaug, K., and Karlsen, S. A. (2008). How EM survey analysis validates current technology, processing and interpretation methodology. *First Break*, 26(6):83–88.

Johansen, S. E. and Gabrielsen, P. T. (2015). Interpretation of Marine CSEM and Marine MT Data for Hydrocarbon Prospecting. *Petroleum Geoscience: From Sedimentary Environments to Rock Physics - Second Edition*, pages 515–544.

Johnstad, S., Farrell, B., and Ringstad, C. (2005). EM seabed logging on the Troll Field. EAGE 67th Conference & Exhibition - Madrid, Spain.

Kong, F. N., Westerdahl, H., Ellingsrud, S., Eidesmo, T., and Johansen, S. (2002). Seabed logging: A possible direct hydrocarbon indicator for deepsea prospects using EM energy. *Oil and Gas Journal*, 100(19).

Kumar, K. C. H. (2010). On the Application of Simandoux and Indonesian Shaly Sand Resistivity Interpretation Models in Low and High R_w Regimes. 8th Biennial International Conference & Exposition on Petroleum Geophysics, Hyderabad 2010.

La Vigne, J., Herron, M., and Hertzog, R. (1994). Density-Neutron Interpretation in Shaly Sands. SPWLA 35th Annual Logging Symposium.

Leveaux, J. and Poupon, A. (1971). Evaluation Of Water Saturation In Shaly Formations. *The Log Analyst*, 12(4).

Lindom, B., Lie, J., and Ridyard, D. (2007). Electromagnetic Prospect Scanning - Seabed Logging Moves from Risk Reduction to Value Creation . International Oil Conference and Exhibition in Mexico.

Løseth, L. O., Haabesland, N. E., Linberg, B., Hansen, J. O., and Henriksen, L. B. (2015). Pingvin - proving a new play in a frontier area. Exploration Revived, Bergen 16-18th March 2015. 6th NPF Biennial Petroleum Geology Conference.

Maaø, F. A. and Nguyen, A. K. (2010). Enhanced subsurface response for marine CSEM surveying. *Geophysics*, 75(3):A7–A10.

MacGregor, Harris, and Walls (2008). CSEM modeling study using iMOSS-EM. 70th EAGE Conference & Exhibition - Rome, Italy.

MacGregor, L., Andreis, D., and Cooper, R. (2010). Integrated interpretation of seismic, CSEM and well log information for reservoir characterization. EGM 2010 International Workshop: Adding new value to Electromagnetic, Gravity and Magnetic Methods for Exploration.

MacGregor, L. and Tomlinson, J. (2014). Marine controlled-source electromagnetic methods in the hydrocarbon industry: A tutorial on method and practice. *Interpretation*, 3(3):SH13–SH32.

Mitchum, R., Vail, P., and Thompson, S. (1977). Seismic Stratigraphy and Global Changes of Sea Level, Part 2: The Depositional Sequence as a Basic Unit for Stratigraphic Analysis. In: Payton (Ed.), Seismic Stratigraphy: Application to Hydrocarbon Exploration. AAPG-Memoir No. 26, AAPG, Tulsa, p. 53-62.

Mittet, R., Brauti, K., Maulana, H., and Wicklund, T. A. (2008). CMP inversion and post-inversion modelling for marine CSEM data. *First Break*, 26(8):59–67.

Mittet, R. and Morten, J. P. (2012). Detection and imaging sensitivity of the marine CSEM method. *Geophysics*, 77(6):E411–E425.

Mittet, R. and Morten, J. P. (2013). The marine controlled-source electromagnetic method in shallow water. *Geophysics*, 78(2):E67–E77.

Morten, J. P., Roth, F., Karlsen, S. A., Timko, D., Pacurar, C., Olsen, P. A., Nguyen, A. K., and Gjengedal, J. (2012). Field appraisal and accurate resource estimation from 3D quantitative interpretation of seismic and CSEM data. *The Leading Edge*, 31(4):447–456.

Morten, J. P., Roth, F., Timko, D., Pacurar, C., Nguyen, A. K., and Olsen, P. A. (2011). 3D reservoir characterization of a North Sea oil field using quantitative seismic & CSEM interpretation. SEG Technical Program Expanded Abstracts 2011: pp. 1903-1907.

Morten, J. P., Veire, H. H., Granli, J. R., and Gabrielsen, P. T. (2017). Quantitative comparison of deep-reading well resistivity to 3D CSEM at Wisting. SEG International Exhibition and 87th Annual Meeting, September 2017 Houston, Texas.

Nelson, R. J. and Mitchell, W. K. (1990). Improved Vertical Resolution Of Well Logs By Resolution Matching. SPWLA 31st Annual Logging Symposium, 24-27 June, Lafayette, Louisiana.

Nguyen, A. K., Nordskag, J., Wiik, T., Bjørke, A., Boman, L., Pedersen, O., Ribaudo, J., and Mittet, R. (2016). Comparing large-scale 3D Gauss-Newton and BFGS CSEM inversions. SEG International Exposition and 86th Annual Meeting.

Norwegian Petroleum Directorate (2017). Oil and gas discovery northwest of 7220/11-1 (Alta) in the Barents Sea - 7219/12-1 and 7219/12-1 A. `http://www.npd.no/en/news/Exploration-drilling-results/2017/721912-1-and-721912-1-A/` [Online: accessed 08 Jun 2017].

Norwegian Petroleum Directorate (n.d.a). FactMap. http://gis.npd.no/factmaps/html_21/ Interactive map of the petroleum activity on the Norwegian continental shelf.

Norwegian Petroleum Directorate (n.d.b). Factpages. http://factpages.npd.no/factpages/Default.aspx?culture=no [Online: accessed 15 Mar 2017].

Norwegian Petroleum Directorate (n.d.c). Kolmule Fm. http://factpages.npd.no/FactPages/Default.aspx?nav1=strat&nav2=PageView|Litho|Formations&nav3=85&culture=en [Online: accessed 21 Mar 2017].

Norwegian Petroleum Directorate (n.d.d). Kveite Fm. http://factpages.npd.no/FactPages/Default.aspx?nav1=strat&nav2=PageView|Litho|Formations&nav3=89&culture=en [Online: accessed 21 Mar 2017].

Norwegian Petroleum Directorate (n.d.e). Overview of geographical data available from the Norwegian Petroleum Directorate. http://factpages.npd.no/ReportServer?/Factpages/geography/geography_all&rs:Command=Render&rc:Toolbar=false&rc:Parameters=f&IpAddress=1&CultureCode=en [Online: accessed 10 Mar 2017].

Norwegian Petroleum Directorate (n.d.f). Torsk Fm. http://factpages.npd.no/FactPages/Default.aspx?nav1=strat&nav2=PageView|Litho|Formations&nav3=172&culture=en [Online: accessed 09 Apr 2017].

Norwegian Petroleum Directorate (n.d.g). Wellbore 7319/12-1. http://factpages.npd.no/FactPages/Default.aspx?nav1=wellbore&nav2=PageView|Exploration|All&nav3=7555&culture=en [Online: accessed 09 Apr 2017].

Palacky, G. (1987). Resistivity characteristics of geologic targets. *Electromagnetic Methods in Applied Geophysics*, 1.

Peeters, M. (2011). Review of existing shaly sand evaluation models and introduction of a new method based on dry clay parameters. SPWLA 52nd Annual Logging Symposium, May 14-18, 2011.

Ramberg, I. B., Bryhni, I., and Nøttvedt, A. (2007). *Landet blir til: Norges geologi*. Norsk Geologisk Forening (NGF).

Richardsen, G., Vorren, T., and Tørudbakken, B. (1993). Post-Early Cretaceous uplift

and erosion in the southern Barents Sea: a discussion based on analysis of seismic interval velocities. *Norsk Geologisk Tidsskrift*, 73:3–20.

Rider, M. (1996). *The Geological Interpretation of Well Logs*. Gulf Publishing.

Røsten, T., Johnstad, S., Ellingsrud, S., Amundsen, H. E. F., Johansen, S. E., and I., B. (2003). A sea bed logging (SBL) calibration survey over the Ormen Lange gas field. EAGE 65th Conference & Exhibition - Stavanger, Norway.

Ryseth, A., Augustson, J. H., Charnock, M., Haugerud, O., Knutsen, S.-M., Midbøe, P. S., Opsal, J. G., and Sundsbø, G. (2003). Cenozoic stratigraphy and evolution of the Sørvestsnaget Basin, southwestern Barents Sea. *Norwegian Journal of Geology*, 83(2):107–130.

Schlumberger (1987). Log Interpretation Principles/Applications.

Schlumberger (2009). Log interpretation charts.

Schroeder, F. (n.d.). Well-Seismic Ties. American Association of Petroleum Geologists `http://archives.aapg.org/slide_resources/schroeder/7/index.cfm` [Online: accessed 17 Mar 2017].

Simandoux, P. (1963). Dielectric measurements on porous media application to the measurement of water saturations: study of the behaviour of argillaceous formations. Revue de l'Institut Francais du Petrole 18, Supplementary number, p. 193-215.

Simm, R. and White, R. (2002). Phase, polarity and the interpreter's wavelet. *First Break*, 20(5):277–281.

Skelt, C. (1995). An Integrated Approach to Saturation Height Analysis. SPWLA 36th Annual Logging Symposium.

Spichak, V. (2015). *Electromagnetic Sounding of the Earth's Interior*. Elsevier, second edition.

Spies, B. R. (1989). Depth of investigation in electromagnetic sounding methods. *Geophysics*, 54(7):872–888.

Statoil (2014). Gas discovery in Pingvin. `https://www.statoil.com/content/statoil/en/news/archive/2014/09/26/26SeptGasFindPingvin.html` [Online: accessed 23 Feb 2017].

Stewart, R. R., Huddleston, P. D., and Kan, T. K. (1984). Seismic versus sonic velocities: A vertical seismic profiling study. *Geophysics*, 49(8):1153–1168.

Støren, T., Zach, J., and Maaø (2008). Gradient Calculations for 3D Inversion of CSEM Data Using a Fast Finite-difference Time-domain Modelling Code. 70th EAGE Conference & Exhibition - Rome, Italy.

Szabó, N. P. (2011). Shale Volume Estimation Based on the Factor Analysis of Well-Logging Data. *Acta Geophysica*, 59(5):935–953.

Tveit, S. (2014). *Inversion of CSEM Data for Subsurface Structure Identification and Numerical Assessment of the Upstream Mobility Scheme*. PhD thesis, University of Bergen.

Veeken, P. (2007). *Handbook of Geophysical Exploration - Seismic Stratigraphy, Basin Ananlysis and Reservoir Characterisation*, volume 37. Elsevier.

Vieugue, V. (2014). The Importance of Electromagnetic (EM) Data - Avoiding Dry Wells in the Barents Sea. *EM Exploration*, 9:12–13.

Vold, I., Rotevatn, A., and J., H. (2012). The effect of hydrocarbon saturation on resistivity distribution and CSEM response. *Marine and Petroleum Geology*, 38(1):117–127.

White, R. and Simm, R. (2003). Tutorial: Good practice in well ties. *First Break*, 21(10):75–83.

Wicklund, T. and Fanavoll, S. (2004). Norwegian Sea - SBL Case Study. EAGE 66th Conference & Exhibition - Paris, France.

Woodhouse, R. and Warner Jr., H. R. (2004). Improved Log Analysis in Shaly-Sandstones-Based on Sw and Hydrocarbon Pore Volume Routine Measurements of Preserved Cores Cut in Oil-Based Mud. *Petrophysics*, 45(3):281–295.

Worsley, D. (1986). *The geological history of Svalbard: evolution of an arctic archipelago*. Den norske stats oljeselskap a.s.

Worsley, D. (2008). The post-Caledonian development of Svalbard and the western Barents Sea. *Polar Research*, 27(3):298–317.

Worthington, P. (1985). The evolution of shaly-sand concepts in reservoir evaluation. *The Log Analyst*, 26(1):23–40.

Worthington, P. F. (2011). The Petrophysics of Problematic Reservoirs. *Journal of Petroleum Technology*, 63(12):88–96.

Zach, J. and Frenkel, M. (2009). 3D Inversion-Based Interpretation of Marine CSEM Data. Offshore Technology Conference.

Zhdanov, M. S., Gribenko, A., and Čuma, M. (2007). Regularized focusing inversion of marine CSEM data using minimum vertical support stabilizer. SEG Technical Program Expanded Abstracts 2007.

Appendices

Appendix A

Schlumberger Log Interpretation Charts

The charts are found in Schlumberger's "Log Interpretation Charts" from 2009 (Schlumberger, 2009).

The charts have been used for petrophysical analysis. See Section 5.4 for method description and Section 6.4 for results.

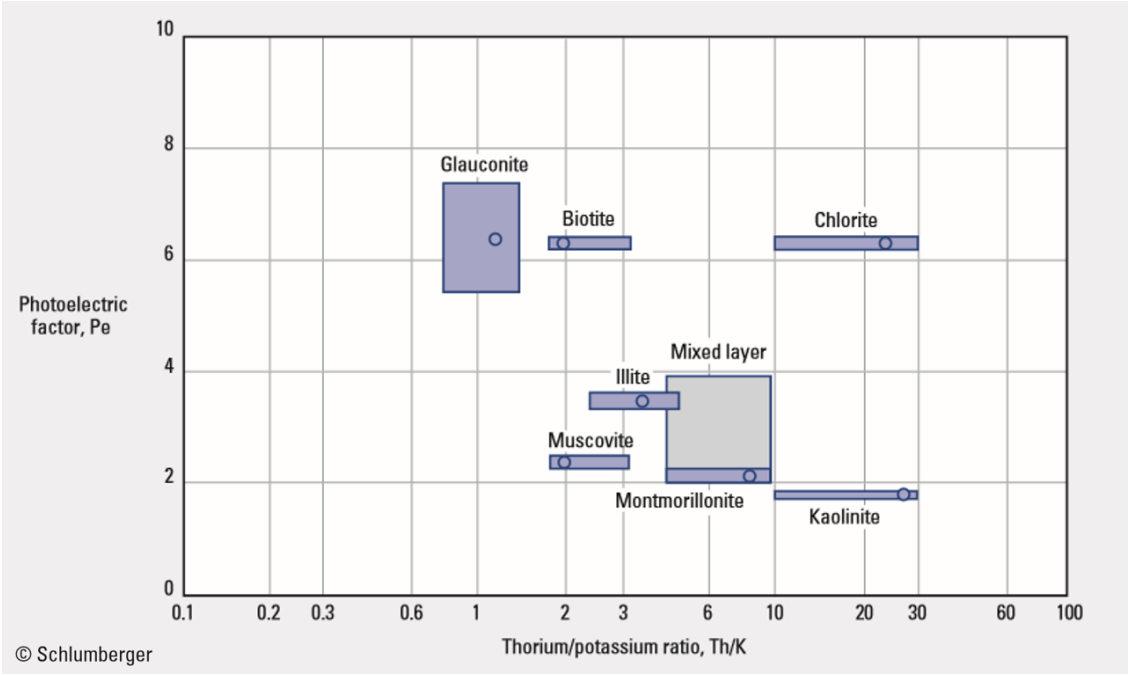

Figure A.1: *Chart Lith-1B: Cross-plot between photoelectric factor (Pe) and thorium/potassium ratio (Th/K). The chart has been used for identifying the type of minerals encountered in the formation(s) in the wellbore.*

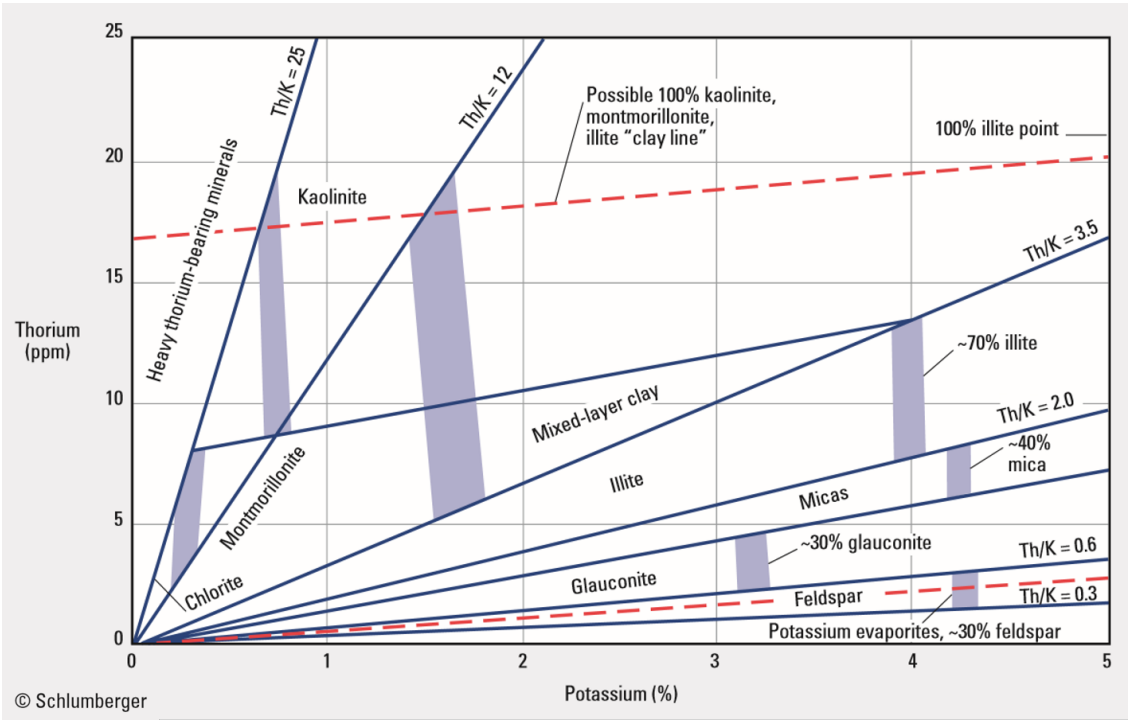

Figure A.2: *Chart Lith-2: Cross-plot between thorium and potassium. The chart has been used for determining the type of minerals in the formation(s) from concentrations of thorium and potassium measured by the natural gamma ray spectroscopy (NGS) tool.*

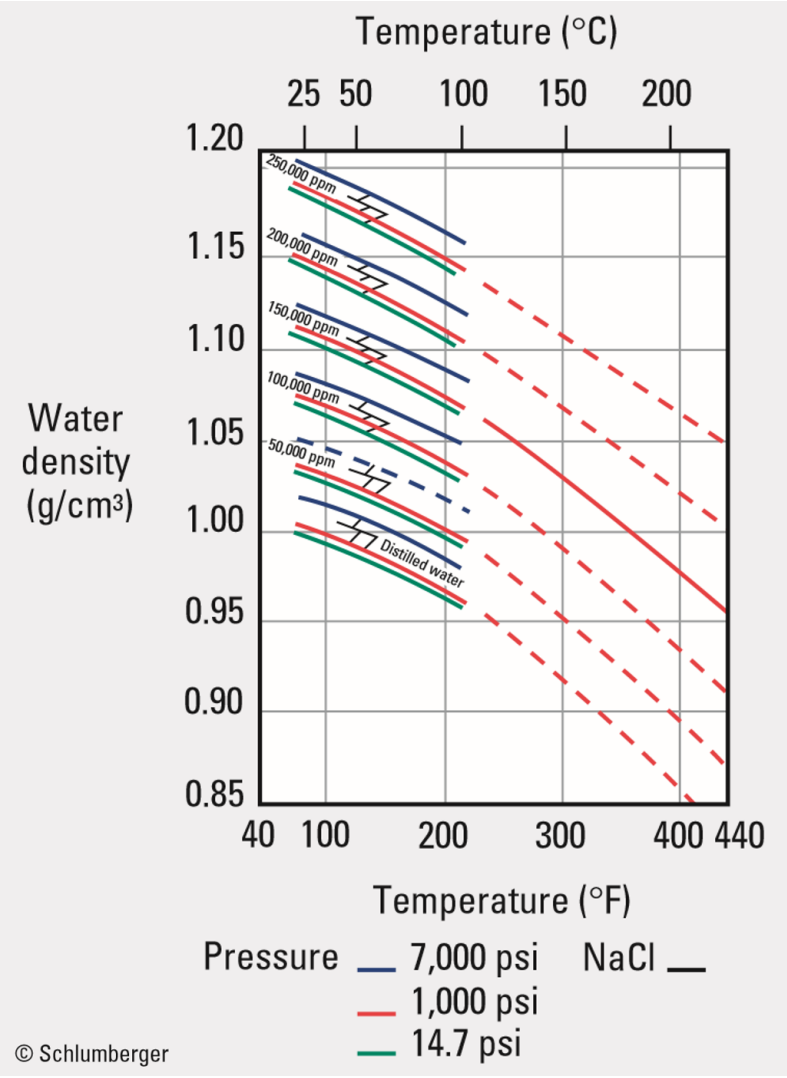

Figure A.3: *Chart Gen-7: Water density determination from known values of temperature, pressure and salinity of the water.*

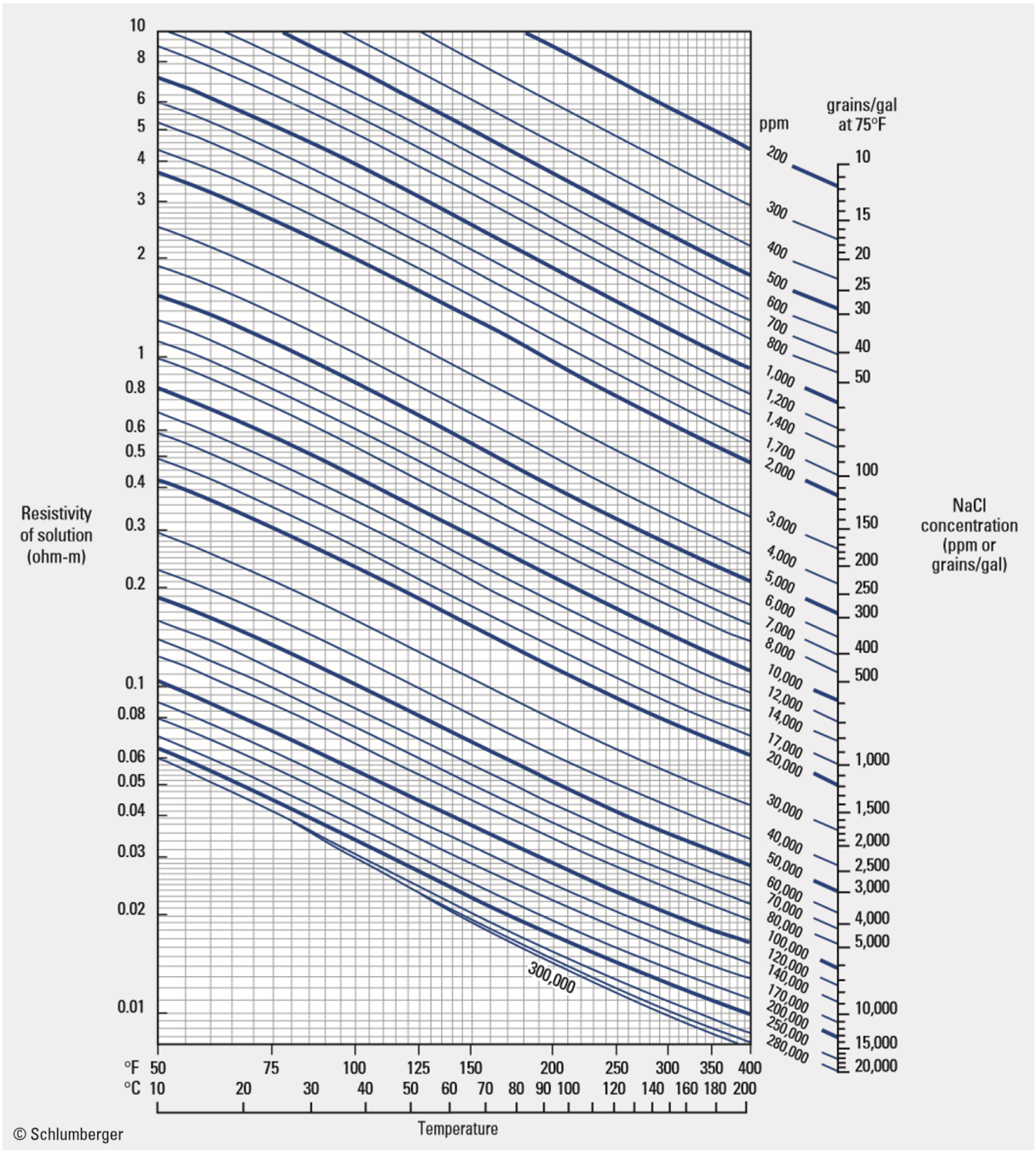

Figure A.4: *Chart GEN-6: Fluid resistivity as a function of temperature and NaCl concentration. The chart can be used to determine the resistivity of an equivalent NaCl concentration at a specific temperature and to provide a transition of resistivity at a specific temperature to another temperature. For this project, the salinity has been found from known values of resistivity and temperature.*

Appendix B

Relationships Between Anomalous Transverse Resistance and Gross Pay

B.1 Relationship Based on Well Data

Anomalous transverse resistance (ATR) as a function of gross pay (see Figure 6.49). The relationship has been created from the relationship between upscaled vertical resistivity and gross pay based on well data. The associated gross pay map is presented in Figure 6.50.

data file

ATR [Ohmmm]	GROSS PAY [m]
0.00000000000000000e+00	0.00000000000000000e+00
4.07405254229025626e-01	1.01010101010101016e+00
1.51003795040876021e+00	2.02020202020202033e+00
3.10936299671129390e+00	3.03030303030302760e+00
5.03191712152989723e+00	4.04040404040406640e+00
7.15352416823659354e+00	5.05050505050510520e+00
9.39447574813273079e+00	6.06060606060605520e+00
1.17064303678419819e+01	7.07070707070709400e+00
1.40608144862461870e+01	8.08080808080813280e+00
1.64408615738373811e+01	9.09090909090917170e+00
1.88366958555933479e+01	1.01010101010102100e+01

2.124243817403112189e+01	1.111111111111111249e+01
2.365453582944511624e+01	1.212121212121212110e+01
2.607080347292879452e+01	1.313131313131313149e+01
2.848987027616799139e+01	1.414141414141414188e+01
3.091085840978910682e+01	1.515151515151515227e+01
3.333319373285134191e+01	1.616161616161616266e+01
3.575649269824301513e+01	1.717171717171717304e+01
3.818049370138051302e+01	1.818181818181818343e+01
4.060501469526438711e+01	1.919191919191919382e+01
4.302992655958200885e+01	2.020202020202020421e+01
4.545513606717894106e+01	2.121212121212121460e+01
4.788057479206527489e+01	2.222222222222222499e+01
5.030619175638317131e+01	2.323232323232323537e+01
5.273194846925936474e+01	2.424242424242424221e+01
5.515781552109216079e+01	2.525252525252525260e+01
5.758377020592708107e+01	2.626262626262626299e+01
6.000979483438752027e+01	2.727272727272727337e+01
6.243587551786103518e+01	2.828282828282828376e+01
6.486200127933746273e+01	2.929292929292929415e+01
6.728816339414363767e+01	3.030303030303030454e+01
6.971435489489391557e+01	3.131313131313131493e+01
7.214057019542553917e+01	3.232323232323232531e+01
7.456680480212801854e+01	3.333333333333333570e+01
7.699305509029225902e+01	3.434343434343434609e+01
7.941931812941366786e+01	3.535353535353535648e+01
8.184559154576098194e+01	3.636363636363636687e+01
8.427187341359726247e+01	3.737373737373737725e+01
8.669816216861914882e+01	3.838383838383838764e+01
8.912445653878410212e+01	3.939393939393939803e+01
9.155075548880665792e+01	4.040404040404040842e+01
9.397705817549291396e+01	4.141414141414141881e+01
9.640336391169785202e+01	4.242424242424242919e+01
9.882967213717773802e+01	4.343434343434343958e+01
1.012559823949749500e+02	4.444444444444444997e+01
1.036822943122568006e+02	4.545454545454546036e+01
1.061086075847481709e+02	4.646464646464647075e+01
1.085349219640717422e+02	4.747474747474748114e+01
1.109612372474436199e+02	4.848484848484848442e+01
1.133875532692797776e+02	4.949494949494949481e+01
1.158138698943564862e+02	5.050505050505050519e+01

1.182401870122325533e+02	5.151515151515151558e+01
1.206665045327007704e+02	5.252525252525252597e+01
1.230928223820758944e+02	5.353535353535353636e+01
1.255191405001653493e+02	5.454545454545454675e+01
1.279454588377965365e+02	5.555555555555555713e+01
1.303717773547978709e+02	5.656565656565656752e+01
1.327980960183504067e+02	5.757575757575757791e+01
1.352244148016409611e+02	5.858585858585858830e+01
1.376507336832659405e+02	5.959595959595959869e+01
1.400770526438189165e+02	6.060606060606060908e+01
1.425033716701852029e+02	6.161616161616161946e+01
1.449296907499138456e+02	6.262626262626262985e+01
1.473560098732432948e+02	6.363636363636364024e+01
1.497823290321972536e+02	6.464646464646465063e+01
1.522086482202590219e+02	6.565656565656566102e+01
1.546349674321040197e+02	6.666666666666667140e+01
1.570612866633814235e+02	6.767676767676768179e+01
1.594876059105367574e+02	6.868686868686869218e+01
1.619139251706652374e+02	6.969696969696970257e+01
1.643402444413940486e+02	7.070707070707071296e+01
1.667665637207838643e+02	7.171717171717172334e+01
1.691928830072505434e+02	7.272727272727273373e+01
1.716192022994995341e+02	7.373737373737374412e+01
1.740455215964731224e+02	7.474747474747475451e+01
1.764718408973070041e+02	7.575757575757576490e+01
1.788981602012951271e+02	7.676767676767677528e+01
1.813244795078624634e+02	7.777777777777778567e+01
1.837507988165338588e+02	7.878787878787879606e+01
1.861771181269258477e+02	7.979797979797980645e+01
1.886034374387237449e+02	8.080808080808081684e+01
1.910297567516702770e+02	8.181818181818182723e+01
1.934560760655554077e+02	8.282828282828283761e+01
1.958823953802074698e+02	8.383838383838384800e+01
1.983087146954861737e+02	8.484848484848485839e+01
2.007350340112767526e+02	8.585858585858586878e+01
2.031613533274857559e+02	8.686868686868687917e+01
2.055876726440366156e+02	8.787878787878788955e+01
2.080139919608665764e+02	8.888888888888889994e+01
2.104403112779248772e+02	8.989898989898991033e+01
2.128666305951696245e+02	9.090909090909092072e+01

```
2.15292949912566712e+02    9.19191919191931l1e+01
2.17719269230088400e+02    9.29292929292941l9e+01
2.20145588547711611e+02    9.39393939393951l8e+01
2.22571907865417927e+02    9.49494949494962l7e+01
2.24998227183192341e+02    9.59595959595972l6e+01
2.27424546501022007e+02    9.69696969696968l4e+01
2.29850865818897148e+02    9.79797979797979l2e+01
2.32277185136809237e+02    9.89898989898989l1e+01
2.34703504454751680e+02    1.00000000000000000e+02
```

B.2 Relationship Based on Well Data and the Modified Simandoux Equation

Anomalous transverse resistance (ATR) as a function of gross pay (see Figure 6.49). The relationship has been created from the relationship between upscaled vertical resistivity and water saturation based on well data and the modified Simandoux equation. The associated gross pay map is presented in Figure 6.51.

data file

```
      ATR [Ohmmm]                GROSS PAY [m]

0.00000000000000000e+00    0.00000000000000000e+00
5.75553629445701098e-01    1.01010101010101016e+00
2.50393593570895589e+00    2.02020202020202032e+00
6.13377375064643715e+00    3.03030303030302760e+00
1.18774508342650086e+01    4.04040404040406640e+00
2.02100692957053560e+01    5.05050505050510520e+00
3.16618857382000769e+01    6.06060606060605520e+00
4.68025011316024404e+01    7.07070707070709400e+00
6.62160217711924872e+01    8.08080808080813280e+00
9.04680449880454489e+01    9.09090909090917170e+00
1.20067413536910806e+02    1.01010101010102100e+01
1.55427644475818482e+02    1.11111111111112490e+01
1.96834003906085457e+02    1.21212121212121100e+01
2.44421764364445266e+02    1.31313131313131490e+01
```

```
2.98169177532286767e+02    1.41414141414141888e+01
3.57905711783076128e+02    1.51515151515151522e+01
4.23333139844436857e+02    1.61616161616161626e+01
4.94055035522016282e+02    1.71717171717171730e+01
5.69609588392798741e+02    1.81818181818181834e+01
6.49501240131824943e+02    1.91919191919191938e+01
7.33227987452523052e+02    2.02020202020202042e+01
8.20302721706394095e+02    2.12121212121212146e+01
9.10268274506302532e+02    2.22222222222222250e+01
1.00270672505531842e+03    2.32323232323232354e+01
1.09724399140633590e+03    2.42424242424242458e+01
1.19355086636951227e+03    2.52525252525252562e+01
1.29134158805762058e+03    2.62626262626262666e+01
1.39037085895729865e+03    2.72727272727272770e+01
1.49043001916396497e+03    2.82828282828282874e+01
1.59134288214696653e+03    2.92929292929292978e+01
1.69296157540929698e+03    3.03030303030303082e+01
1.79516259936229517e+03    3.13131313131313186e+01
1.89784322339716164e+03    3.23232323232323290e+01
2.00091827280319194e+03    3.33333333333333394e+01
2.10431731735224821e+03    3.43434343434343498e+01
2.20798224605686482e+03    3.53535353535353602e+01
2.31186519788068290e+03    3.63636363636363706e+01
2.41592681123282591e+03    3.73737373737373810e+01
2.52013475312349237e+03    3.83838383838383914e+01
2.62446248993472864e+03    3.93939393939394018e+01
2.72888826452550802e+03    4.04040404040404122e+01
2.83339424797247330e+03    4.14141414141414226e+01
2.93796583808664718e+03    4.24242424242424330e+01
3.04259108061248162e+03    4.34343434343434434e+01
3.14726019252234255e+03    4.44444444444444538e+01
3.25196516997723029e+03    4.54545454545454642e+01
3.35669946630306276e+03    4.64646464646464746e+01
3.46145772773615499e+03    4.74747474747474850e+01
3.56623557674659332e+03    4.84848484848484954e+01
3.67102943448815631e+03    4.94949494949495058e+01
3.77583637538616449e+03    5.05050505050505162e+01
3.88065400809720541e+03    5.15151515151515266e+01
3.98548037809211792e+03    5.25252525252525370e+01
4.09031388795722478e+03    5.35353535353535474e+01
```

4.19515232206447683e+03	5.45454545454454675e+01
4.299997343972424460e+03	5.555555555555555713e+01
4.40484535141876949 6e+03	5.656565656565656752e+01
4.50969654210525641 2e+03	5.757575757575757791e+01
4.61455033385792467 0e+03	5.858585858585858830e+01
4.71940625095864925 2e+03	5.959595959595959869e+01
4.82426390468415138 5e+03	6.060606060606060908e+01
4.92912297740081976 4e+03	6.161616161616161946e+01
5.03398320956628413 1e+03	6.262626262626262985e+01
5.13884438910684275 5e+03	6.363636363636364024e+01
5.24370634273683299 4e+03	6.464646464646465063e+01
5.34856892886505738 7e+03	6.565656565656566102e+01
5.45343203179825923 1e+03	6.666666666666667140e+01
5.55829555700453420 3e+03	6.767676767676768179e+01
5.66315942724295382 5e+03	6.868686868686869218e+01
5.76802357940097499 5e+03	6.969696969696970257e+01
5.87288796191027540 8e+03	7.070707070707071296e+01
5.97775253263521153 7e+03	7.171717171717172334e+01
6.08261725714743533 9e+03	7.272727272727273373e+01
6.18748210731626477 4e+03	7.373737373737374412e+01
6.29234706015649226 2e+03	7.474747474747475451e+01
6.39721209688744329 5e+03	7.575757575757576490e+01
6.50207720216376765 2e+03	7.676767676767677528e+01
6.60694236344708951 9e+03	7.777777777777778567e+01
6.71180757049255316 8e+03	7.878787878787879606e+01
6.81667281492929578 2e+03	7.979797979797980645e+01
6.92153808991766618 4e+03	8.080808080808081684e+01
7.02640338986911865 5e+03	8.181818181818182723e+01
7.13126871021737406 4e+03	8.282828282828283761e+01
7.23613404723142230 1e+03	8.383838383838384800e+01
7.34099939786273353 1e+03	8.484848484848485839e+01
7.44586475962041822 6e+03	8.585858585858586878e+01
7.55073013046922005 7e+03	8.686868686868687917e+01
7.65559550874618435 0e+03	8.787878787878788955e+01
7.76046089309253784 4e+03	8.888888888888889994e+01
7.86532628239805853 8e+03	8.989898989898991033e+01
7.97019167575560732 1e+03	9.090909090909092072e+01
8.07505707242398239 0e+03	9.191919191919193111e+01
8.17992247179756122 9e+03	9.292929292929294149e+01
8.28478787338150687 0e+03	9.393939393939395188e+01

```
8.389653276771490710e+03    9.494949494949496227e+01
8.494518681637151531e+03    9.595959595959597266e+01
8.599384087708556763e+03    9.696969696969696884e+01
8.704249494765148484e+03    9.797979797979797922e+01
8.809114902626717594e+03    9.898989898989898961e+01
8.913980311146013264e+03    1.000000000000000000e+02
```

B.3 Relationship Based on the Archie Equation

Anomalous transverse resistance (ATR) as a function of gross pay (see Figure 6.49). The relationship has been created from the relationship between upscaled vertical resistivity and water saturation based on the Archie equation. The associated gross pay map is presented in Figure 6.52.

data file

```
      ATR [Ohmmm]                GROSS PAY [m]

0.000000000000000000e+00    0.000000000000000000e+00
2.151321388342298135e+00    1.010101010101010166e+00
1.207693930722249398e+01    2.020202020202020332e+00
3.855704768421600903e+01    3.030303030303030276e+00
9.626928718948717290e+01    4.040404040404040664e+00
2.045428854590038554e+02    5.050505050505051052e+00
3.814794364953290824e+02    6.060606060606060552e+00
6.361935516528097878e+02    7.070707070707070940e+00
9.653882573035798487e+02    8.080808080808081328e+00
1.356567558580169361e+03    9.090909090909091717e+00
1.794089927361134414e+03    1.010101010101010210e+01
2.263722771980042580e+03    1.111111111111111249e+01
2.754495493561870717e+03    1.212121212121212110e+01
3.258732895689709039e+03    1.313131313131313149e+01
3.771369472675540692e+03    1.414141414141414188e+01
4.289178121260858461e+03    1.515151515151515227e+01
4.810146491519471056e+03    1.616161616161616266e+01
5.333035890859561732e+03    1.717171717171717304e+01
5.857089803522723741e+03    1.818181818181818343e+01
```

6.381848381580174646e+03	1.919191919191919382e+01
6.907032905568511524e+03	2.020202020202020421e+01
7.432474731950775094e+03	2.121212121212121460e+01
7.958071926754758351e+03	2.222222222222222499e+01
8.483762916363262775e+03	2.323232323232323537e+01
9.009510521126121603e+03	2.424242424242424221e+01
9.535292296214603994e+03	2.525252525252525260e+01
1.006109469387900390e+04	2.626262626262626299e+01
1.058690953734982577e+04	2.727272727272727337e+01
1.111271189177227505e+04	2.828282828282828376e+01
1.163855877894558944e+04	2.929292929292929415e+01
1.216438840155004436e+04	3.030303030303030454e+01
1.269021967492955264e+04	3.131313131313131493e+01
1.321605194451450734e+04	3.232323232323232531e+01
1.374188481528603188e+04	3.333333333333333570e+01
1.426771804885918209e+04	3.434343434343434609e+01
1.479355150137426608e+04	3.535353535353535648e+01
1.531938508601541980e+04	3.636363636363636687e+01
1.584521875039139195e+04	3.737373737373737725e+01
1.637105246288535454e+04	3.838383838383838764e+01
1.689688620441731837e+04	3.939393939393939803e+01
1.742271996347300228e+04	4.040404040404040842e+01
1.794855373310381401e+04	4.141414141414141881e+01
1.847438750911645184e+04	4.242424242424242919e+01
1.900022128898035953e+04	4.343434343434343958e+01
1.952605507116841545e+04	4.444444444444444997e+01
2.005188885475903953e+04	4.545454545454546036e+01
2.057772263919607940e+04	4.646464646464647075e+01
2.110355642414390604e+04	4.747474747474748114e+01
2.162939020939996772e+04	4.848484848484848442e+01
2.215522399484205016e+04	4.949494949494949481e+01
2.268105778039640427e+04	5.050505050505050519e+01
2.320689156601850118e+04	5.151515151515151558e+01
2.373272535168148897e+04	5.252525252525252597e+01
2.425855913736896400e+04	5.353535353535353636e+01
2.478439292307149663e+04	5.454545454545454675e+01
2.531022670878320059e+04	5.555555555555555713e+01
2.583606049450014325e+04	5.656565656565656752e+01
2.636189428022036373e+04	5.757575757575757791e+01
2.688772806594256326e+04	5.858585858585858830e+01

2.74135618516659415e+04	5.95959595959595869e+01
2.79393956373900473e+04	6.06060606060606090e+01
2.84652294231145861e+04	6.16161616161616194e+01
2.89910632088393868e+04	6.26262626262626298e+01
2.95168969945643439e+04	6.36363636363636402e+01
3.00427307802894029e+04	6.46464646464646506e+01
3.05685645660145165e+04	6.56565656565656610e+01
3.10943983517396628e+04	6.66666666666667140e+01
3.16202321374648236e+04	6.76767676767676818e+01
3.21460659231900063e+04	6.86868686868686922e+01
3.26718997089151962e+04	6.96969696969697026e+01
3.31977334946403935e+04	7.07070707070707130e+01
3.37235672803655762e+04	7.17171717171717233e+01
3.42494010660907807e+04	7.27272727272727337e+01
3.47752348518159779e+04	7.37373737373737441e+01
3.53010686375411751e+04	7.47474747474747545e+01
3.58269024232663724e+04	7.57575757575757649e+01
3.63527362089915696e+04	7.67676767676767753e+01
3.68785699947167741e+04	7.77777777777777857e+01
3.74044037804419713e+04	7.87878787878787961e+01
3.79302375661671758e+04	7.97979797979798065e+01
3.84560713518923730e+04	8.08080808080808168e+01
3.89819051376175630e+04	8.18181818181818272e+01
3.95077389233427602e+04	8.28282828282828376e+01
4.00335727090679647e+04	8.38383838383838480e+01
4.05594064947931619e+04	8.48484848484848584e+01
4.10852402805183592e+04	8.58585858585858688e+01
4.16110740662435637e+04	8.68686868686868792e+01
4.21369078519687609e+04	8.78787878787878896e+01
4.26627416376939581e+04	8.88888888888889000e+01
4.31885754234191626e+04	8.98989898989899103e+01
4.37144092091443598e+04	9.09090909090909207e+01
4.42402429948695643e+04	9.19191919191919311e+01
4.47660767805947615e+04	9.29292929292929415e+01
4.52919105663199660e+04	9.39393939393939519e+01
4.58177443520451632e+04	9.49494949494949623e+01
4.63435781377703533e+04	9.59595959595959727e+01
4.68694119234955578e+04	9.69696969696969831e+01
4.73952457092207550e+04	9.79797979797979935e+01
4.79210794949459523e+04	9.89898989898990039e+01

```
4.844691328067112045e+04     1.0000000000000000000e+02
```